ABSTRACT

YAN, JUN. A Numerical and Experimental Investigation of the Machinability of Elastomers. (Under the direction of Dr. John S. Strenkowski.)

The machinability of elastomers is investigated in this dissertation. The main objective of this research is to determine the favorable machining conditions for which elastomers can be machined with a good surface finish. Both orthogonal cutting experiments and finite element model simulations were conducted to achieve this goal. In the orthogonal cutting tests, a wide variety of cutting parameters were examined. Cutting forces, machined surface roughness and temperature were measured to evaluate the effects of various parameters. Rake angle and workpiece temperature were found to have a significant effect on the machined surface roughness during cutting. Large rake angle tools and cryogenic machining produced a smooth machined surface with corresponding continuous ribbon-like chips. In contrast, small rake angle tools generated a rough machined surface.

A plane strain finite element cutting model was developed using ABAQUS/Explicit for simulating the orthogonal rubber cutting process. The model was used to predict the cutting forces, chip shape, stress and strain contours, the strain energy density field, and strain energy history in the chip and workpiece. Good agreement was found between the predicted and measured cutting forces. The finite element simulations demonstrated the ability of the model to predict the characteristics of rubber cutting process. A tensile stress and strain in the cutting direction in the workpiece machined surface near the tool tip was observed when a smooth machined surface was produced.

New insight into the chip formation mechanism of rubber was achieved by using strain energy concepts. The strain energy density near the tool edge was found to be not only larger but it also extended over a larger area when a rough surface was generated. It was found that the strain energy release rate was closely related to the machined surface quality. A large strain energy release rate corresponded to the generation of a rough machined surface.

The understanding gained from the finite element models in this research can be used to develop future guidelines for operating conditions that result in a smooth machined surface finish for machining of elastomers.

A NUMERICAL AND EXPERIMENTAL INVESTIGATION OF THE MACHINABILITY OF ELASTOMERS

by

JUN YAN

A dissertation submitted to the Graduate Faculty of
North Carolina State University
in partial fulfillment of the
requirements for the Degree of
Doctor of Philosophy

MECHANICAL AND AEROSPACE ENGINEERING

Raleigh

2005

APPROVED BY:

Chair of Advisory Committee

BIOGRAPHY

Jun Yan was born in Nanjing, China in September 1972. He graduated from Yan Zi Ji middle school and was admitted into Southeast University in Nanjing through 3-day nation-wide exams in July 1991. In June 1995, Mr. Yan received his Bachelor of Science degree in Mechanical Engineering from Southeast University and ranked No. 1 in the class. After his graduation, he was immediately admitted to the graduate school at Southeast University with admission exams waived by the school. In March 1998, he received his Master of Science in Mechanical Engineering with a concentration in structure health monitoring and fault diagnostics. Then, he joined Nanjing Yuejin Automobile Company as a structure engineer. In the meantime, he was also appointed as a lecturer at Nanjing University of Posts and Telecommunications. After having been in his hometown for 28 years, he came to United States in August 2000 to pursue his doctoral degree at North Carolina A&T State University in Greensboro, NC with a concentration in manufacturing techniques of composite materials. During his study, he found that his interest in numerical analysis become stronger and stronger. In August 2002, he transfered to North Carolina State University to continue his Ph.D. study in the area of computational mechanics applied to manufacturing processes with Dr. John S. Strenkowski, a well-known professor in this area.

The author is happily married to Ms. Ling Cao and they had their first baby boy: Leonard C. Yan, who was born on July 5th, 2004 and brings much happiness to their lives.

ACKNOWLEDGEMENTS

The author would like to express his sincere appreciation and gratitude to Dr. John S. Strenkowski, the chairman of the author's Ph.D. advisory committee, for his invaluable guidance, insight, wisdom and encouragement to the completion of this research. It has been the author's great honor to work as his doctoral student for three years. Gratitude is also extended to Dr. Eric Klang, Dr. Zhilin Li and Dr. Kara Peters for serving on the committee.

The author would like to thank Richard Lemaster, director of Wood Machining and Tooling Research program and Tim Horn, graduate student at the department of Wood & Paper Science for providing instruments, machines and assistances in the experiments. Appreciation is also extended to Mike Breedlove and Rufus (Skip) Richardson of the Mechanical Engineering fabrication shop for their assistance in preparing fixtures, workpieces and tooling. Gratitude is extended to Gwendolyn Smith, Mechanical Engineering departmental receptionist, for her endless encouragement.

Special thanks are also extended to the National Science Foundation for financial support of this research under Grant No. DMI-0099829 and the Department of Mechanical and Aerospace Engineering for partial financial assistance during his PhD study. Funds provided by them made possible the purchase of materials used in this study and the financial support of the author. Lord Corporation is specially appreciated for supplying test samples and characterizing their material response.

Finally, the author would like to express his deep appreciation and love to his parents, brother and his dearest wife, Ling Cao, and their lovely son, Leonard C. Yan, for their unconditional love, patience and support throughout this work. Their steadfast support provided constant encouragement without which, completion of this work would not have been possible.

Appreciation and gratitude are extended to all those who supported, encouraged and assisted him throughout this work.

TABLE OF CONTENTS

TABLE OF CONTENTS (continued)

LIST OF TABLES

LIST OF FIGURES

LIST OF FIGURES (continued)

LIST OF FIGURES (continued)

1. INTRODUCTION

Elastomers have been used as an engineering material for nearly 150 years. According to ASTM D 1566-00 (ASTM, 2000), an elastomer is a material that is capable of recovering from large deformations quickly and forcibly, and can be, or already is, modified to a state in which it is essentially insoluble (but can swell) in a boiling solvent. Elastomers possess many unique material properties. For example, elastomers have a very low elastic modulus and high percent of elongation before fracture, which makes the machining of elastomers a challenge. Elastomers also have very low thermal conductivity. Under cyclic loading, elastomers exhibit significant hysteresis, which contributes to their energy absorption capability. These unique properties have led many industries to adopt elastomers for a wide range of products including tires, springs, shock isolators, noise and vibration absorbers, seals, corrosion and abrasion protection, and electrical and thermal insulators.

Most elastomer parts are manufactured using a molding rather than machining process. In the molding process, raw polymeric materials are mixed with other additives and then heated, melted, and pressed into a mold. Inside the mold, the polymer material is subjected to a controlled temperature-pressure-time cycle. The material is cured, vulcanized, and cooled to produce the desired properties and geometry. To manufacture elastomer parts with complicated shapes, such as tire and footwear tread patterns, a set of molds must first be produced. However, there are many disadvantages associated with molding elastomers including high cost, labor-intensive and time consuming process of mold fabrication and the inflexibility of a mold to design changes. For these reasons, machining offers an attractive

alternative for manufacturing elastomer components, which would be especially useful for manufacturing low volume custom or prototype parts and other applications requiring a complex shape and frequently modified designs. Potential applications of elastomer machining include prototype tire and footwear tread patterns, custom seals for biomedical applications, specialty vibration dampers, and scrap tire recycling equipment.

Very little research on elastomer machining has been conducted because of the complex material response of elastomers and the complexity of the machining process itself. The primary difficulty of machining precision elastomeric parts is due to their low elastic modulus and large deformation characteristics. Early research on elastomer machining was conducted by Jin and Murakawa (Jin and Murakawa, 1998). The benefits of high speed machining using large tool helix and rake angles for manufacturing precision elastomeric parts were demonstrated. The machining of elastomers with sharp woodworking tools and under cryogenic conditions was investigated by Shih et al. (Shih, Lewis, and Strenkowski, 2004). With proper selection of end mill geometries, process parameters, and fixture stiffness, clean grooves can be machined in elastomers. It was also shown that cryogenic cooling of an elastomer workpiece is beneficial in achieving a smooth machined surface.

Orthogonal cutting is the most simplified form of cutting that can be studied without neglecting the complex material aspects associated with the cutting process. Orthogonal rubber cutting experiments have been conducted by Strenkowski and Rodkwan (Rodkwan, 2002). The effects of various machining parameters on chip morphology, machined surface roughness, and the associated machining forces were examined. Feed rate and rake angle

were found to have a significant effect on the types of chips generated during orthogonal cutting. Long and continuous ribbon-like chips and corresponding smooth machined surfaces were produced for high feed speed conditions and large rake angle tools.

Wedge indentation models have been used to investigate chip formation during incipient cutting prior to material separation by Strenkowski and Rodkwan (Strenkowski, Shih, Rodkwan, and Lewis, 2003). Even though wedge indentation does not incorporate chip formation, it can lead to a better understanding of the behavior of elastomers during the initial stages of cutting. Simulations of half-wedge indentation in elastomers were conducted to identify machining conditions that lead to continuous chip formation and good surface finish. Shih and Lewis modeled the rubber workpiece to study its stiffness using ANSYS (Shih, Lewis et al., 2004). Good fixture design was found beneficial in stabilizing the rubber workpiece for a smooth machined surface during the machining process.

1.1. Scope and Objective of Dissertation

In this dissertation, both rubber cutting experiments and numerical simulations of orthogonal rubber cutting process were performed to achieve a better understanding of the material removal mechanisms associated with machining of rubber and to lead to new tooling and fixturing for improving the surface finish of machined rubber. Orthogonal rubber cutting experiments were conducted with an improved stiffer design. A wide variety of parameters, including rake angle, clearance angle, cutting speed, feed rate and workpiece temperature, were studied to determine the effects of those parameters on the machined surface finish.

Cutting forces, machined surface roughness and temperatures were measured with a dynamometer, reflective laser profilmeter and infrared thermometer, respectively. The measurements were used to evaluate the effects of various cutting parameters and to validate the finite element model. Large rake angle tools under cryogenic machining conditions were found to be the most significant factors in achieving a smooth machined surface.

A better understanding of the chip formation process was achieved with the use of finite element models of orthogonal rubber cutting. These models were developed in this research using ABAQUS/Explicit with user-supplied material subroutines to study the machinability of elastomers (Yan and Strenkowski, 2005). The models were used to predict cutting forces, chip shape, stress and strain fields, strain energy density field and strain energy history in the chip and workpiece for various rake angles and feeds. Tool tip sharpness was also incorporated into the model by considering an average tool tip radius. Good agreement was found between the predicted and measured cutting forces, and the predicted and experimental chip shapes. A large principal cutting force and high cutting force fluctuations were found to be associated with a rough machined surface. Stress and strain contours throughout the workpiece were compared with those in the metal cutting models. A von Mises stress failure criterion was identified as a material failure criterion for rubber. The stress and strain contours beneath the tool clearance face, and the strain energy density and strain energy release rate were used to explain the relationships between tool rake angle and the machined surface roughness. Tensile stress and positive strain in the cutting direction were observed on the machined surface near the tool tip when a smooth surface was produced. For rough surfaces, a large distribution of strain energy density and strain energy variation were found.

In summary, the models developed in this research have provided new insight into the mechanisms of chip formation of elastomers.

2. LITERATURE REVIEW

2.1. Introduction to Elastomers

Elastomers (also called rubber) are essentially supercondensed gases because most precursor monomers are gases. Their density is greater by approximately 3 orders of magnitude, and viscosity by 14 orders, than the gaseous state. Through polymerization, a long-chain molecule is created which is the primary structure of any polymeric material. The molecules can be arranged in an amorphous (rubbery), glassy, or crystalline phase. Elastomers are typically categorized as amorphous polymers having a random-coil molecular arrangement (Bhowmick and Stephens, 2001), (Harper, 1996), (Walker, 1979).

To give rubber a permanent shape the molecules are tied together by a few chemical bonds, in a process known as “crosslinking” or “vulcanization”. Molecular sequences or strands between interlinking sites still move about and change their shapes, but they are subject to a restriction caused by crosslinks, which remain in more or less stationary positions. Before crosslinking, rubber is basically a very viscous, elastic liquid. In contrast, after crosslinking, rubber is a soft and highly elastic solid.

We consider Fig. 2.1, which is a tensile stress-strain diagram for three physical states of a polymer: glassy, crystalline, and rubbery. Glassy polymers are hard and brittle. Crystalline polymers go through a succession of changes including elastic deformation, yield, plastic flow, necking, strain hardening, and strain fracture. As compared to the above two categories of polymers, an elastomer is unique because it is soft, highly extensible, and highly elastic.

Table 2.1 illustrates the unique mechanical and thermal properties of elastomers, compared to other engineering materials. Elastomers have a very low elastic modulus and high percent of elongation before fracture. Elastomers also have very low thermal conductivity. Under cyclic loading, elastomers exhibit significant hysteresis, which contributes to their energy absorption capability. The deformation of elastomers can be considered to be non-linear in terms of both their material and geometric behavior. Elastomers are isotropic, highly deformable, highly elastic, nearly incompressible, hyperelastic or Green elastic, which means that their mechanical properties can be characterized by means of a strain energy function. In addition, the mechanical behavior of elastomers is very complex due to their sensitivity to strain, strain-rate, deformation history, temperature, and the fabrication process (Gent, 2001).

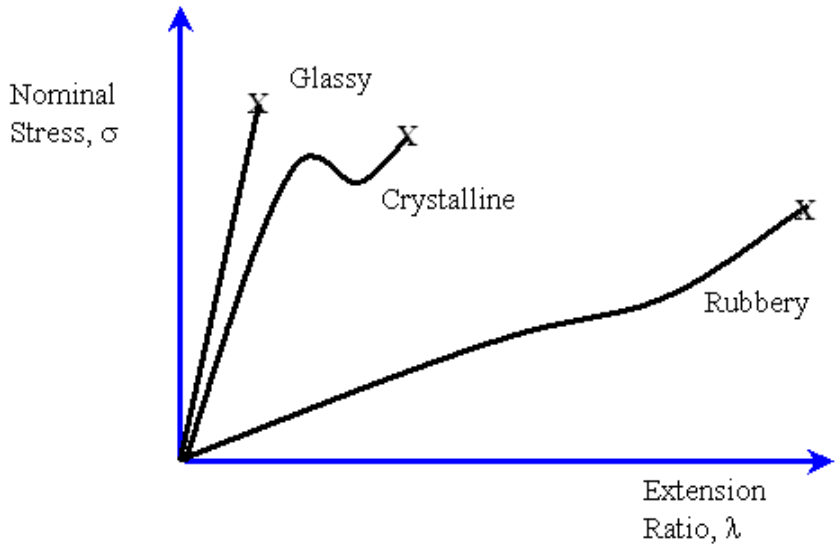

Figure 2.1. Tensile stress strain curves for polymers in three physical states.

Table 2.1. Comparison of the properties of elastomers and other materials (Lewis, 2002)

Material	Elastic modulus (GPa)	Poisson's ratio	Ultimate stress (MPa)	% of elongation to fracture	Thermal conductivity (W/m K)
Elastomers	0.0007 – 0.004	0.47 – 0.5	7 – 20	100 – 800	0.13 – 0.16
Aluminum alloys	70 – 79	0.33	100 – 550	1 – 45	177 – 237
Steel, high-strength	190 – 210	0.27 – 0.3	550 – 1200	5 – 25	35 – 60
Titanium alloys	100 – 120	0.33	900 – 1200	10	7 – 7.5
Plastic, Nylon	2.1 – 3.4	0.4	40 – 80	20 – 100	0.3
Plastic, Polyethylene	0.7 – 1.4	0.4	7 – 28	15 – 300	0.4

2.1.1. Elastomer Types

Elastomer can be broadly divided into two types: thermosets and thermoplastics. Thermosets are three-dimensional molecular networks, with the long molecules held together by *chemical* bonds. They absorb solvents and swell, but do not dissolve; furthermore, they cannot be reprocessed simply by heating. The molecules of a thermoplastic elastomer, on the other hand, are not connected by primary chemical bonds. Instead, they are joined by the *physical* aggregation of parts of molecules into hard domains. Hence, thermoplastic elastomers dissolve in suitable solvents and they soften during heating, so they can be reprocessed repeatedly. In many cases thermoplastic and thermoset elastomers may be used interchangeably. However, in demanding uses, such as in tires, engine mounts, and springs, thermoset elastomers are used exclusively because of their superior elasticity, resistance to set, and durability (Gent, 2001).

2.1.2. Compounding

The addition of various chemicals to raw rubber to impart desirable properties is termed rubber compounding or formulation. Typical ingredients include crosslinking agents, reinforcements, anti-degradants, and colorants. Because thermoplastic rubber contains hard domains that interconnect the molecules and impart strength and elasticity, they do not require crosslinking agents or reinforcing fillers. However, the selection of appropriate crosslinking agents and fillers is critical to the performance of thermoset elastomers. None of the elastomers have useful properties until they have been properly formulated. An unformulated elastomer is basically a high molecular weight liquid with low elasticity and strength. Although the molecules are entangled, they can readily disentangle upon stressing, leading to viscous flow. Vulcanization or curing is the process in which the chains are chemically linked together to form a network, thereby transforming the material from a viscous liquid to a tough elastic solid. After vulcanization, the strength and modulus increase, while hysteresis decreases. The most widely used vulcanizing agent is sulfur (Long, 1985).

Mechanical properties of an elastomer depend strongly on crosslink density. The modulus and hardness increase monotonically with increasing crosslink density. The crosslink density can be determined from swelling or mechanical measurements. For unfilled elastomers, the Flory-Rehner equation is widely used to relate the amount of swelling to the crosslink density (Flory, 1953):

$$N' = -\frac{1}{2V_s}\frac{\ln(1-\nu_r)+\nu_r+\chi\nu_r^2}{\nu_r^{1/3}-\nu_r/2} \qquad 2.1$$

where N' is the number of moles of crosslinks per unit volume, V_s is the molar volume of the swelling solvent, ν_r is the volume fraction of rubber in the swollen gel, and χ is the polymer-solvent interaction parameter. For vulcanizates containing reinforcing fillers such as carbon black, ν_r in the Floty-Rehner equation may be obtained from the following expression derived by Kraus:

$$\frac{\nu_r}{\nu_{rf}} = 1-\left\{3c\left[1-\nu_r^{1/3}\right]+\nu_r-1\right\}\frac{\phi}{1-\phi} \qquad 2.2$$

where ν_{rf} is the volume fraction of filled elastomer in the swollen gel, ϕ is the volume fraction of filler in the unswollen filled elastomer, and c is the filler-elastomer interaction parameter (Ciullo and Hewitt, 1999).

Crosslink densities of unfilled elastomer can also be determined from equilibrium stress-strain measurements using the following equation:

$$\frac{\sigma}{2\left(\lambda-\lambda^{-2}\right)} = C_1 + \frac{C_2}{\lambda} \qquad 2.3$$

where σ is the engineering stress, λ is the extension ratio, and C_1, C_2 are elastic constants. By plotting $\sigma/2\left(\lambda-\lambda^{-2}\right)$ versus $1/\lambda$ and extrapolating to $1/\lambda = 0$, a value of C_1 can be obtained at the intercept. From the theory of elastomer elasticity, $C_1 = N'RT$, where N' is the crosslink density, R is the gas constant, and T is the absolute temperature. To assure

near equilibrium response, stress-strain measurements are carried out at a low strain rate (Ciullo and Hewitt, 1999).

When an elastomer is deformed by an external force, part of the input energy is stored elastically in the chains and is available (released upon crack growth) as a driving force for fracture. The remainder of the energy is dissipated through molecular motions into heat, and in this manner, is made unavailable to break chains. At high crosslink levels, chain motions become restricted, and the tight network is incapable of dissipating much energy. This results in relatively easy and brittle fracture at low elongation. Elastomers have an optimum crosslink density range for practical use. Crosslink levels must be high enough to prevent failure by viscous flow, but low enough to avoid brittle failure.

Particulate fillers can increase the strength of an amorphous elastomer more than 10-fold. For a filler to cause significant reinforcement, it must possess high specific surface area, i.e., the particles must be small and less than 1μm in size. Small particles have large surface area to interact with the rubber and close particle-to-particle spacing in the compound. Two types of fillers that are most effective for reinforcing rubber are carbon black and silica. They can be produced with a primary particle size as small as 0.1μm, corresponding to a surface area of a few hundred square meters per gram of filler (Gent, 2001).

2.1.3. Mechanical Properties of Elastomers - Linear Elastic

An elastomer consists of long flexible molecules that are in continuous Brownian motion at normal temperatures due to thermal agitation. When the molecules are straightened out by an applied force and released, they spring back to random shapes as fast as their thermal motion allows. This is the origin of the unique ability of rubber to undergo large elastic deformations and recover completely: elastomer molecules are highly flexible and therefore, highly extensible, but in the absence of an external force they adopt rather compact and random configurations.

Although elastomers have the unique ability to undergo large deformations, in practice many rubber springs are subjected only to relatively small strains of less than about 25% in extension and compression, or 75% in simple shear. A good approximation for the corresponding stresses is then given by conventional elastic analysis, assuming simple, linear, stress-strain relationships, because like all solids, rubber behaves as a linearly elastic substance at small strains. Thus, many common rubber design problems can be treated by knowing only the value of the modulus of elasticity. Elastic materials that are isotropic in their undeformed state can be described by two fundamental elastic constants. The first deals with their resistance to compression in volume under hydrostatic pressure, termed the modulus K of bulk compression. It is defined by the following relation between the applied pressure P and the consequent shrinkage, ΔV of the original volume V_o: $P = K\left(\frac{-\Delta V}{V_o}\right)$.

The second constant describes the resistance to a simple shearing stress t, termed the shear

modulus G. It is defined by the relation: $G = t/\gamma$ where γ is the amount of shear, defined as the ratio of the lateral displacement d to the height h of the sheared block.

Other commonly used elastic constants can be derived from these two. The tensile modulus E (Young's modulus of elasticity), defined by the ratio of a simple tensile stress t to the corresponding fractional tensile elongation ε, is given by $E = \frac{t}{\varepsilon} = \frac{9KG}{3K+G}$. Poisson's ratio ν, is defined by the ratio of lateral contraction strain to longitudinal tensile strain for a bar subjected to a simple tensile stress, which is given by $\nu = \frac{1}{2}\frac{3K-2G}{3K+G}$.

Rubber solids have high values of bulk compression modulus K, but the shear modulus G is typically rather low, only about 0.5 to 5 Mpa, which is two to three orders of magnitude smaller than K. Thus Poisson's ratio ν is close to one half (typically 0.499) and the tensile modulus E of elasticity is given almost exactly by 3G. If an elastomer is considered to be completely incompressible in bulk ($\nu = \frac{1}{2}$) then the elastic behavior at small strains can be described by a single elastic constant given by G. Note that when an elastomer block is "compressed", its volume does not decrease significantly unless the pressures are extremely high. Instead, the block expands laterally and the elastomer volume remains virtually unchanged.

The elastic modulus of elastomer is often characterized indirectly by measuring the elastic indentation caused by a rigid indentor of prescribed size and shape, either a truncated cone or

a sphere, pressed into the surface under specified loading conditions. Various nonlinear scales are employed to derive a value of "rubber hardness" from such measurements. Hardness values range from zero degrees when the modulus is zero, up to 100 degrees when the modulus is infinitely high. Corresponding values of modulus E are given in Table 2.2 (Briscoe, and Sebastian, 1993).

Table 2.2. Relationship between indentation hardness and elastic modulus E

Hardness (Degrees)	E (Shore) (Mpa)
10	0.4
20	0.7
30	1.2
40	1.7
50	2.5
60	3.8
70	6
80	10
90	23

Classical results for indentation of an elastic block assume that the block is much thicker than a characteristic dimension of the indentor (e.g. the radius of a spherical indentor) and much thicker than the amount of indentation. With these limitations in mind, the following relations hold between indenting force F and amount of displacement d of the rubber surface under an indentor:

For a flat-ended cylindrical punch of radius a (Timoshenko and Goodier, 1970),

$$F = 8Ead \tag{2.4}$$

For a spherical indentor of radius a,

$$F = \left(\frac{16}{3}\right) E a^{1/2} d^{3/2} \qquad 2.5$$

For a conical indentor with semi-angle of θ (Sneddin, 1975),

$$F = \left(\frac{8}{\pi}\right) E d^{2} \tan\theta \qquad 2.6$$

In each of these relationships the rubber is assumed to be completely incompressible. For compressible materials, the right hand sides are divided by the factor $2(1-\nu)$.

2.1.4. Mechanical Properties of Elastomers - Non-linear Elastic

Some features of elastomers can be understood only in terms of its response to large deformations. Therefore, there is a need to know how to characterize the elastic behavior of highly extensible, nonlinearly elastic materials. A simple modulus of elasticity is no longer sufficient. The theory of large elastic deformations is necessary to analyze the behavior of elastomer under large deformation.

The initial orientation of the long-chain molecules in elastomeric materials is assumed to be random; therefore, the material is initially isotropic. As the material is stretched, the molecules orient themselves, giving rise to anisotropy. However, the development of this anisotropy follows the direction of straining; hence, the material can be considered to be isotropic throughout the deformation history. As a consequence, the strain energy potential can be formulated as a function of the strain invariants. Symmetry considerations suggest

that appropriate measures of strain, independent of the choice of axes, are given by three strain invariants defined as follows:

$$\begin{aligned} J_1 &= \lambda_1^2 + \lambda_2^2 + \lambda_3^2 - 3 \\ J_2 &= \lambda_1^2\lambda_2^2 + \lambda_2^2\lambda_3^2 + \lambda_1^2\lambda_3^2 - 3 \\ J_3 &= \lambda_1^2\lambda_2^2\lambda_3^2 - 1 \end{aligned} \qquad 2.7$$

where the symbols $\lambda_1, \lambda_2, \lambda_3$ denote the principal stretch ratios, defined as the ratio of stretched length to unstretched length of the edges of a small volume element, cubical in the unstrained state. Thus the values of λ_i are given by $(1+\varepsilon_i)$ where ε_i is the corresponding principal extension and the values of J_i become zero in the unstrained state when $\lambda_1 = \lambda_2 = \lambda_3 = 1$. Moreover, for an incompressible material, J_3 is identically zero; hence, only two independent measures of strain, namely J_1 and J_2, remain. It follows that the strain energy density W (i.e., the amount of energy stored elastically in a unit volume of material under the state of strain specified by $\lambda_1, \lambda_2, \lambda_3$) is a function of J_1 and J_2 only: $W = W(J_1, J_2)$. Furthermore, when the function of W is expanded as a power series in terms of J_1 and J_2, the strain energy function at sufficiently small strains must take the form

$$W = C_1 J_1 + C_2 J_2 \qquad 2.8$$

where C_1 and C_2 are constants. This particular form of strain energy function was originally proposed by Mooney and is often called Mooney-Rivlin equation. Because J_1 and J_2 are of second order in the strains ε_i, the above equation is valid for a greater range of strains than classical small-strain elasticity theory, which neglects terms of higher order than ε_i. However, strains of more than about 25% give rise to fourth-order terms that cannot be neglected. Thus, it does not apply to strains of a size commonly encountered. It applies only

for a limited range of strains, much less than unity. To include all terms of order J^2 (i.e., all terms of order ε_i^4), it would be necessary to include nine terms in the relation for W for compressible elastic solid, reducing to five terms for incompressible elastic solid. Thus, it would require five elastic coefficients to include all terms of order ε^4 in the strain energy function for rubber. Because it is difficult in practice to determine the values of more than two or three elastic coefficients with any accuracy, a power-series expansion for W using more than two or three terms has not been widely employed (Gent, 2001).

2.2. Elastomer Mechanics Models

In general, the elasticity of elastomers can be studied in three categories; namely, a thermodynamic approach, a statistical approach and a phenomenological treatment. The first thermodynamic treatment is only concerned with the macroscopic behavior of the material, rather than the molecular behavior. The second approach considers statistical mechanics that underlie elastomeric molecular dynamics. The phenomenological approach, which is widely used today, provides a description of the elasticity for large deformation. As its name implies, the phenomenological approach is concerned only with observed behavior, not with the mechanism responsible for that behavior. Its primary aim is to provide a means of calculating the relationships between the state of strain in a deformed body and the applied forces. A secondary aim is to find a general description of material properties in terms of the elastic energy stored in the system. The elastic energy stored after the deformation in a system is a unique state function of strain and it is independent of the strain path. The state

of strain is defined by three principal stretch ratios, denoted by λ_1, λ_2, and λ_3 (ABAQUS Theory Manual, 2002).

There are several forms of strain energy potentials available to model approximately incompressible isotropic elastomers: the Arruda-Boyce form, the Mooney-Rivlin form, the neo-Hookean form, the Ogden form, the polynomial form, the reduced polynomial form, the Yeoh form, and the Van der Waals form. The reduced polynomial and Mooney-Rivlin models can be viewed as particular cases of the polynomial model; the Yeoh and neo-Hookean potentials, in turn, can be viewed as special cases of the reduced polynomial model. The detailed relationships among various hyperelastic material models are plotted in Fig. 2.2 below.

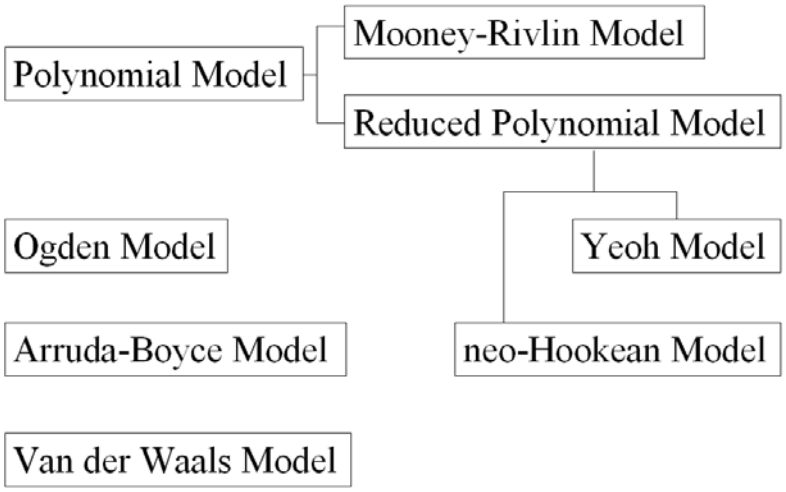

Fig. 2.2. Relationships among various hyperelastic material models.

Generally, when data from multiple experimental tests are available (typically, this requires at least uniaxial and equibiaxial test data), the Ogden and Van der Waals forms are more

accurate in fitting experimental results. If limited test data are available for calibration (usually uniaxial tension data only), the Arruda-Boyce, Van der Waals, or reduced polynomial forms provide reasonable behavior and are recommended.

Given isotropy and additive decomposition of the deviatoric and volumetric strain energy contributions in the presence of incompressible or almost incompressible behavior, the potential can be written in general in a polynomial form. The form of the polynomial strain energy potential is

$$W = \sum_{i+j=1}^{N} C_{ij} {J_1}^{i} {J_2}^{j} + \sum_{i=1}^{N} \frac{1}{D_i} {J_3}^{2i} \qquad 2.9$$

The parameter can assume values up to six; however, values of greater than 2 are rarely used when both the first and second invariants are taken into account.

If N=1, only the linear terms in the deviatoric strain energy are retained, the Mooney-Rivlin form is recovered. The form of the Mooney-Rivlin strain energy potential for compressible elastic solid is (Mooney, 1940)

$$W = C_1 J_1 + C_2 J_2 + \frac{1}{D_1} {J_3}^{2} \qquad 2.10$$

The Mooney-Rivlin form can be viewed as an extension of the neo-Hookean form in that it adds a term that depends on the second invariant. In some cases this form will give a more accurate fit to the experimental data than the neo-Hookean form; in general, however, both models give similar accuracy since they use only linear functions of the invariants. These functions do not allow representation of the "upturn" at higher strain levels in the stress-strain curve.

Particular forms of the polynomial model can also be obtained by setting specific coefficients to zero. If all C_{ij} with $j \neq 0$ are set to zero, the reduced polynomial form is obtained. The form of the reduced polynomial strain energy potential is

$$W = \sum_{i=1}^{N} C_i J_1^{\ i} + \sum_{i=1}^{N} \frac{1}{D_i} J_3^{\ 2i} \qquad 2.11$$

The Yeoh form can be viewed as a special case of the reduced polynomial with N=3. The form of the Yeoh strain energy potential is (Yeoh, 1993)

$$W = C_1 J_1 + C_2 J_1^{\ 2} + C_3 J_1^{\ 3} + \frac{1}{D_1} J_3^{\ 2} + \frac{1}{D_2} J_3^{\ 4} + \frac{1}{D_3} J_3^{\ 6} \qquad 2.12$$

If the reduced-polynomial strain-energy function is simplified further by setting N=1, the neo-Hookean form is obtained. The form of the neo-Hooken strain energy potential is

$$W = C_1 J_1 + \frac{1}{D_1} J_3^{\ 2} \qquad 2.13$$

This form is the simplest hyperelastic model and often serves as a prototype for elastomeric materials in the absence of sufficient material data.

The Ogden strain energy potential is expressed in terms of the principal stretches. The form of the Ogden strain energy potential is (Ogden, 1986)

$$W = \sum_{i=1}^{N} \frac{2\mu_i}{\alpha_i^2} (\bar{\lambda}_1^{\alpha_i} + \bar{\lambda}_2^{\alpha_i} + \bar{\lambda}_3^{\alpha_i} - 3) + \sum_{i=1}^{N} \frac{1}{D_i} J_3^{\ 2i} \qquad 2.14$$

If $N = 2$, $\alpha_1 = 2$, and $\alpha_2 = -2$, the Mooney-Rivlin model is obtained. If $N = 1$, and $\alpha_1 = 2$, Ogden model degenerates to the neo-Hookean material model.

The form of the Arruda-Boyce strain energy potential is (Arruda and Boyce, 1993)

$$W = C_1\left\{\frac{1}{2}(I_1-3)+\frac{1}{20C_2^2}(I_1^2-9)+\frac{11}{1050C_2^4}(I_1^3-27)+\frac{19}{7000C_2^6}(I_1^4-81)+\frac{519}{673750C_2^8}(I_1^5-243)\right\}$$
$$+\frac{1}{D_1}\left(\frac{I_3^2-1}{2}-\ln I_3\right) \qquad 2.15$$

The Arruda-Boyce potential depends on the first invariant only. The physical interpretation is that the eight chains are stretched equally under the action of a general deformation state. The first invariant, $I_1 = \lambda_1^2 + \lambda_2^2 + \lambda_3^2$, directly represents this elongation.

The form of the Van der Waals strain energy potential is (Treloar, 1975)

$$W = \mu\left\{-(\lambda_m^2-3)[\ln(1-\eta)+\eta]-\frac{2}{3}a(\frac{\tilde{I}-3}{2})^{3/2}\right\}+\frac{1}{D}\left(\frac{J_3^2}{2}-\ln(J_3+1)\right) \qquad 2.16$$

where $\tilde{I} = (1-\beta)(J_1+3)+\beta(J_2+3)$ and $\eta = \sqrt{\frac{\tilde{I}-3}{\lambda_m^2-3}}$

2.3. Experimental Study of Machining Processes

Machining processes involve the removal of layers from a workpiece in the form of a chip by action of a wedge shaped cutting tool. Those processes are dependent on the workpiece parameters (material type, crystallography, temperature, pre-deformation), cutting tool parameters (tool design geometry, material), and cutting parameters (speed, feed, depth of cut, environment). Some studies have been done that include the influence of only a few specific topics, and other more advanced studies have been conducted to understand the complex physical behavior underlying the specific machining process (Athavale and Strenkowski, 1997), (Guo and Liu, 1999), (Guo and Dornfeld, 2000), (Lo, 2000). In general,

machining experiments can be used for studying the relationships among various parameters such as cutting forces, chip morphology, and cutting parameters. They are also often used to verify the numerical models such as finite element models for cutting and achieve material properties for various conditions.

Two basic cutting operations are normally considered: orthogonal (two force) models and oblique (three force) modes. Orthogonal cutting process is the most simplified process without losing the nature of cutting. It is easier to analyze and can be useful or adequate for understanding the basic mechanics of machining processes. In orthogonal cutting, the cutting edge of the tool is perpendicular to the direction of the workpiece material velocity vector as shown in Fig. 2.3. There are some practical orthogonal cases such as some finishing planer cuts, surface broaching, the lathe cut-off operation, and some plain-milling operations, although most commercial tools are three-dimensional. These include a conventional lathe tool, a face-milling cutter, and a twist drill. As shown in Fig. 2.4, oblique cutting refers to cutting when the cutting edge of the tool is oblique or at an angle to the movement of the relative workpiece-tool direction (Shaw, 2005).

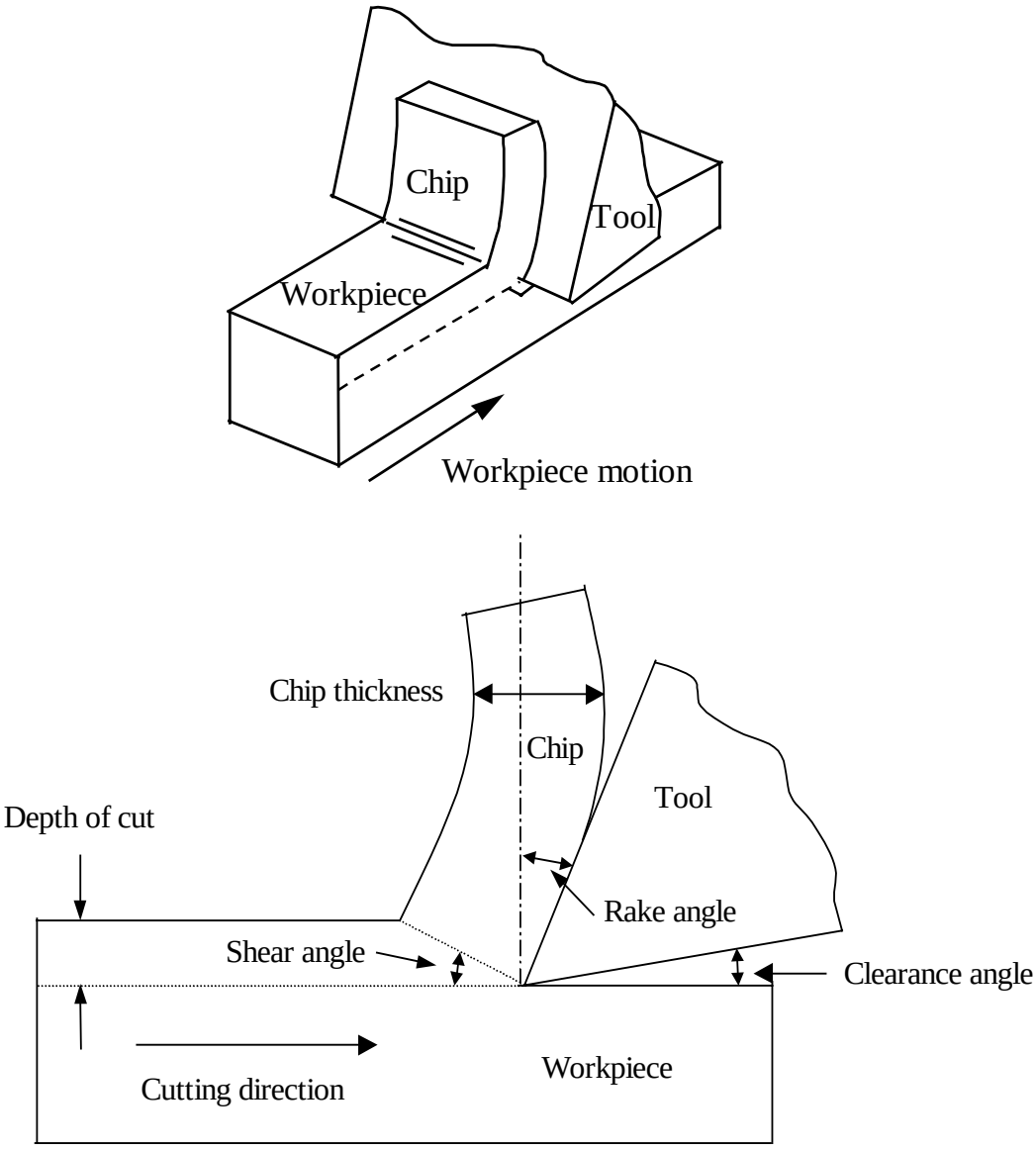

Figure 2.3. Orthogonal cutting process.

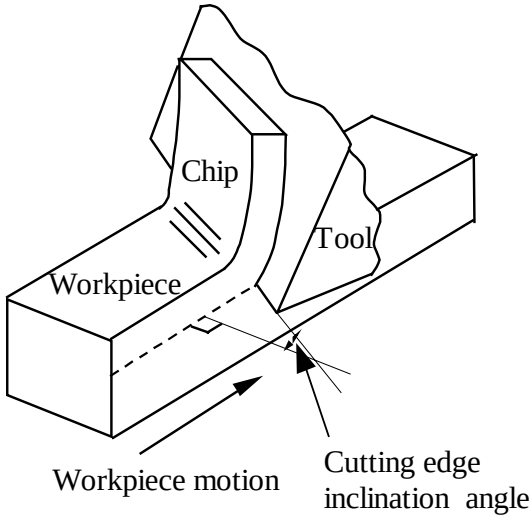

Figure 2.4. Oblique cutting process.

Extensive experimental studies have been conducted on the cutting of metal materials. Usui et al. (Usui et al., 1978) developed an analytical model of three-dimensional cutting with a single-point tool. In this method, empirical relations must be established from orthogonal machining tests and validated before they are extended to three-dimensional machining. Oxley (Oxley, 1989) used a carefully designed machining test to develop an effective method for predicting a material's flow stress behavior. Orthogonal machining experiments were conducted using low carbon steels as test specimens. Strenkowski and Mitchum used experimental incipient cutting tests for 70/30 Brass to verify an updated Lagrangian finite element model (Strenkowski and Mitchum, 1987). Cutting experiments for aluminum alloy 6061-T6 also were performed by Strenkowski and Moon to validate an Eulerian finite element model for orthogonal cutting (Strenkowski and Moon, 1990). A series drilling tests on AISI 1020 steel for several drilling diameters, spindle speeds and feed rates were conducted by Strenkowski and Hsieh to validate an analytical finite element technique for

predicting the cutting and thrust forces in drilling with twist drills (Strenkowski and Hsieh, 2004). In contrast, very little experimental research on rubber machining has been reported because of the material complexity of rubber and the machining process itself. High speed rubber milling experiment was conducted by Jin and Murakawa (Jin and Murakawa, 1998). They used several carbide end mill tools of various sizes and helix angles to cut grooves on three types of soft rubber, H-NBR, Norbornone rubber and silicone rubber, at various speeds. Better surface quality in terms of roughness and flatness was observed for machining at high speeds with high helix angle cutters. Lewis conducted a series of milling tests on ambient and solid carbon dioxide cooled rubber plates with woodworking tools of different geometries (Lewis, 2002).

Fixture design and tool shape were found to be crucial in producing a clean groove surface. A specially designed fixture was used in the experiments to overcome excessive motion of the workpiece material due to rubber's low modulus. A finite element model of the structure generated by the ANSYS code was used to analyze the overall structure stiffness. Chips were classified as six types, such as burned (B) and rough flat (RF), based on their sizes and shapes measured by SEM. Cutting forces were also measured using a dynamometer for machining of rubbers under room temperature and dry ice cooled conditions. Larger forces were observed for cryogenic cutting due to the increased stiffness of rubber under low temperatures. The possibility of adiabatic shear band formation in serrated chip formation due to the low thermal conductivity of rubbers was also suggested. This study provides valuable information on the milling of elastomers for use in later investigations of the machining mechanics of rubbers. Recently, Strenkowski and Rodkwan performed a series of

orthogonal turning experiments on elastomers with high-speed steel (HSS) tools of various geometries for different cutting parameters (Rodkwan, 2002). Both continuous and discontinuous chips were observed for the range of experimental parameters. Large rake angles, cutting speeds and feed rates were found helpful in generating a smooth surface finish.

It is known that rubber is a so-called hyperelastic or super elastic material with an extremely small modulus. These materials have distinct material characteristics as compared to metallic materials. Therefore, there are many significant differences between the machining of metals and elastomers. For example, rubber has a temperature sensitive stiffness and low thermal conductivity. Cryogenic machining has been shown to be an efficient method for machining elastomers to achieve good surface quality (Lewis, 2002). A well designed fixture also plays an important role in increasing the stiffness of the rubber workpiece for achieving good surface quality. In contrast to machining of metals, sharp tools with small included angles are always recommended for machining rubber materials (Rodkwan, 2002). These factors are important considerations when investigating the machining of elastomers.

2.4. Finite Element Analysis (FEA) of Elastomer Machining

The numerical analysis of elastomer machining process has not been widely conducted. In contrast, the metal cutting process has been studied extensively for a long time due to the wide application of metals as an important industrial material. Therefore, it is helpful to review the historical development of the use of FEA for understanding the metal cutting

process first as a foundation for developing a similar FEA model for elastomer machining processes.

It is known that many simple metal cutting problems can be solved with analytical methods. For example, much effort has been devoted to developing analytical models of orthogonal metal cutting throughout the 1900's. In 1941, Ernst and Merchant developed models that related the so-called shear plane angle to the tool rake angle and the coefficient of friction between the chip and the tool rake face. The analytical model was found to give good agreement for polymeric materials, but it was a poor model for machining of steel. Lee and Shaffer developed a more sophisticated model by introducing plasticity of the workpiece material. The material was assumed to be rigid-perfectly plastic. A slip-line theory was used, in which a plane triangular region was assumed to exist near the tool tip. In this zone, no deformation occurred but the material was stressed to its yield. There are other shear zone solutions in the literature based on these early models (Shaw, 2005).

The lack of agreement of these models with experiment has led researchers to reexamine the features that have been ignored in these models. These effects include more sophisticated models of the frictional behavior on the tool rake face, high strain-rates and work-hardening of the workpiece material, and the effect of extreme temperatures on the workpiece material properties. In summary, these simplified orthogonal metal cutting models only provide a first order approximation of certain metal parameters and they are not highly accurate. Attempts by researchers to improve the model by including a more realistic description of the friction phenomenon, temperature field, high strain-rate, and large strains have not been

successful. As the geometry becomes more complex, the techniques and assumptions used oversimplify the problem or result in equations that are not applicable or impossible to solve.

A more promising approach for developing an orthogonal metal cutting model is provided by the finite element method. The finite element method (FEM) is one of the most accurate, versatile, and comprehensive methods for solving complex problems. The finite element technique has been extensively used since its formulations were well established. Unlike analytical methods, this method permits the analysis of complex structures without the necessity of developing and solving complex equations. A large number of commercial FEM packages, such as ABAQUS, ANSYS, NASTRAN and IDEAS, have been successfully implemented and applied to various industries and academic areas. In academic and research fields, some researchers have developed special-purpose in-house finite element codes for specific research problems.

For example, several finite element formulations have been developed for elastic-plastic metal cutting problems which provide for temperature-dependent material properties and high strain rates. Specifically, Strenkowski and Carroll developed an orthogonal cutting model using an updated-Lagrangian elasto-plastic implicit dynamic formulation with modified NIKE2D code (Strenkowski and Carroll, 1985, 1986). This work introduced a new chip separation criterion based on the effective plastic strain. It also included several cutting parameters, such as elastic-plastic material properties of the workpiece and tool, friction along the tool rake face, and geometry of the cutting edge and workpiece. The model predicts chip geometry, residual stress in the workpiece, and tool stresses and forces without

empirical metal cutting data. However, since the mesh was attached to the workpiece being modeled, it could cause large element distortion problems in the workpiece. Also, a prescribed chip separation criterion based on effective strain must be known in advance. Although the model was improved by Strenkowski and Mitchum (Strenkowski and Mitchum, 1987), the accuracy was limited by the size of the elements in the vicinity of the cutting edge.

In the Lagrange formulation, material particles are fixed to the finite element grid. This may cause problems when the deformations are severe. Strenkowski and Carroll introduced an alternative Eulerian approach for simulating a flat tool based on the work of Zienkiewicz (Strenkowski and Carroll, 1986). In this study, the workpiece and tool were treated as a control volume with a stationary grid that can be refined as necessary at the tool cutting edge where the stress and strain gradients are the highest. The workpiece was treated as a viscoplastic material in which the material can flow through the control volume. The model included temperature prediction for heat that is generated due to plastic work and friction. Friction along the tool rake face was also included in the model. Cutting experiments were performed for aluminum alloy 6061-T6 to validate the model. Good correlation with the model was found based on tool forces and average tool-chip interface temperature measurements. With an assumed chip geometry, the Euleraian formulation is more efficient for simulating steady-state orthogonal cutting. To capture the generality of the Lagrangian formulation and the efficiency of the Euleraian formulation, Strenkowski and Moon proposed a coupled Lagrangian-Eulerian finite element model (Strenkowski and Moon, 1990). By defining relative velocities between particle velocities of the finite element grid, they formulated a set of momentum equations which were applied to both the Lagrangian and

Eulerian description of the flow field. In their formulation, the workpiece was modeled as an elastic-plastic material. The model was limited to steady state with no temperature effects. The restriction of a predefined tool-chip contact that existed in these models was later modified by Athavale and Strenkowski (Athavale and Strenkowski, 1997). Further development of the cutting model was carried out by Hsieh and Strenkowski to improve the model accuracy and capability for use in cutting tools with large negative rake angles (Strenkowski and Hsieh, 2004). In this work, a three-dimensional twist drill model was developed in conjunction with an analytical single edge oblique cutting model. Drilling forces, torque and temperature distribution in the drill body were calculated in this investigation.

The development of a plane strain finite element method for the simulation of orthogonal metal cutting with continuous chip formation was also carried out by Shih using an in-house code. The effects of elasticity, viscoplasticy, temperature, friction, large strain, and high strain rate were used to simulate the material deformation during the cutting process. Several special techniques for finite element simulation of metal cutting processes, such as element separation and mesh rezoning, were used to enhance the computational accuracy and efficiency. The cutting process was analyzed using an unbalanced force reduction method and a stick-slip friction model. The predicted residual stress distribution was correlated with X-ray diffraction measurements on annealed 1020 carbon steel samples for various rake angles. In summary, Table 2.3 shows a summary of the literature of metal cutting simulations using finite element methods (Wang, Sadat and Twu, 1988).

Table 2.3. Summary of literature in metal cutting simulation using finite element methods

		Klamecki (1973)	Shirakashi Usui(1974)	Usui (1978)	Lajczok (1980)	Shirakashi Usui(1982)	Iwata (1984)	Strenkowski Carroll(1985)	Strenkowski Carroll(1986)	Carroll (1986)	Strenkowski Mitchum(1987)	Strenkowski Moon(1987)
Method	2D		X		X	X	X	X	X	X	X	X
	3D	X		X								
	Lagrangian	X	X		X	X	X	X		X	X	
	Eulerian								X	X		
	Coupled											X
	Transient	X					X			X		
	Steady		X	X	X	X			X	X		X
Assumptions	Chip geometry		X	X	X	X	X		X	X		X
	Tool force				X							
	Flow line		X			X						
Material Model	Rigid-plastic						X					
	Elastic-plastic	X	X		X	X		X		X	X	
	Visco-plastic								X			
	Elastic-viscoplastic											X
	Thermal effect		X		X	X		X	X	X		
Parameters	Depth	X		X	X			X		X	X	X
	Speed	X			X			X	X	X		
	Feed			X	X					X	X	
	Rake angle	X		X	X		X	X	X	X	X	X
	Friction		X					X	X	X		
Results	Stress		X			X	X	X		X	X	X
	Strain	X	X			X	X	X	X	X	X	X
	Residual stress				X			X		X	X	

	Plastic strain	X	X		X	X				X		
	Tool force			X				X	X	X	X	
	Shear angle						X					
	Chip initiation	X								X		
	Chip thickness							X		X	X	
Materials	Aluminum	X						X	X	X		X
	Copper	X			X					X		
	Brass	X	X			X						
	Steel					X	X					
	Babbitt			X								
Experimental comparison		X		X	X	X	X		X	X		

With the rapid growth of various commercial finite element programs, modeling of the cutting process can be readily achieved. Kalhori used the general finite element code ABAQUS/Standard to simulate the quasi-static adiabatic heat cutting process along a predetermined chip separation path for SANDVIK steel 1672-08. He also used an in-house adaptive, fully coupled thermo-mechanical code SiMPle with mesh smoothing facilities to compensate the major lacking capability in ABAQUS for adaptive meshing and arbitrary cracking. Guo and Liu simulated the 3D hard facing process using ABAQUS/Explicit code (Guo and Liu, 2002). A finite element prediction in terms of cutting forces and chip geometry agreed with the experimental data with reasonable accuracy using the material property data obtained from the proposed testing method. Guo and Dornfeld also used the ABAQUS/Explicit code to simulate the drilling burr formation process (Guo and Dornfeld, 2000). A nonlinear thermo-elastic-plastic model simultaneously accounted for dynamic effects of mass and inertia, strain hardening, strain rate, automatic mesh contact with friction capability, material ductile failure and temperature-mechanical coupling.

Several advantages with ABAQUS/Explicit code were mentioned including 1) good convergence for a large model 2) less computational cost and 3) capability of modeling complex contact conditions. The simulation results coincided with phenomenological observations of burr geometry from drilling 304 stainless steel and plastic work materials. Guo and Liu also developed an explicit 3D FE model to analyze hard turning of AISI 52100 steels using a PCBN cutting tool (Guo and Liu, 2002). The finite element model gave reasonable accuracy for chip geometry, forces, residual stresses, and cutting temperatures. The effect of sequential cuts on the residual stress in the machined layers was predicted using

a thermo-elastic viscoplastic finite element cutting model developed with ABAQUS/Explicit by Guo and Liu (Guo and Liu, 1999). In this work, chip formation, cutting forces, and temperatures were predicted for stainless steel. In another study, Yang and Liu used ABAQUS/Explicit code to perform analyses on a stress-based polynomial model of friction behavior in machining (Yang and Liu, 2002). Because the proposed model captured the relationship between the normal stress and shear stress on the tool rake face better than a conventional approach, it had a potential for improving the prediction of residual stress induced by machining.

Ng and Aspinwall presented a FE model using ABAQUS/Explicit to simulate continuous and segmental chip formation when machining AISI H13tool/die steel heat treated to 49HRC with PCBN tools (Ng and Aspinwall, 2002). The work utilized the shear failure criteria and element deletion/adaptive remeshing modules. The model was validated by experimental data involving chip morphology and cutting forces. Meske and Sauter used a combination of the optimization system TOSCA and nonlinear FE solver ABAQUS to optimize the design of tools in machining of elastomer-metal components. Both time and costs were reduced in the development of elastomer-metal components while maintaining high product quality. Recently, Timbrell et al. developed a FE model using the Zencrack code to simulate crack propagation in rubber in which the finite element mesh was adapted in the region of the crack tip as the crack propagated. ABAQUS was used as a solver to calculate the strain energy release rate at each increment in crack length. A three-dimensional analyses showed that the crack front developed a curvature during crack propagation.

2.5. Summary

Elastomers are typically divided into thermosets and thermoplastics, and thermosets are the most widely used type of elastomers. The crosslink density has a critical effect on an elastomer's properties, and it can be determined from formulae for both unfilled and filled elastomers. In the design of elastomer components, the linear elastic properties for an elastomer can be used when the deformation is within the linear elastic range. Hyperelastic material models are necessary when large deformations occur. Based on past research, it is known that commercial finite element analysis packages such as ABAQUS can be a useful tool for simulating the complexities of the cutting process. In this dissertation, a finite element model using ABAQUS/Explicit code and a user-supplied material subroutines are described for simulating the cutting process of elastomers.

3. ELASTOMER TURNING EXPERIMENTS

3.1. Introduction

A total of 66 dry turning tests were conducted on a conventional Republic Lagun CMZ lathe (type PERMIL-L-23250B) to study the mechanism of elastomer orthogonal cutting and gain a better understanding of favorable conditions that result in a good machined surface finish. Before any machining tests were conducted, a spindle speed calibration of the lathe was performed in order to ensure accurate cutting speeds. Cutting forces, including principal, thrust and transverse force components, and workpiece surface temperatures were recorded during the tests to study the effect of tool geometry and cutting speed. During the tests, chips were collected for subsequent analysis and the machined surface roughness was measured to evaluate the surface finish.

Although turning is a three-dimensional machining process, the orthogonality assumption greatly simplifies the geometry of the cutting analysis while retaining the material response characteristics of the workpiece and tool interaction. Therefore, orthogonality was considered to be an appropriate assumption for studying the elastomer cutting process. In fact, orthogonal cutting has been extensively studied for a long time for many other machining processes. Once the orthogonal cutting process is understood, more complex three-dimensional machining operations, such as oblique cutting, milling, and drilling, can be either directly derived or approximated as a series of oblique sections along the cutting edge (Strenkowski, Hseih and

Shih, 2004), (Strenkowski, Shih and Lin, 2002). Therefore, these complex processes can be readily analyzed by this discrete method.

In orthogonal cutting, chips flow along the tool rake face in two-dimensional plane strain without transverse motion. To obtain orthogonal machining conditions, a rubber tube with a large radius (inner diameter = 72 mm) and a significantly smaller thickness (11.6 mm) was cut by a tool with a zero inclination angle as shown in Fig. 3.1. The width of the tool (20 ~ 40 mm) is much greater than the width of the workpiece due to the large transverse deformation of the workpiece. In the experiments, the edge of the rubber tube overhung approximately 15 mm from the aluminum mandrel edge so that only the rubber was machined during the cutting tests. Cutting tools with four rake angles of 10°, 30°, 50°, and 75° and two clearance angles of 5° and 20° were used in the tests for three spindle speeds of 80, 320, and 550 rpm and three feed rates of 0.127, 0.254, and 0.508 mm/rev under two workpiece temperatures (ambient and dry-ice cooled). Note that these feed rates correspond to 0.005, 0.010 and 0.020 in/rev, respectively. In the following figures, units of in/rev are used because this is a commonly accepted unit for feed rate.

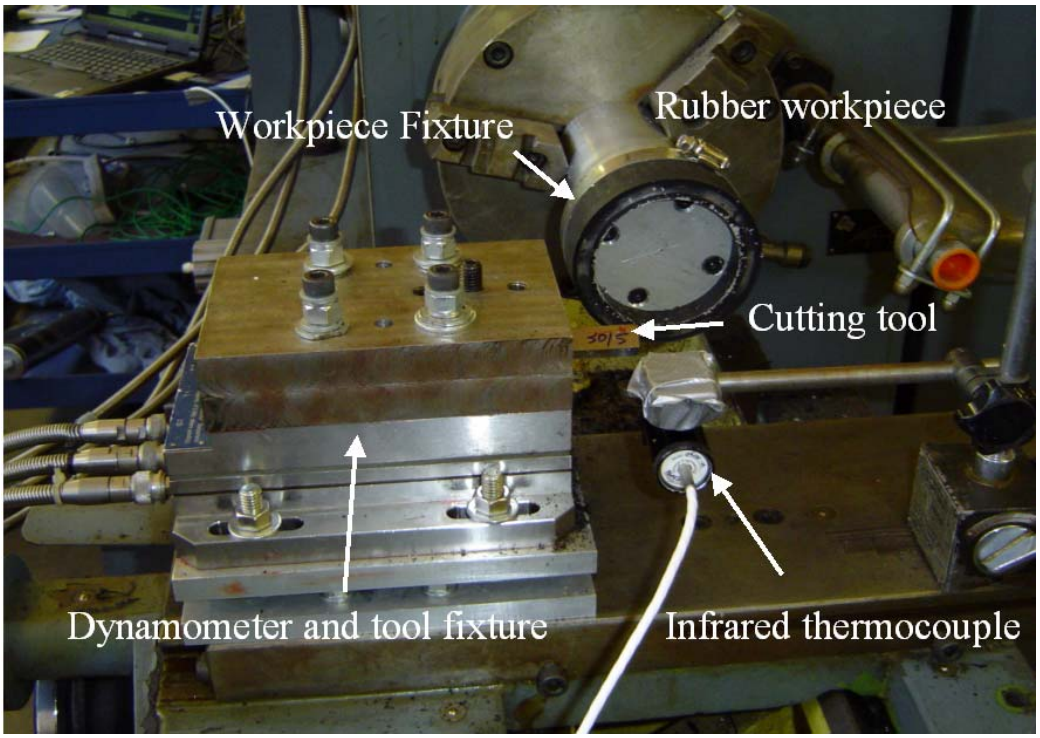

Figure 3.1. Experimental setup for elastomer cutting tests.

3.2. Experimental Setup

3.2.1. Fixture Design

Elastomers have a very low elastic modulus (1~10 MPa) as compared with 200 GPa for AISI 1020 steel. Elastomers exhibit large elastic deformation before rupture (500% for the elastomers used in the experiments). Based on previous end milling and orthogonal cutting tests, it has been shown that a stable fixture is necessary for producing a smooth surface finish for machined rubber (Shih, Lewis and Strenkowski, 2004), (Lewis, 2002). To achieve a stable condition for the elastomer workpiece, a mandrel was designed with a tapered region as shown in Fig. 3.2. The rubber workpiece was mounted on the mandrel by stretching it from its original

inner diameter of 72 mm to a final diameter of 77 mm, which is a little larger than its original diameter, and then sliding it over the tapered portion of the mandrel. The stretched workpiece provided adequate contact force between the workpiece and the mandrel. The contact force was further increased by applying a vacuum through the series of small holes. This vacuum-assist feature was especially effective for securing the rubber workpiece to the mandrel since rubber is often used as a sealing material in many practical applications. The vacuum applied to the inner chamber of the mandrel was well maintained during the cutting process by closing a valve in the end cap of the mandrel. A pipe clamp was also used to secure the rubber workpiece to the mandrel and prevent the workpiece from sliding. In addition, the rubber stiffness was further increased by cooling the workpiece in solid carbon dioxide before conducting the cutting tests.

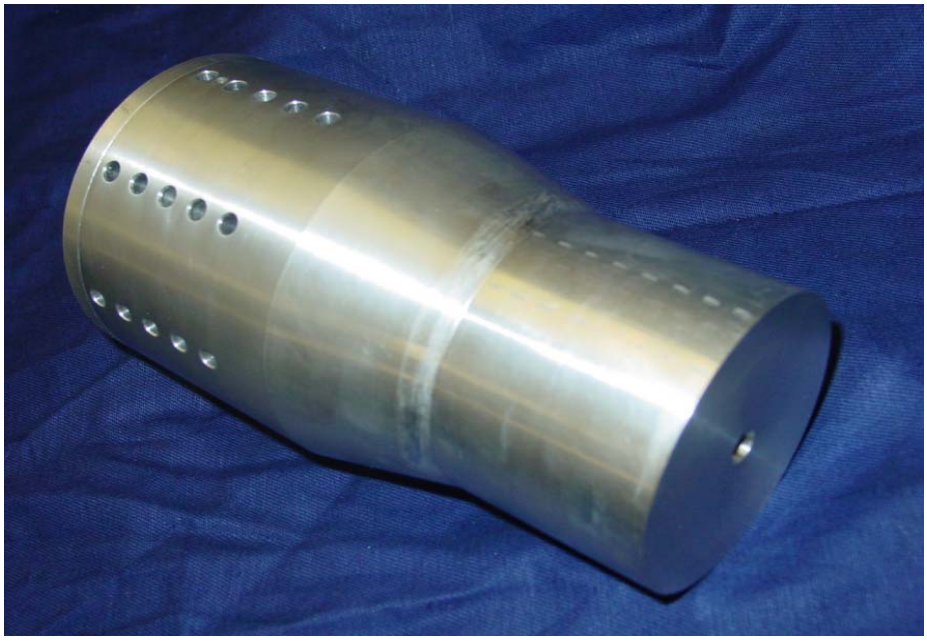

Figure 3.2. Specially designed fixture for elastomer cutting tests.

3.2.2. Cutting Force Measurement

For all the tests, three cutting force components, i.e., principal forces, thrust forces, and transverse forces, were measured with a Kistler 9257A three-axis piezoelectric force dynamometer mounted on the traversing carriage of the lathe and a data acquisition system based on a simple Labview program. Figure 3.3 shows the data acquisition equipment used in the tests. For each of the force components, a proportional electrical charge is obtained from the dynamometer and then directed into a 3-channel Kistler charge amplifier assembly type 5801 where they are converted into proportional voltages for record, display and further analysis. The charge amplifier range was set for 50 for all three units which means that the output of all three amplifiers is 50 Newtons per volt. For calibration, a series of known weights were placed on the dynamometer along the x, y, and z directions. An output of 50 Newtons per volt should be acquired and if not, the transducer sensitivity setting on the charge amplifier was adjusted so that the 50 Newtons per volt output was achieved. Final charge amplifier transducer sensitivity settings were set at 7.84, 7.9 and 3.74 pC/lb for channels x, y, and z, respectively. Note that the calibration only applies to the applied known force level, and a known calibration force that more closely approximated the forces produced during practical turning tests was applied to get a more accurate calibration. Also note that the actual cutting forces were measured at a location off the center axes of the dynamometer while calibration was measured at the center axes of the dynamometer. The dynamometer is designed to minimize this effect and the difference between the forces measured at those two locations is less than 1%. Transverse force should be nearly zero, which will validate the orthogonality assumption. The measured in-plane cutting forces were used to validate the FEM results.

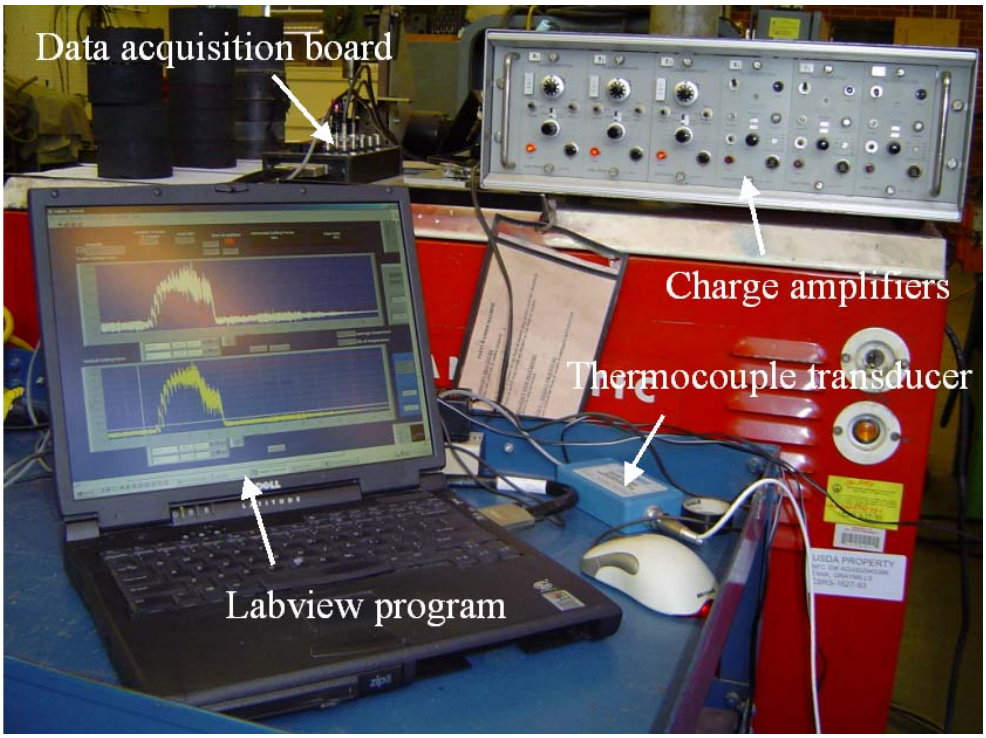

Figure 3.3. Data acquisition equipment.

3.2.3. Workpiece Surface Temperature Measurement

Elastomers are temperature-sensitive materials. Their mechanical properties change significantly even when the temperature only varies slightly (Ward, 1983), (Bhowmick and Stephens, 2001), (Gent, 2001). There are two heat sources during elastomers machining processes, i.e. heat created by friction at the workpiece/tool interface and by elastomers' hysteresis phenomenon under cyclical loading. The latter normally can be neglected in turning because the turning process itself does not involve cyclical loading. Heat generated due to friction in machining can be significant, especially when the machining speed is high and the interfacial friction force is large. Actually, in some preliminary high speed milling tests, smoke

and melting of the workpiece were observed during machining, which indicates that excessive heat is generated in the machining process.

A real time non-contact temperature measurement method is essential to achieve accurate temperature measurements for the moving workpiece during machining. Emissivity (0 ~ 1.0) is a surface property which determines how well an object's temperature can be measured using an infrared device. The higher the emissivity, the more accurate the infrared temperature measurement. Rubber has an emissivity of 0.9 compared to 0.10 ~ 0.12 for polished mild steel, therefore rubber is a good emitter for which infrared temperature measurement technology is well suited to apply for temperature measurements (Handheld Infrared Thermocouple Operator's Manual, Omega Engineering, Inc.). In this study, an Omega infrared thermal probe type OS-88000-K-1200 was used to measure the machined workpiece surface temperature during machining. The probe has a response time 80 ms and measurement range from -50°C to 650°C (–60°F ~ 1200°F) that is independent of emissivity over the range 0.8 to 1.0. The infrared thermal probe was pre-calibrated by the manufacturer and has an error less than 0.5% within the measurement range.

3.2.4. Machined Surface Roughness Measurement

The machined surface is an important measure of a machining operation because it represents the end-goal of the operation. Surface integrity is a term that involves several considerations: surface finish and freedom from cracks, chemical change, thermal damage (burn, transformation, and overtempering), and adverse (tensile) residual stress. Surface finish is by

far the most important consideration for machining operations (Shaw, 2005). Lewis et al. (Lewis, 2002), (Shih, Lewis and Strenkowski, 2004) attempted to categorize the end-milled surface finish as four levels by observations and descriptions. Rodkwan tried to characterize the turned surface at three levels, i.e. rough, smooth and intermediate (Rodkwan, 2002). In this study, the machined surface finish was evaluated by direct measurement of the surface profile for rubber. Recall that rubber has a very small modulus, and any contact measurement method, such as a stylus tracer, will deform the workpiece surface and significantly affect the measurement accuracy. Therefore, a non-contacting reflective laser profilmeter was used for the surface finish measurement as shown in Fig. 3.4. The laser displacement sensor scans the machined surface along a programmed circular path. The reflected laser signal is captured to determine the surface profile. The measured signal includes both surface waviness and roughness information as shown in Fig. 3.5. A frequency filter was used to filter out the low frequency waviness signal and retain the surface roughness signal for analysis. The surface roughness, calculated by the root mean square value $RMS = \sqrt{\frac{\sum_{i=1}^{N} X_i^2}{N-1}}$, was used to evaluate the surface quality (Shaw, 2005).

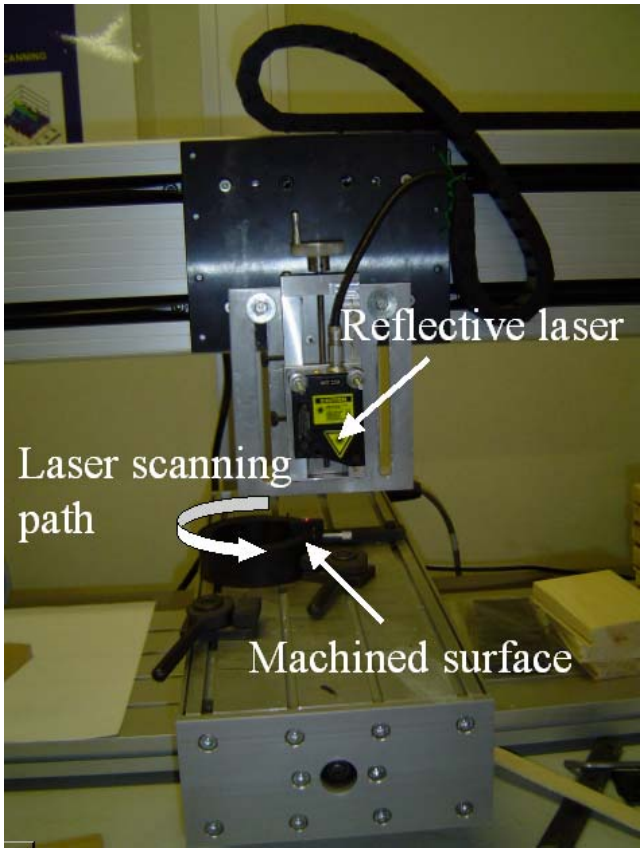

Figure 3.4. Surface roughness measurement.

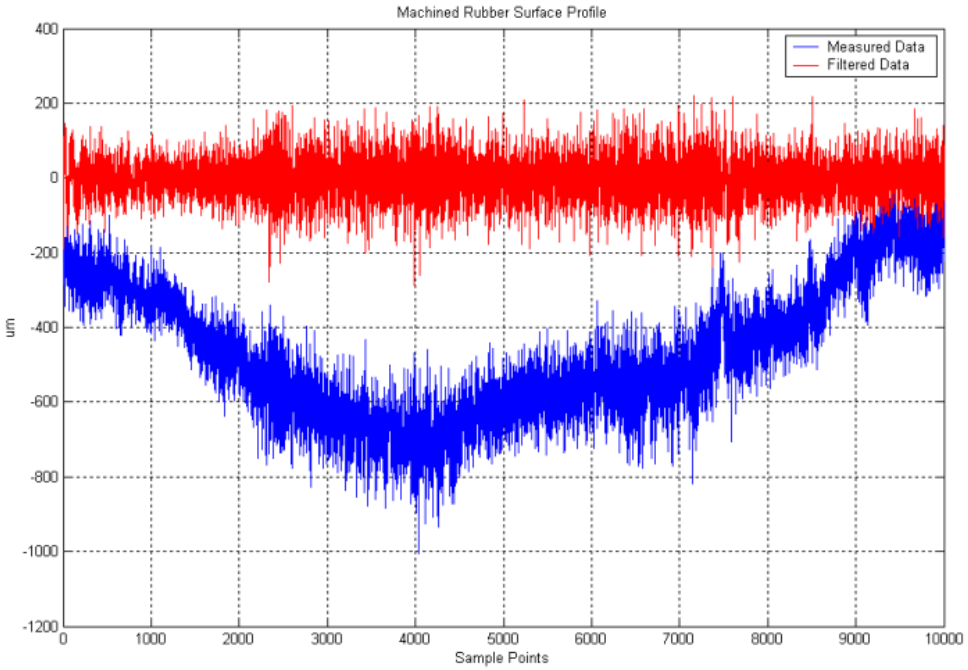

Figure 3.5. Machined rubber surface profile signals before and after filtering for cutting with a 50° rake angle and 5° clearance angle tool for 550 rpm spindle speed and 0.005 in/rev feed rate.

3.2.5. Tool Tip Radius Measurement

The sharpness of the tool cutting edges was assumed unchanged during the tests due to the short time for the tests and extremely low modulus for the rubber material. The nose width of the cutting edge was measured after the tests using an optical microscope measurement system as shown in Fig. 3.6. Using the assumption of a circular tool nose, the radius of the tool was calculated according to the schematic diagram in Fig. 3.7 and Eq. 3.1.

$$\text{Tool tip radius (length of BC or CD)} = \frac{BD/2}{\cos(A/2)} \qquad 3.1$$

In this equation, BD is the measured nose width of the tool and A is the included angle of the tool tip and equals to 90°- (rake angle + clearance angle). The range of various cutting tool tip

radii is between 6 and 10 µm. An average tool tip radius of 8 µm was calculated and adapted in the FE models.

Fig. 3.6. Apparatus for measuring the cutting edge sharpness.

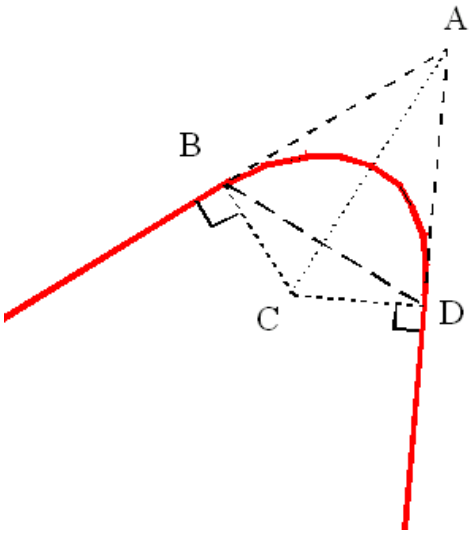

Fig. 3.7. Schematic diagram to determine the tool tip radius. (Hsieh, 1998).

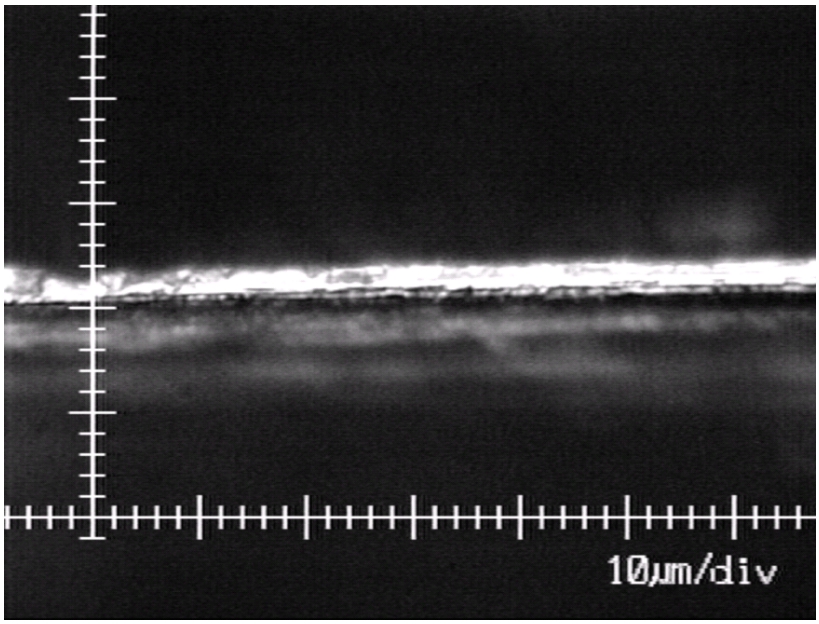

Fig. 3.8. Cutting tool edge with a tool of 40° rake angle and 5° clearance angle.

3.3. Experiment Results and Discussion

3.3.1. Cutting Forces

The rake angle is the most important geometric parameter for cutting tools, and its value affects the tool performance dramatically. Figures 3.9 and 3.10 show the measured principal and thrust force components as a function of rake angle for various orthogonal cutting conditions. It can be clearly seen that those force components are decreasing with rake angle for similar cutting conditions, which is expected. Also note that the forces converge to a narrow range as the rake angle increases for various cutting conditions. Figures 3.11 and 3.12 show that the principal and thrust force components vary with clearance angle, respectively. Again, the components

decrease with increasing clearance angles. The cutting speed and feed rate have a minor effect on cutting forces, although it can be observed that a larger feed rate corresponds to larger cutting forces.

As shown in Fig. 3.13, larger principal forces are produced during cryogenic cutting. The increases of principal cutting forces become more significant with higher cutting speeds for cryogenic cutting. This is due to a larger modulus of rubber at lower temperatures. In contrast, decreasing vertical forces were observed when cryogenically cutting rubber. This is because the increased rigidity of rubber at lower temperatures leads to less workpiece material flow underneath the tool clearance surface. In contrast, under ambient temperatures rubber is more flexible and easier to flow beneath the tool during cutting, which would apply a larger force on the tool clearance surface in the positive vertical direction. Lower vertical forces are beneficial in maintaining cutting stability and achieving a good machined surface finish because the tool usually has a small included angle which results in a low tool rigidity.

Figure 3.14 shows the principal forces for 10° and 50° rake angle tools for a 550 rpm spindle speed and a 0.254 mm/rev feed at room temperature. Fluctuation of the measured forces occurs as a result of the accumulation and release process of rubber internal energy during cutting. This process will be discussed in chapter 4 in detail (see Figs. 4.15 ~ 4.17). It can be seen that more fluctuation of the measured forces occurs for a 10° rake angle tool. In contrast, a cutting tool with a 50° rake angle produced less force fluctuation.

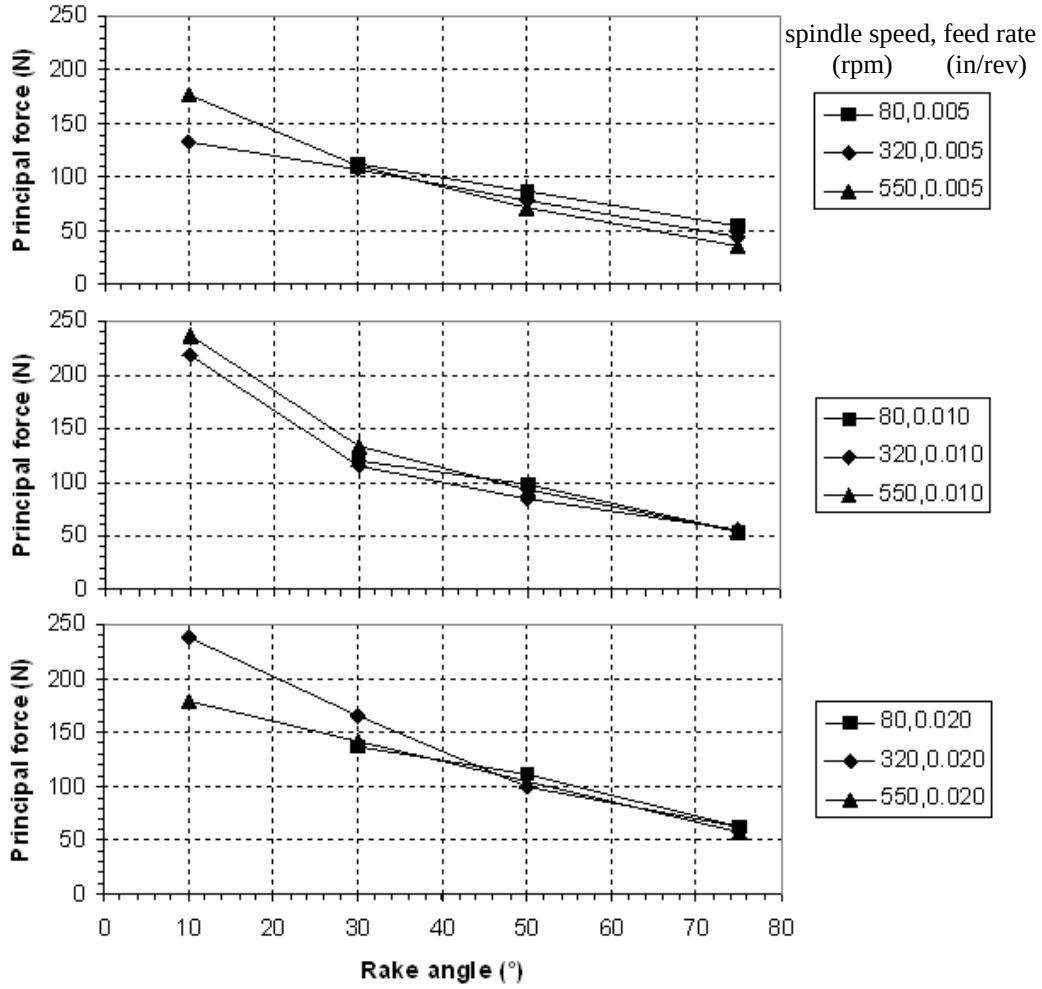

Figure 3.9. Principal forces as a function of rake angle for various cutting conditions.

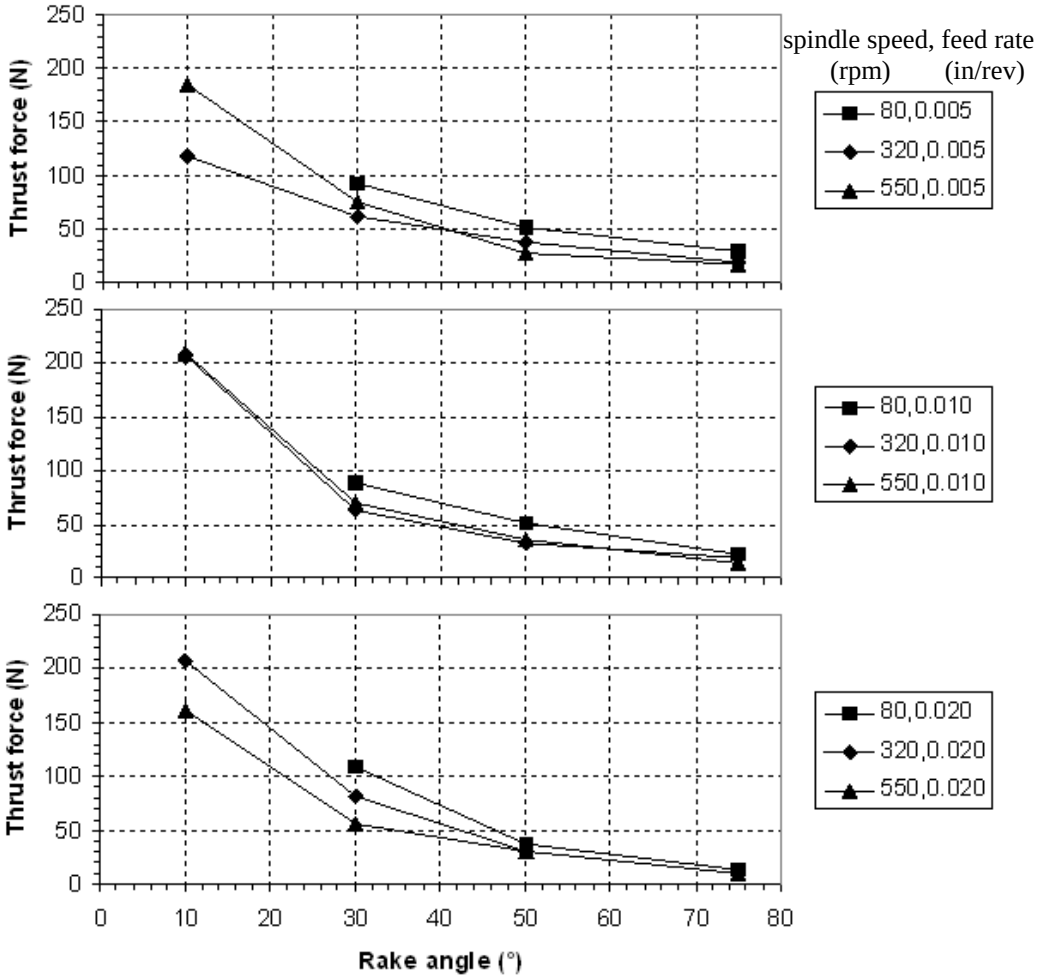

Figure 3.10. Thrust forces as a function of rake angle for various cutting conditions.

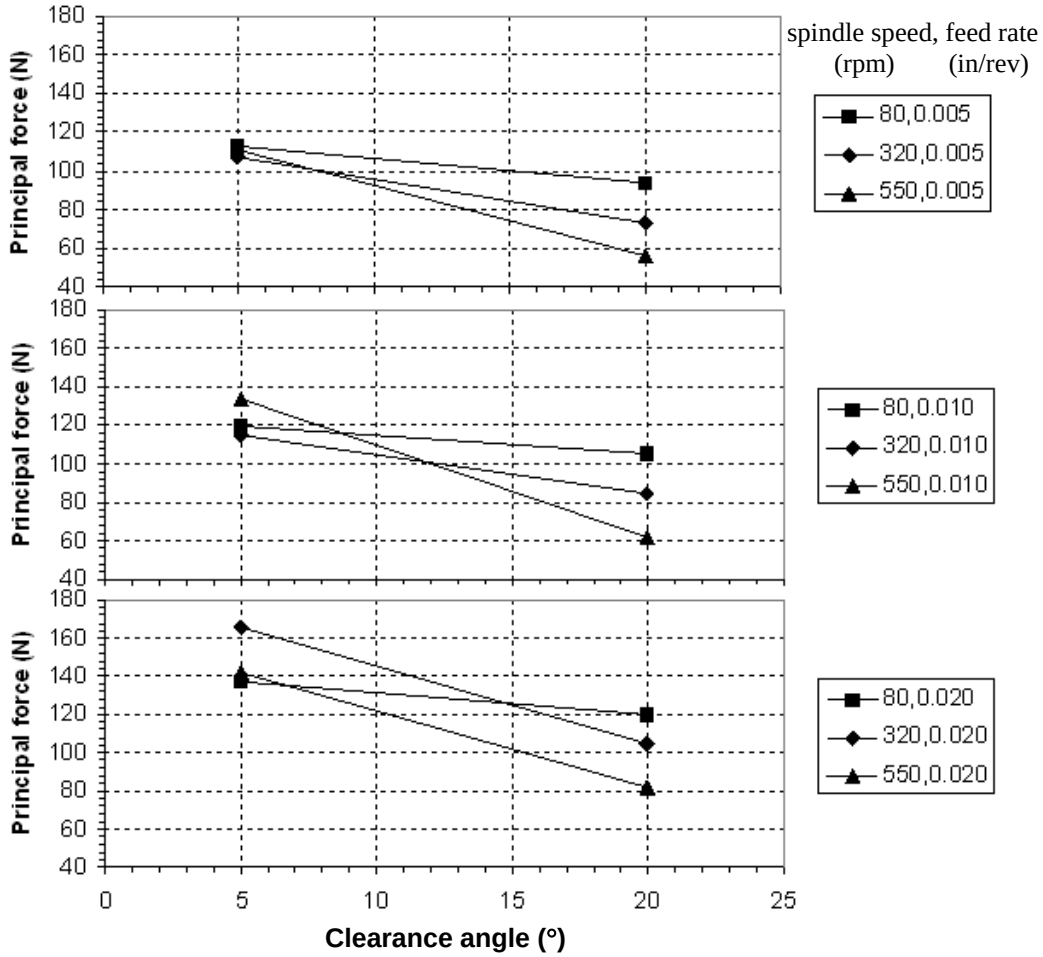

Figure 3.11. Principal forces as a function of clearance angle for various cutting conditions.

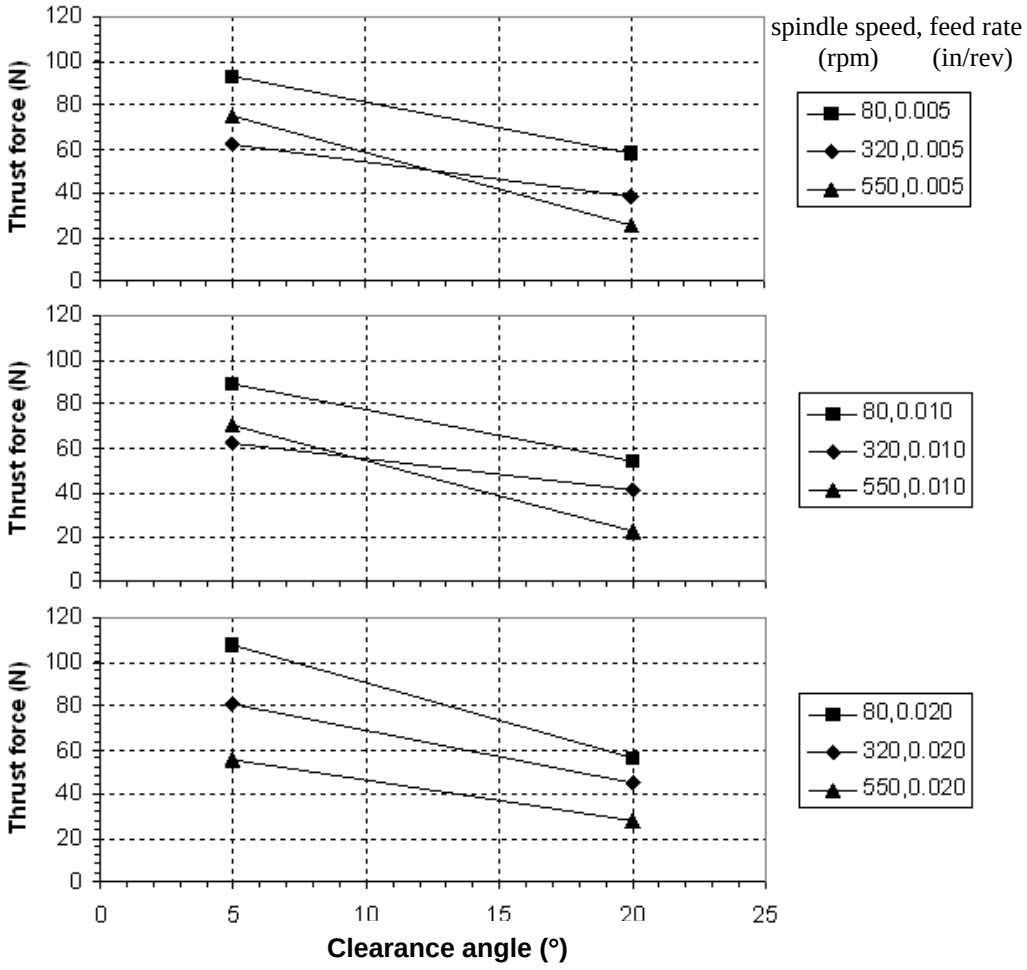

Figure 3.12. Thrust forces as a function of clearance angle for various cutting conditions.

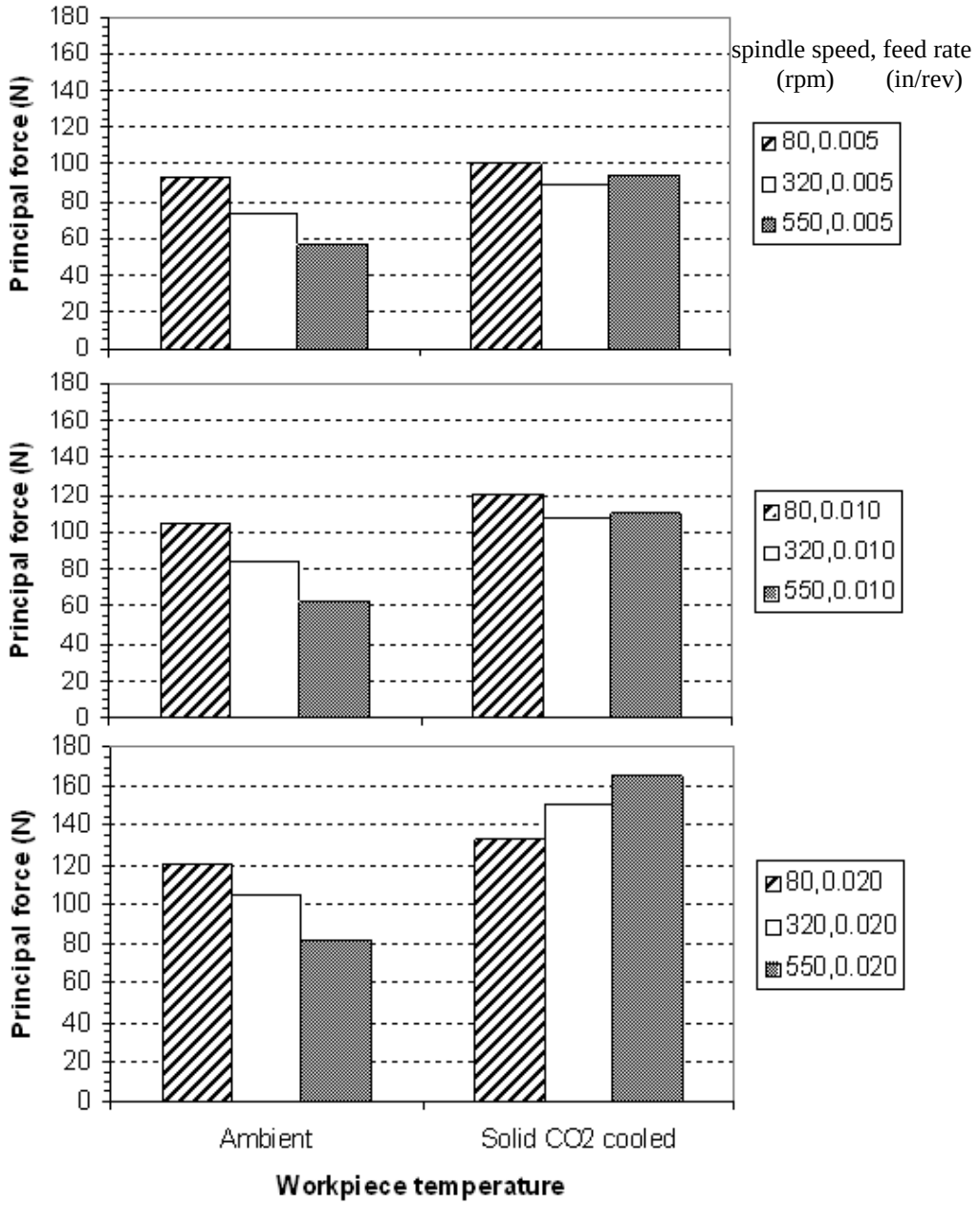

Figure 3.13. Principal forces as a function of workpiece temperature for various cutting conditions.

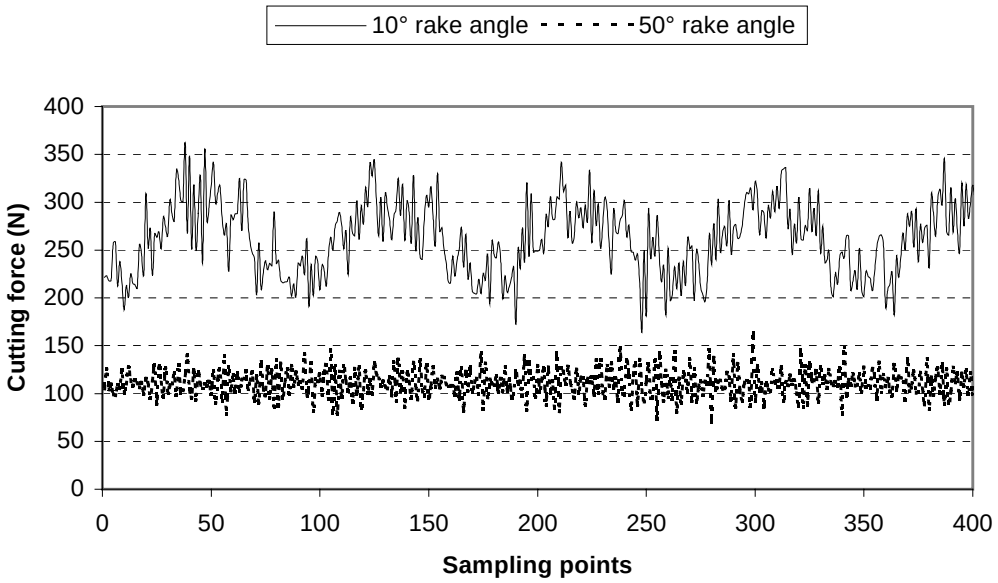

Fig. 3.14. Measured cutting forces with 10° and 50° rake angle tools.

3.3.2. Machined Surface Finish

A non-contacting reflective laser profilmeter (type MICROTRAK 7000) was applied for measuring the surface finish. Figure 3.15 shows RMS values of the machined surface with rake angles for tools with a clearance angle of 5° under various cutting conditions. It can be seen that rake angle has the most significant effect on machined surface quality. For example, for cutting with a 550 rpm spindle speed and 0.005 in/rev feed rate, the 30°, 50° and 75° rake angle tools generate a surface roughness of 116, 81, 49 μm, respectively. The surface quality improves significantly as the rake angle increases. Figure 3.16 gives the actual surface profile signals from various surface measurements. It is apparent that larger rake angles produce a better surface finish.

The cutting speed and feed rates do not have a significant effect on surface quality. However, there was a larger surface finish discrepancy for different cutting speeds with tools with small rake angles as compared with tools with larger rake angles. For example as shown in Fig. 3.15, for all cutting tests with a tool of 30° rake angle, the surface roughness varies over a range of 30 μm. For cuts with a 75° rake angle tool, the variation has a range of 15 μm only. A larger rake angle tool not only produces a smoother surface but also generates a smaller surface roughness variation. No direct relationships were found between the clearance angle and surface finish.

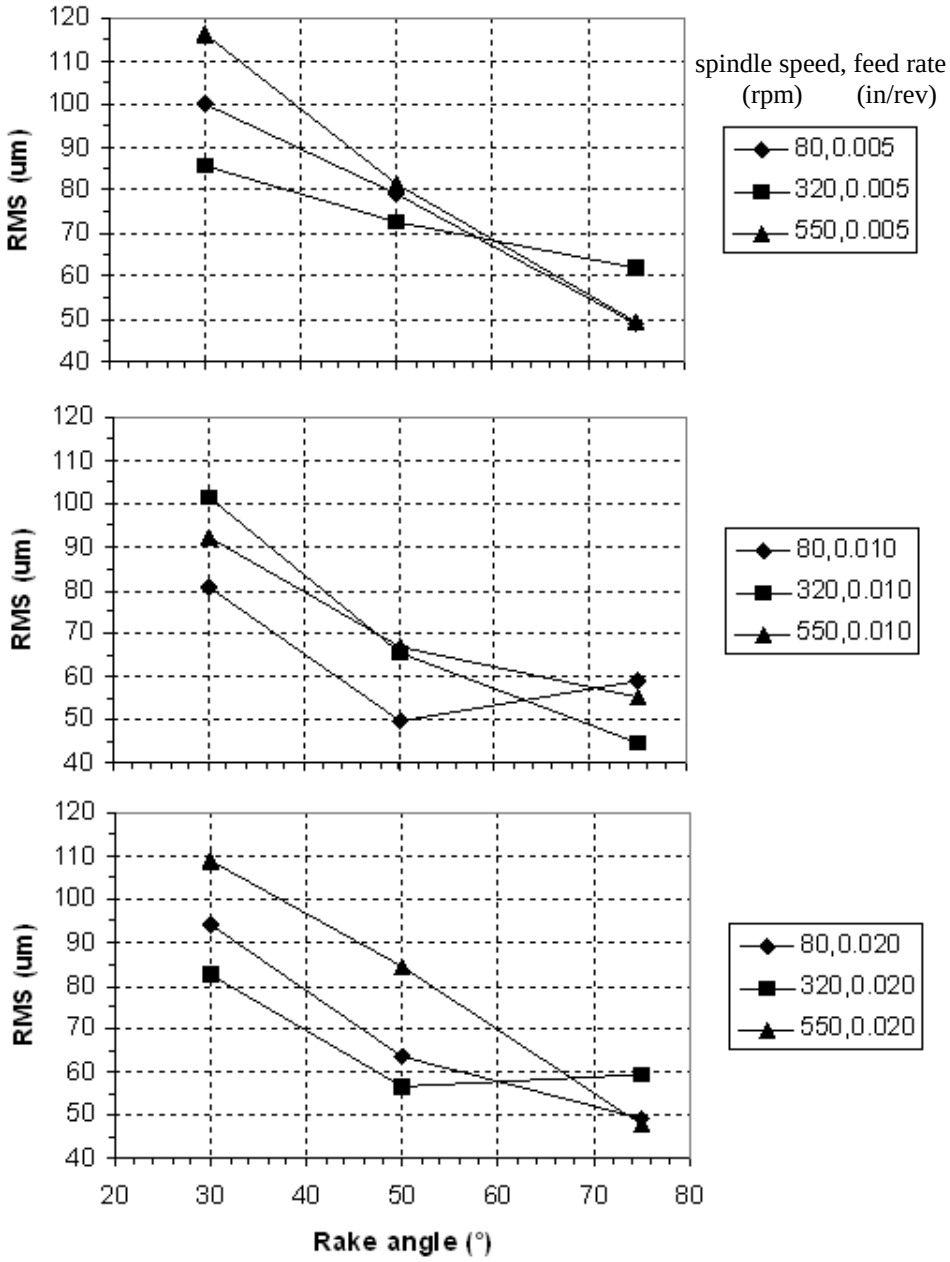

Fig. 3.15. Machined surface roughness with rake angle for a tool with a clearance angle of 5°.

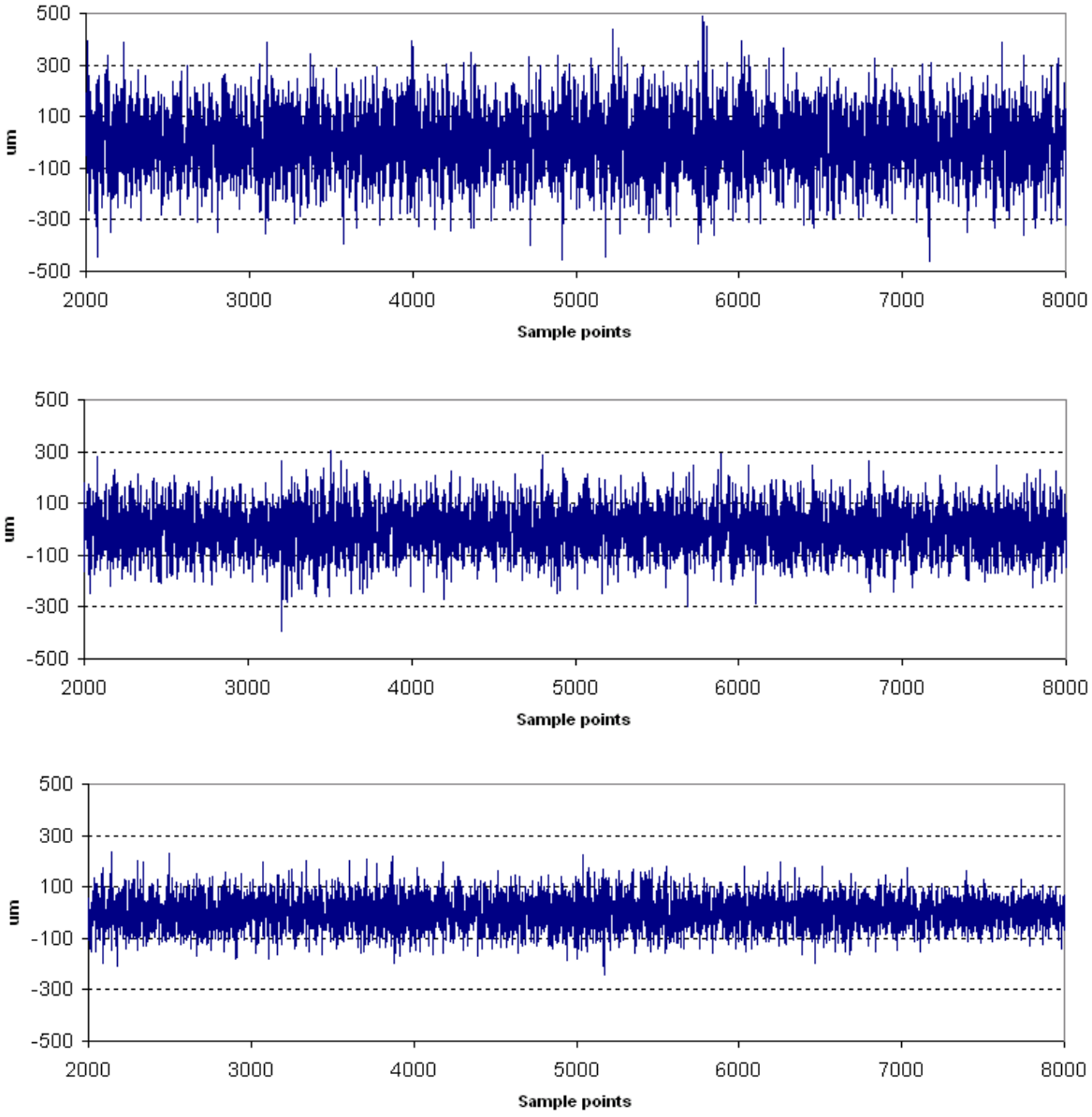

Fig. 3.16. Machined surface profiles (μm) for cutting tests with various cutting tools (Upper: 30° rake angle and 5° clearance angle, Middle: 50° rake angle and 5° clearance angle, Lower: 75° rake angle and 5° clearance angle) at a spindle speed of 550 rpm and feed rate of 0.005 in/rev.

The low rigidity of rubber is believed to contribute to the rough machined surface. As shown in Figure 3.17, the rigidity of rubber increases as the workpiece temperature decreases. Also note that a sudden increase of the rubber modulus occurs near the glass transition temperature (about -70°C). This is the reason that cryogenic machining tests were carried out to study the relationship between the machined surface finish and workpiece temperature. For the cryogenic cutting tests, rubber samples were kept in a cooler with solid carbon dioxide (sublime temperature -68°C) overnight to ensure that the workpiece had a low temperature. During the tests, the workpiece was quickly removed from the cooler and set up on the lathe. The entire set-up was completed in less than 30 seconds. The workpiece temperature was well maintained between -40°C ~ -25°C during the tests due to rubber's low thermal conductivity. The surface roughness and actual machined surface photograph with workpiece temperatures are shown in Figures 3.18 and 3.19 respectively. It can be seen that the machined surface quality was greatly improved for all speeds and feed rates by machining solid carbon dioxide cooled rubber as compared with the machining of rubber under ambient temperature conditions.

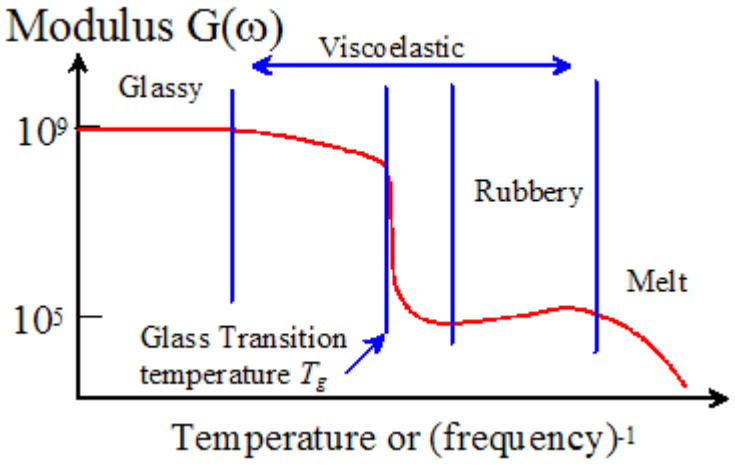

Fig. 3.17. Rubber rigidity with temperature.

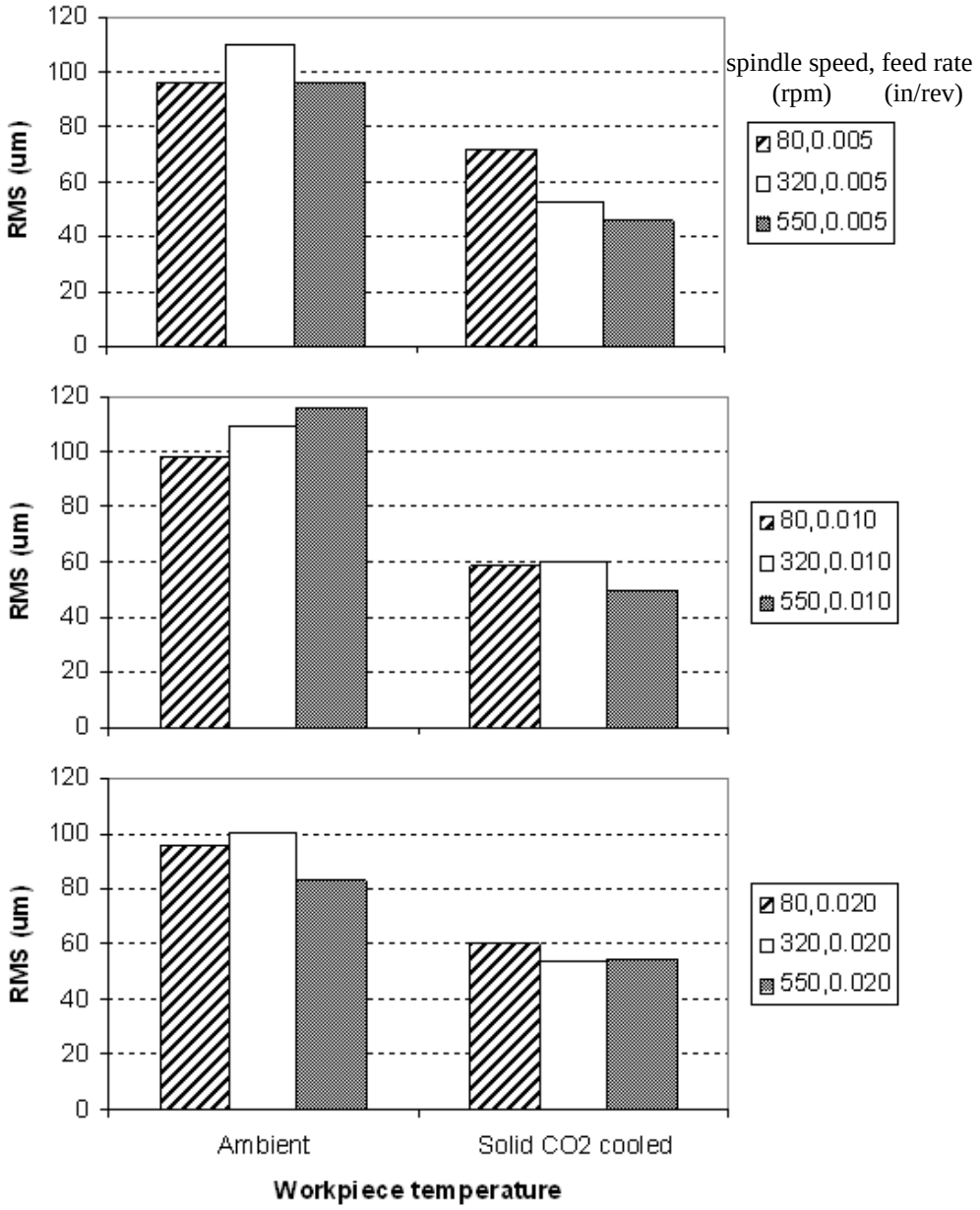

Fig. 3.18. Machined surface roughness with workpiece temperature for tools with 30° rake angle and 20° clearance angle.

Fig. 3.19. Photos of machined surface roughness with workpiece temperature.

3.3.3. Workpiece Machined Surface Temperature

Rubber has a low melting temperature, heat capacity and thermal conductivity (Table 4.1). Therefore, the heat generated during machining can deteriorate the mechanical properties and dramatically affect the machining process. There are two heat sources that occur when machining rubber. One is the heat generated by friction between the rake surface and workpiece, and the other is due to internal heating from hystersis of the rubber under cyclic loading. Figure 3.20 shows a typical temperature curve during the tests. A total of five segments can be identified for changing of the workpiece surface temperature in cutting processes. The workpiece has an ambient temperature for the first 2.8 s as the tool approaches the workpiece prior to contacting it. Next, surface rubbing occurs as the tool begins to contact

the workpiece. Note that during rubbing, cutting does not occur and no chips are produced. Also note that the rate of temperature rise is fairly large due to the high friction force that occurs on the workpiece-rake interface. After a short rubbing period of about 0.3 s, the cutting process occurs in which the workpiece surface temperature maintains a constant value. This indicates that the heat generation during cutting is insignificant. The transverse carriage of the lathe is stopped at about 5 s, and another rubbing process is initiated. The workpiece temperature arises again with a rate close to that during the first rubbing process. The carriage is finally withdrawn from contact with the workpiece at about 5.7 s, during which a steep drop in the workpiece temperature is observed due to the separation of the tool from the workpiece and the cooling effect of ambient air circulation.

Table 3.1. Material properties for test rubber samples.

Density (Kg/m^3)	Thermal Expansion Coeff. (1/K)	Thermal Conductivity (W/m K)
1104.43	4.8E-4	0.145

Specific Heat (J/Kg K)	Failure Stress (MPa)	Failure Strain (%)
1500	11.0	500

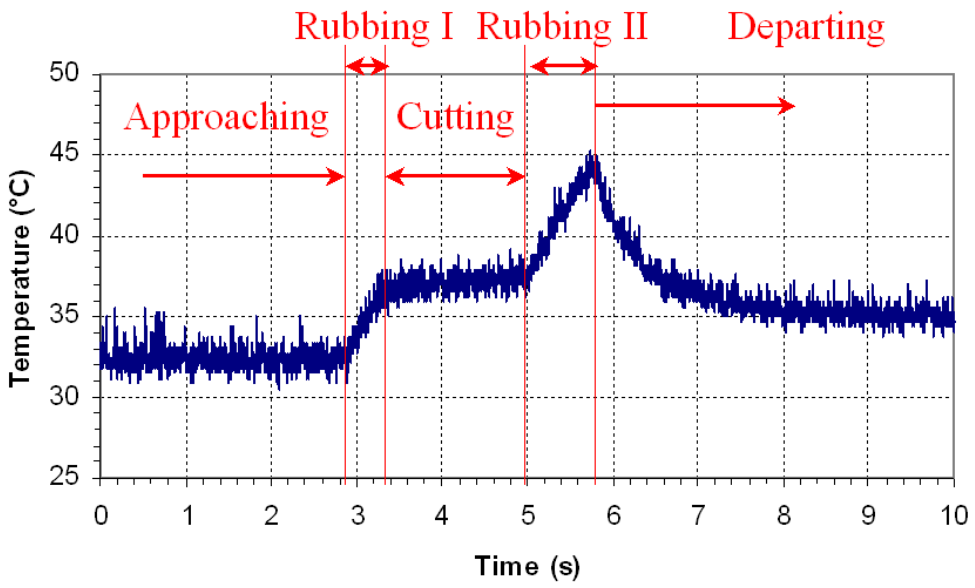

Fig. 3.20. Typical work surface temperature profile during a test with a tool of 30° rake and 20° clearance for a spindle speed of 550 rpm and a feed rate of 0.020 in/rev under ambient temperature conditions.

Note that the ultimate temperature was not high enough to melt the workpiece in the turning tests because of the short test times and the relatively low cutting speeds. However, it can be seen that the high rate of temperature rise in the rubbing phase would lead to a very high temperature of the workpiece if the duration of the tests was longer. This would occur for example when removing a large amount of material from the workpiece with a small feed rate. In fact, melting of the workpiece was observed in some preliminary high speed milling tests in which the feed rates were fairly low.

The machined rubber surface temperature depends on two factors, the slope of the temperature rise and the duration of the rubbing process. Figures 3.21 and 3.22 show the temperature rise rate with the rake angle for various feed rates and the rubbing process duration with feed rate

for various tool geometries, respectively. It can be seen that a tool with a large rake angle produces a low temperature rise rate, and large feed rates reduce the rubbing duration. Therefore, the combination of a large rake angle tool and a large feed rate are important to keep the machined surface temperature low.

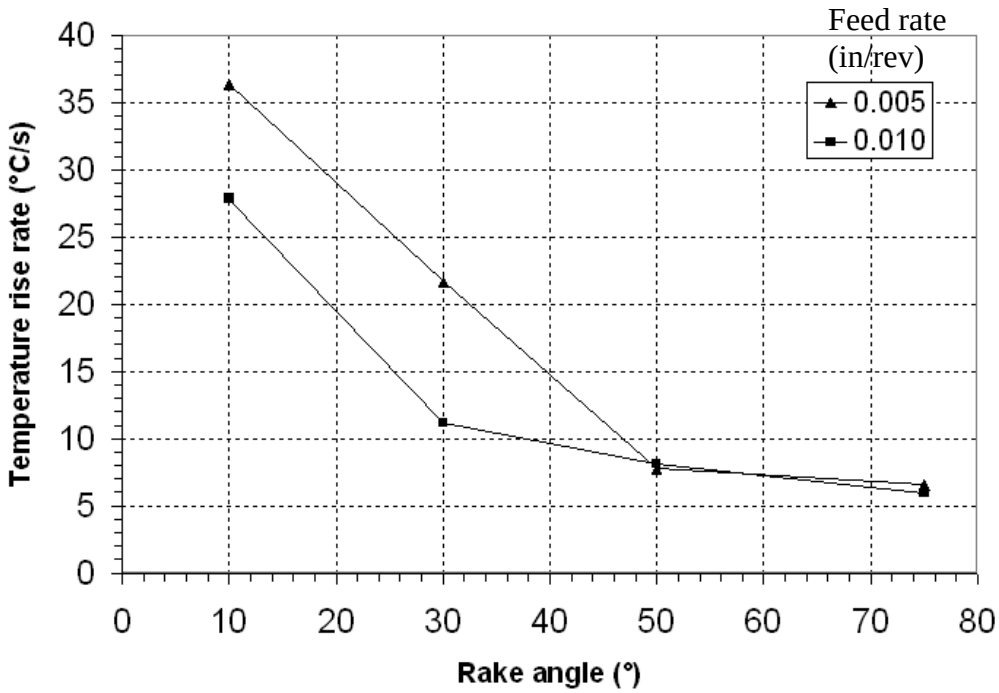

Fig. 3.21. Temperature rise rate with rake angle for various feed rates.

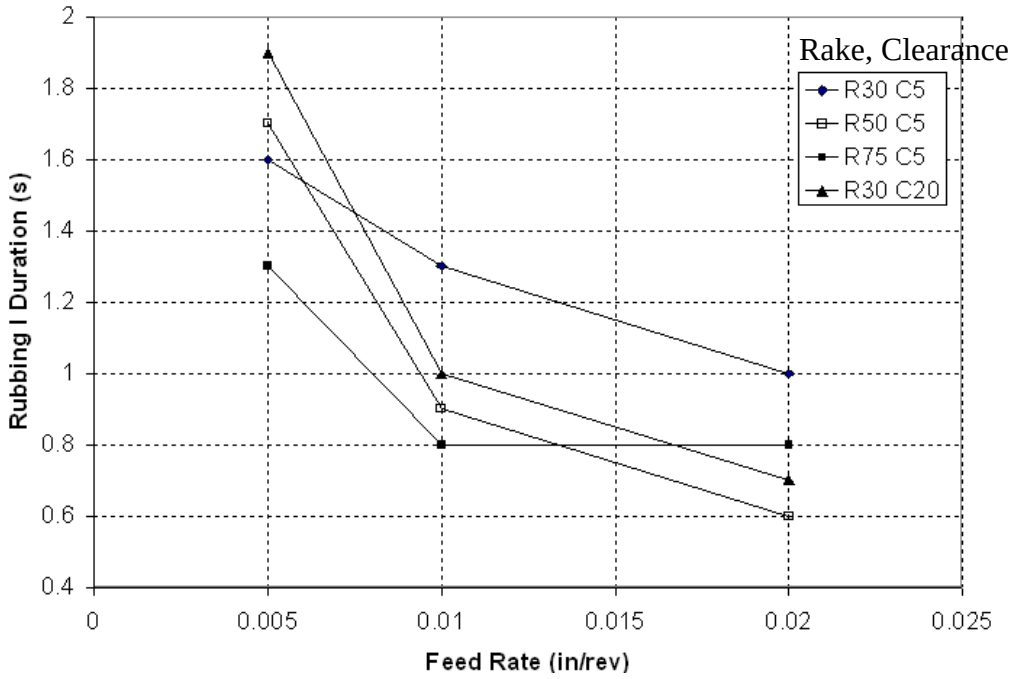

Fig. 3.22. Rubbing process duration with feed rate for various tool geometries.

3.3.4. Chip Morphology

Chip shape and form provide useful information for understanding the chip formation process of rubber machining. Chips were collected and analyzed after the cutting tests. Figure 3.23 shows various chip types that correspond to the machined surfaces shown in Fig. 3.19. It can be seen that the chip types are closely related to the machined surface finishes. From previous and current cutting tests, it has been shown that the morphology of rubber chips can be categorized into three basic types: (1) continuous ribbon-like chips with a smooth machined surface, (2) segmented chips with a rough machined surface, and (3) discontinuous chips with an even worse surface finish. Continuous ribbon-like chips are associated with a smooth surface finish, which occurs with large rake angle tools and under dry-ice cooled workpiece

conditions. In contrast, discontinuous chips are associated with a rough machined surface that results from cutting with small rake angle tools at ambient temperatures.

Fig. 3.23. Photos of chips with workpiece temperature and cutting conditions.

3.4. Concluding Remarks

The rake angle of the tool plays an important role in generating a smooth machined surface. Tools with a large rake angle produce a smooth surface with ribbon-like chips. Conversely, rough surfaces and discontinuous chips are generated with tools with a small rake angle. Corresponding cutting force components decrease as the rake angle increases. The temperature rise rate for cutting with a large rake angle tool is low compared with that for a small rake angle tool. Low workpiece temperatures help to generate smooth machined surfaces because of the

increased rigidity of rubber with lower temperature. Cryogenic machining is also useful for achieving a smooth machined surface. It can be used to keep the temperature of the rubber workpiece from reaching critical values, such as the melting point, due to the excessive heat generated during the machining processes. The temperature can be further reduced by shortening the duration of the rubbing phase. Large feed rates will result in shorter rubbing duration and a reduced machined surface temperature rise rate, which will lead to a controlled machined surface temperature and an improved machined surface finish. Finally, it was found that the cutting process itself does not change the machined surface temperature significantly.

4. SIMULATIONS OF ORTHOGONAL RUBBER CUTTING

Based on the discussions in the previous chapters, the basic finite element (FE) simulation methodology for 2D plane strain analysis of cutting appears to be in a relatively advanced stage of development. The most recent work of Strenkowski et al includes updated-Lagrangian, Eulerian as well as a coupled Lagrangian-Eulerian formulation (Strenkowski, et al., 1985, 1986, 1987, 1990). In contrast, three-dimensional finite element analysis has not drawn as much attention as the 2D finite element modelling from researchers. Strenkowski et al developed an analytical finite element model for predicting three-dimensional tool faces and chip flow angle in a drilling process. The approach consists of coupling an orthogonal finite element cutting model with an analytical model of three-dimensional cutting (Strenkowski, et al., 2002). Guo and Liu & Guo and Dornfeld have reported the use of 3D finite element models to analyze turning and drilling processes (Guo, et al., 1999, 2000, 2002). With the ever-increasing computational power of super computers, the development of 3D simulation methodology for cutting is a potential area for future research.

In this dissertation, a 2D explicit plane strain FE model using ABAQUS/Explicit was developed to analyze rubber cutting using high-speed steel (HSS) tools. A brief background of the finite element method and ABAQUS/Explicit code for simulating cutting processes is described first in the following sections. The neo-Hookean constitutive model for a hyperelastic material considering the effective stress failure criterion was used in the simulations. In this chapter, the advantages of applying an explicit method for simulating the rubber cutting process over its implicit counterpart are discussed. The model is used to

predict cutting forces, chip shape, stress and strain fields, and the strain energy distribution in the chip and workpiece. The orthogonal cutting experiments discussed in Chapter 3 are used to validate the FE models. Good agreement was found between the predicted and measured cutting forces. Favorable cutting conditions for the formation of a smooth machined surface are identified in both the simulations and experiments. The finite element model provides new insight into the chip formation process of rubber cutting.

4.1. General Description of the Finite Element Method

The finite element method (FEM) is used in many problems to find an approximate solution for the displacements, deformations, stresses, forces, and possibly other state variables such as the temperature in a solid body that is subjected to a history of "loading". The exact solution of such a problem requires that both force and moment equilibrium be maintained at all times over an arbitrary volume of the body. The displacement finite element method is based on approximating this equilibrium requirement by replacing it with a weaker requirement, that equilibrium must be maintained in an average sense over a finite number of divisions of the volume of the body. In this section the exact equilibrium statement will be developed and written in the form of a virtual work statement and then the approximate form of equilibrium used in a finite element model will be derived (ABAQUS Theory Manual, 2002).

Let V denote a volume occupied by a part of the body in the current configuration, and let S be the surface bounding this volume. Again, it should be emphasized that from a Lagrangian

point of view, the volume being considered is a volume of material in the body. Specifically, V is the volume of space occupied by this material at the "current" point in time, which is distinct from the Eulerian approach, where material flowing through that volume is examined. Let the surface traction at any point on S be the force t per unit of current area, and let the body force at any point within the volume of material under consideration be f per unit of current volume. Force equilibrium for the volume then can be written as

$$\int_S t dS + \int_V f dV = 0 \qquad 4.1$$

The "true" or Cauchy stress matrix σ at a point of S is defined by

$$t = n \cdot \sigma \qquad 4.2$$

where n is the unit outward normal to S at the point. Using this definition, equation 4.1 becomes

$$\int_S (n \cdot \sigma) dS + \int_V f dV = 0 \qquad 4.3$$

Gauss's theorem allows us to rewrite a surface integral as a volume integral according to

$$\int_S n \cdot () dS = \int_V (\frac{\partial}{\partial X}) \cdot () dV \qquad 4.4$$

where () is any continuous function, which can be a scalar, vector or tensor.

Applying Gauss's theorem to the surface integral in the equilibrium equation gives

$$\int_S n \cdot (\sigma) dS = \int_V (\frac{\partial}{\partial X}) \cdot (\sigma) dV \qquad 4.5$$

Since the volume is arbitrary, this equation must apply pointwise in the body, thus providing the differential equation of translational equilibrium:

$$\frac{\partial}{\partial X} \cdot \sigma + f = 0 \qquad 4.6$$

These are the three familiar differential equations of force equilibrium. In these derivations, no approximations have been made with respect to the magnitude of the deformation or rotation. The equations are an exact statement of equilibrium as long as the surface tractions, body forces, stress (Cauchy stress, defined by equation 4.2), volume, and area are precisely defined.

Moment equilibrium is most simply written in the general case by taking moments about the origin:

$$\int_S (X \times t) dS + \int_V (X \times f) dV = 0 \qquad 4.7$$

Use of Gauss's theorem with this equation then leads to the result that the "true" (Cauchy) stress matrix must be symmetric:

$$\sigma = \sigma^T \qquad 4.8$$

so that at each point there are only six independent components of the stress tensor. Conversely, by taking the stress matrix to be symmetric, moment equilibrium is automatically satisfied. Therefore, only translational equilibrium be considered when explicitly writing the equilibrium equations. The moment equilibrium equation written above assumes that there are no point couples acting on the volume. If there are, the stress matrix does not have the symmetry property of equation 4.8.

The basis for the development of a displacement-interpolation finite element model is the introduction of a locally-based spatial approximation for parts of the solution. To develop such an approximation, the three equilibrium equations represented by equation 4.6 are replaced by an equivalent "weak form". The weak form is a single scalar equation over the entire body, which is obtained by multiplying the pointwise differential equations by an arbitrary, vector-valued "test function" defined with suitable continuity over the entire

volume, and then integrating. As the test function is arbitrary, the differential equilibrium statement in any particular direction at any particular point can always be recovered by choosing the test function to be nonzero only in that direction at that point. For this case of equilibrium with a general stress matrix, this equivalent "weak form" is the virtual work principle. The test function can be a "virtual" velocity field, δv, which is completely arbitrary except that it must obey any prescribed kinematical constraints and have sufficient continuity. The dot product of this test function with the equilibrium force field then represents the "virtual" work rate.

Taking the dot product of equation 4.6 with δv results in a single scalar equation at each material point that is then integrated over the entire body to give

$$\int_V (\frac{\partial}{\partial X} \cdot \sigma + f) \cdot \delta v dV = 0 \qquad 4.9$$

The chain rule gives

$$(\frac{\partial}{\partial X}) \cdot (\sigma \cdot \delta v) = \left[(\frac{\partial}{\partial X}) \cdot \sigma \right] \cdot \delta v + \sigma : \left[(\frac{\partial}{\partial X}) \cdot \delta v \right] \qquad 4.10$$

so that

$$\int_V \left[\left(\frac{\partial}{\partial X} \right) \cdot \sigma \right] \cdot \delta v dV = \int_V \left[\left(\frac{\partial}{\partial X} \right) \cdot (\sigma \cdot \delta v) - \sigma : \left(\frac{\partial \delta v}{\partial X} \right) \right] dV \qquad 4.11$$

Applying Gauss theorem to the first term gives $= \int_S n \cdot \sigma \cdot \delta v dS - \int_V \sigma : \left(\frac{\partial \delta v}{\partial X} \right) dV$

Applying the definition of the Cauchy stress to the first term gives

$$= \int_S t \cdot \delta v dS - \int_V \sigma : \left(\frac{\partial \delta v}{\partial X} \right) dV$$

Thus, the virtual work statement, equation 4.9, can be written as

$$\int_S t \cdot \delta v dS + \int_V f \cdot \delta v dV = \int_V \sigma : \left(\frac{\partial \delta v}{\partial X} \right) dV \qquad 4.12$$

The virtual work statement has a simple physical interpretation that the rate of work done by the external forces subjected to any virtual velocity field is equal to the rate of work done by the equilibrating stresses on the rate of deformation of the same virtual velocity field. The principle of virtual work is the "weak form" of the equilibrium equations and is used as the basic equilibrium statement for the finite element formulation. Its advantage in this regard is that it is a statement of equilibrium cast in the form of an integral over the volume of the body. Approximations can be introduced by choosing test functions for the virtual velocity field that are not entirely arbitrary, but whose variation is restricted to a finite number of nodal values. This approach provides a stronger mathematical basis for studying the approximation than the alternative of direct discretization of the derivative in the differential equation of equilibrium at a point, which is used in a finite difference approach for solving the same problem (ABAQUS Theory Manual).

There are two further steps to derive the finite element equations. These include discretizing the geometry and approximating the displacement field. Geometry discretization converts the continuum into a mesh structure that consists of nodes and elements. Therefore, the smooth integration over the continuum is replaced by calculations which are summed over many small elements. Instead of seeking an exact solution in an infinite space, the displacement field is approximated with finite terms and an approximate solution is computed over a finite dimensional space. As long as the mesh is fine enough and the displacement approximation is close enough, a reasonably precise FE solution can be

achieved. Following this procedure, the governing equation of the FEM at time t_n can be written as following (Cook, 1974), (Chandrupatla, and Belegundu, 2002):

$$[M]\{\ddot{u}_n\}+[C]\{\dot{u}_n\}+[K]\{u_n\}=\{F_n\} \qquad 4.13$$

where $[M]$ is the mass matrix

$[C]$ is the damping matrix

$[K]$ is the stiffness matrix

$\{\ddot{u}_n\}$ is the nodal acceleration vector

$\{\dot{u}_n\}$ is the nodal velocity vector

$\{u_n\}$ is the nodal displacement vector

$\{F_n\}$ is the applied load vector

Depending on how the nodal acceleration and nodal velocity vectors are calculated, the above equation can be solved either by an implicit or explicit method. The major difference between the implicit and explicit methods is that the stiffness matrix still exists on the left hand side of the final equation for the implicit method after substituting the nodal acceleration and velocity vectors with the displacement vector. Therefore, a system of simultaneous equations at every time step must be solved. For linear static analysis, the stiffness matrix is constant throughout the loading process. Nevertheless for highly nonlinear analysis such as a cutting process with geometry, material and boundary condition nonlinearities, the stiffness matrix needs to be updated at each time step to simulate the nonlinearities. The unconditional converged implicit method becomes more difficult for these analyses because the stiffness matrix must be inverted and a new set of simultaneous

equations must be solved at each time step. Some iterative techniques such as a Newton-Raphson method are used to solve nonlinear problems which tend to cause convergence problems and require small time steps. Note that the conditional converged explicit method can be used with the use of lumped mass matrix.

In the explicit method, the stiffness matrix is shifted to the right-hand side of the FE equations and therefore, the stiffness matrix need not be inverted for each step. Also since the diagonal mass matrix is used, the FE equations are uncoupled and simultaneous equations need not be solved. Details of the explicit method will be discussed in the next section.

4.2. Explicit Dynamic Analysis

Orthogonal rubber cutting is a complex nonlinear, large deformation process that is coupled with a material failure criterion. It has all three sources of nonlinearities, i.e., material nonliearity (hyperelastic material), nonlinear boundary conditions (contact behavior) and geometric nonlinearity (finite deformation). To address these problems, the explicit dynamic FE code, ABAQUS/Explicit, was used in this research. The advantages of using ABAQUS/Explicit for modelling orthogonal rubber cutting processes are summarized as follows (ABAQUS/Explicit User's Manual, 2002):

1) ABAQUS/Explicit is a well-known nonlinear FEA code that is widely used by academic research units as well as various industries. Its effectiveness in solving nonlinear problems has been proved by many practical examples.

2) ABAQUS/Explicit has an extensive material library that includes many commonly-used material models. Users can also define their own material subroutines once the constitutive laws have been derived.

3) Chip separation is much easier and more flexible to implement using the element deletion option as compared with the implicit counterpart.

4) The solution algorithm is conditionally stable as long as the time increment is less than the critical stability limit. Iteration, assembly and inversion of the stiffness matrix can be avoided by using an explicit integral formulation and lumped mass matrix. Therefore computational cost for each time increment is significantly reduced.

5) The computational cost for each increment is trivial. Because of the implementation of the lumped mass matrix and explicit integral, there is no need to assembly the stiffness and mass matrices, therefore avoiding the solution of large numbers of simultaneous equations.

6) Total costs are comparably small due to the efficiency of each increment even though explicit methods may require a large number of increments. Also explicit methods require much less hard disk space and memory usage than implicit methods for similar simulations.

The explicit dynamics analysis procedure in ABAQUS/Explicit is based upon the implementation of an explicit integration rule together with the use of diagonal or “lumped” element mass matrices. The equations of motion for the body are integrated using the

explicit central difference integration rule (Cook, 1974), (Boast and Coveney, 1999), (Hinton and Owen, 1977)

$$\dot{u}^{(i+\frac{1}{2})} = \dot{u}^{(i-\frac{1}{2})} + \frac{\Delta t^{(i+1)} + \Delta t^{(i)}}{2}\ddot{u}^{(i)} \tag{4.13}$$

$$u^{(i+1)} = u^{(i)} + \Delta t^{(i+1)}\dot{u}^{(i+\frac{1}{2})} \tag{4.14}$$

where $\dot{u}$ is velocity and $\ddot{u}$ is acceleration. The superscript (i) refers to the increment number and i+1/2 and i-1/2 refer to mid-increment values. The central difference integration operator is explicit in that the kinematic state can be advanced using known values of $\dot{u}^{(i-\frac{1}{2})}$ and $\ddot{u}^{(i)}$ from the previous increment. The key to the computational efficiency of the explicit procedure is the use of diagonal element mass matrices because the inversion of the mass matrix that is used in the computation for the accelerations at the beginning of the increment is trivial:

$$\ddot{u}^{(i)} = M^{-1} \cdot (F^{(i)} - I^{(i)}) \tag{4.15}$$

where M is the diagonal lumped mass matrix, F is the applied load vector, and I is the internal force vector. The explicit procedure requires no iterations and no tangent stiffness matrix.

Special treatment of the mean velocities $\dot{u}^{(i+\frac{1}{2})}$, $\dot{u}^{(i-\frac{1}{2})}$ etc. is required for initial conditions, certain constraints, and presentation of results. For presentation of results, the state velocities are stored as a linear interpolation of the mean velocities:

$$\dot{u}^{(i+1)} = \dot{u}^{(i+\frac{1}{2})} + \frac{1}{2}\Delta t^{(t+1)}\ddot{u}^{(i+1)} \tag{4.16}$$

The central difference operator is not self-starting because the value of the mean velocity $\dot{u}^{(-\frac{1}{2})}$ needs to be defined. The initial values (at time t = 0) of velocity and acceleration are set to zero unless they are specified by the user. The following condition is assumed:

$$\dot{u}^{(+\frac{1}{2})} = \dot{u}^{(0)} + \frac{\Delta t^{(1)}}{2}\ddot{u}^{(0)} \qquad 4.17$$

Substituting this expression into the update expression for $\dot{u}^{(+\frac{1}{2})}$ yields the following definition of $\dot{u}^{(-\frac{1}{2})}$:

$$\dot{u}^{(-\frac{1}{2})} = \dot{u}^{(0)} - \frac{\Delta t^{(0)}}{2}\ddot{u}^{(0)} \qquad 4.18$$

The solution procedure using ABAQUS/Explicit module in this work is summarized as following steps:

a) At time step t, nodal accelerations are solved by dynamic equilibrium equation 4.15.

b) Nodal displacements and velocities are obtained by integrating nodal velocities and accelerations through time respectively using the central difference rule given by equations 4.13 and 4.14.

c) New element strains are updated by $d\varepsilon$ from the strain rates $\dot{\varepsilon}$.

d) Element stresses are then calculated from hyperelastic material constitutive law $\sigma_{t+\Delta t} = f(\sigma_t, d\varepsilon)$.

e) Nodal internal forces $I_{t+\Delta t}$ for the next time step are assembled from adjacent elements.

f) Set $t + \Delta t$ to t, and return to step a).

Explicit methods require a maximal time increment to maintain conditional stability, which normally results in many small time steps to complete an analysis. The critical maximal time increment solely depends on the worst elements with the minimal maximal time increment. Mass scaling features were used to keep those offending elements from hindering the stability limit without significantly affecting the result accuracy.

4.3. Contact and Chip Separation in Cutting Process Simulations

Contact can be treated as a severe boundary condition nonlinearity. It can cause the simulations to be difficult to converge and even terminate before completion. ABAQUS/Explicit provides excellent contact and interaction algorithms for simulating various contacting problems. Three basic surfaces, i.e., rigid surface, element-based surface and node-based surface, can be defined in ABAQUS/Explicit depending upon different applications. In this dissertation, a contact pair including a master rigid surface and a node-based slave surface is used because it has more options to define the contact properties. Note that a master surface can penetrate a slave surface; however, the nodes on a slave surface are constrained to not penetrate the master surface. Generally, the master surface is chosen as the surface of the stiffer body if the materials are different or as the surface with the coarser mesh. When one of the surfaces is rigid, that surface must always be the master. Since contact is enforced only at the nodes on the slave surface, it is important that the mesh be refined sufficiently to be able to follow the geometric detail of the master surface.

As shown in Fig 4.1, cutting tools with various geometries are modeled as a simplified master rigid surface with the normal direction pointing out towards the workpiece. A node-based deformable surface is used as the slave surface for the rubber workpiece because the chip separation during the cutting process generates new contact surfaces as the cutting tool advances and the location of the contact surfaces are unknown until the tool reaches that point to cause the underlying elements to fail. Note that the cutting tool can penetrate the workpiece and nodes on the workpiece are constrained not penetrate the cutting tool surface.

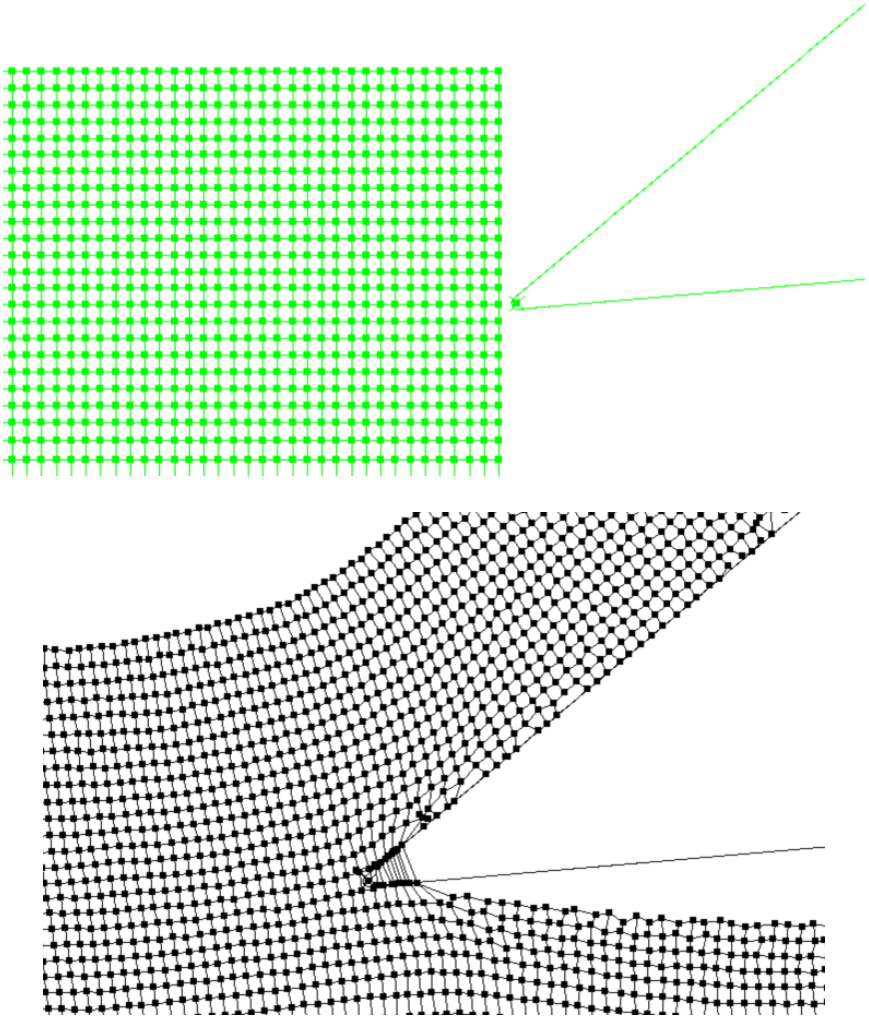

Figure 4.1. Modeling contact and chip separation using ABAQUS/Explicit.

A finite sliding and global contact search algorithm was used for each increment. ABAQUS/Explicit is designed to simulate highly nonlinear events or processes. Because it is possible for a node on one surface to contact any of the element edges on the opposite surface, ABAQUS/Explicit uses sophisticated search algorithms for tracking the motions of the contact surfaces. The contact search algorithm is designed to be robust, and computationally efficient. This algorithm assumes that the incremental relative tangential motion between surfaces does not significantly exceed the dimensions of the master surface elements, but there is no limit in the overall relative motion between surfaces. It is rare for the incremental motion to exceed the element size because of the small time increment used in explicit dynamic analyses. In cases involving relative surface velocities that exceed material wave speeds, it may be necessary to reduce the time increment.

For example in Fig. 4.2, the global search algorithm determines the globally nearest master surface element for each slave node in a given contact pair. The global search computes the distance from node 50 to all of the master surface elements. It determines that the nearest element on the master surface to node 50 is element 10. Node 100 is the node on this element that is nearest to node 50. In a master/slave contact pair, node 50 on the slave surface uses the face of element 10 on the master surface to determine the clearance between the tow surfaces at this location and moment. This search is conducted for each slave node, comparing each node against all of the elements on the master surface. Despite using an optimal sorting algorithm, global searches are computationally expensive. Performing a global contact search in every increment will more than double the run time of

ABAQUS/Explicit contact analyses, however, the proper contact between the master/slave contact pair is guaranteed (ABAQUS/Explicit User's Manual, 2002).

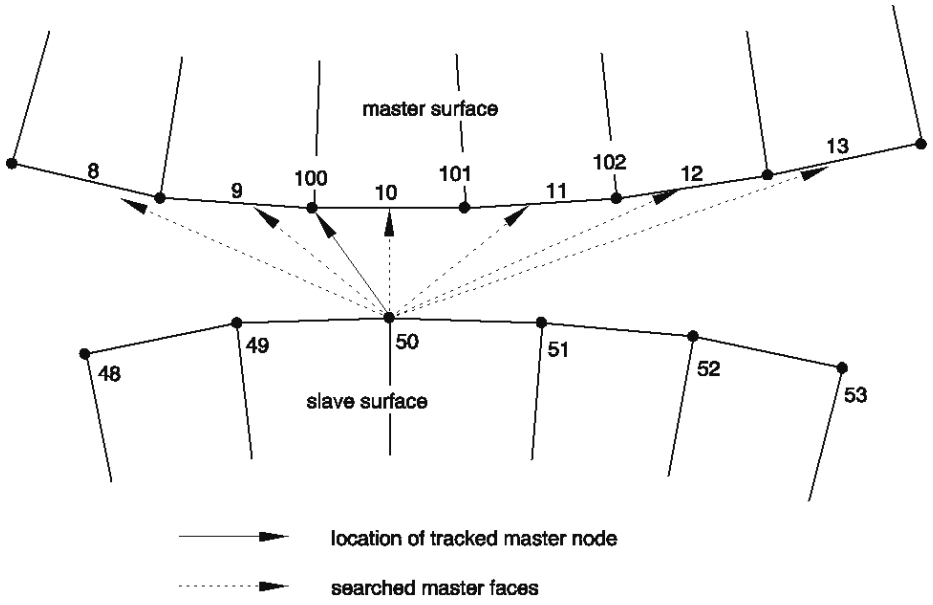

Figure 4.2. Global search scheme for surface contact.

Chip separation can also be easily modeled with ABAQUS/Explicit by using the element deletion option. As illustrated in Fig. 4.1, the algorithm checks for the specified failure criterion at the integration points for every element once every time incremental step. A contact between the node-based slave surface and the rigid surface is removed when its underlying element has failed and has been deleted from the workpiece mesh. As elements fail, contact surfaces will adapt to newly exposed node-based surfaces of elements that have not yet failed, which can be particularly useful for modeling contact involving chip separations. Note that a node-based surface that includes not just the initially exposed nodes but all nodes that might eventually become exposed to contact should be generated in the contact pair to model the chip separation process.

4.4. Hyperelastic Material Constitutive Model

A so-called hyperelastic material (or in the theoretical literature often called a Green-elastic material) postulates the existence of a Helmholtz free-energy function ψ, which is defined per unit reference volume rather than per unit mass. For the case in which $\psi = \psi(F) = \psi(U)$ is solely a function of the deformation gradient F or the symmetric right stretch tensor U, the Helmholtz free-energy function is referred to as the strain-energy function or stored-energy function, simply called strain energy or stored energy in most time. The strain-energy function $\psi = \psi(F)$ is a typical continuous scalar function of the tensor variable F. The response function of a hyperelastic material can be found as (Holzapfel, 2000), (ABAQUS Theory Manual, 2002), (Calcote, 1968):

$$P = \frac{\partial \psi(F)}{\partial F} \tag{4.19}$$

where P is the first Piola-Kirchoff stress tensor and the symmetric Cauchy stress tensor

$$\sigma = J^{-1} P F^T = J^{-1} \frac{\partial \psi(F)}{\partial F} F^T \tag{4.20}$$

where $J = \det(F)$ is the elastic volume ratio. Since the right Cauchy-Green stress tensor is given by $C = U^2$, we can write $\psi(F) = \psi(C)$. Also it can be easily derived that

$$\left(\frac{\partial \psi(F)}{\partial F}\right)^T = 2 \frac{\partial \psi(C)}{\partial C} F^T \tag{4.21}$$

which, when substituted back into equation 4.20, gives an important reduced form of the constitutive equation for hyperelastic materials, namely

$$\sigma = J^{-1}F(\frac{\partial \psi(F)}{\partial F})^T = 2J^{-1}F\frac{\partial \psi(C)}{\partial C}F^T \qquad 4.22$$

For an isotropic hyperelastic material, the strain energy can be further written by the identity $\psi(C) = \psi(b)$, where $\psi(b)$ characterizes an isotropic function of the left Cauchy-Green tensor $b = FF^T$. If a scalar-valued tensor function is an invariant under a rotation, it can be expressed in terms of the principal invariants of its argument, e.g. C or b. So the strain energy can be written as a set of independent strain invariants of the symmetric Cauchy-Green tensors C and b through $I_a = I_a(C) = I_a(b)$, $a = 1,2,3$, respectively. Equivalently,

$$\psi = \psi[I_1(C), I_2(C), I_3(C)] = \psi[I_1(b), I_2(b), I_3(b)] \qquad 4.23$$

In order to determine constitutive equations for isotropic hyperelastic materials in terms of strain invariants, consider a differentiation of $\psi(C) = \psi(I_1, I_2, I_3)$ with respect to tensor C. Assume $\psi(C)$ has continuous derivatives with respect to the principal invariants I_a, $a = 1,2,3$. By means of the chain rule of differentiation, we can get

$$\frac{\partial \psi(C)}{\partial C} = \frac{\partial \psi}{\partial I_1}\frac{\partial I_1}{\partial C} + \frac{\partial \psi}{\partial I_2}\frac{\partial I_2}{\partial C} + \frac{\partial \psi}{\partial I_3}\frac{\partial I_3}{\partial C} \qquad 4.24$$

Rubber is modelled as a hyperelastic material. The material response can be described in terms of a strain energy potential, $\psi(\varepsilon)$, which defines the strain energy stored in the material per unit of reference volume (volume in the initial configuration) as a function of the strain at that material point. There are several forms of strain energy potentials available in ABAQUS/Explicit to model approximately incompressible isotropic rubber-like materials. A neo-Hookean material model was used in this study:

$$\psi(I_1, J) = C_{10}(I_1 - 3) + \frac{1}{D_1}(I_3 - 1)^2 \qquad 4.25$$

where C_{10}, D_1 are model parameters related to initial shear modulus μ_0 and bulk modulus K_0 as $\mu_0 = 2C_{10}, K_0 = 2/D_1$. I_1 is the first invariant of the deviatoric left Cauchy-Green deformation tensor $\overline{B}$, which is defined as $\overline{B} = \overline{F} \cdot \overline{F}^T$, and where $\overline{F} = I_3^{1/3} F$ is the distortion gradient and I_3 is the elastic volume ratio.

The constitutive equation for a neo-Hookean material is given by

$$\sigma = \frac{2}{I_3} C_{10} (\overline{B} - \frac{1}{3} tr(\overline{B}) I_1) + \frac{2}{D_1} (I_3 - 1) I \qquad 4.26$$

where σ is the Cauchy stress. A special user material subroutine with effective stress failure criterion was developed because the hyperelastic models in ABAQUS/Explicit do not incorporate a material failure mechanism, which is essential to simulate cutting processes. This material model coupled with the failure criterion was used in all elements in the workpiece mesh to simulate the cutting process. When the effective stress in one element near the tool tip reached the specified failure criterion, the element was identified and eliminated from the mesh. Therefore the separation of the chip from the machined surface was simulated as the tool advanced into the workpiece. Table 3.1 lists the material properties for the experimental rubber material. The stress strain curve for the experimental material is obtained from uniaxial tension tests and it is shown in Fig. 4.3. The neo-Hookean hyperelastic material model coefficients were obtained from a least square fit of the uniaxial tension test data to be:

$$C_{10} = 1.84E6, D_1 = 4.48E-10 \qquad 4.27$$

The average coefficient of friction on the chip-tool interface used in the simulations is provided by Lord Corporation as a generic coefficient of friction between steels and rubber of 0.8.

Table 4.1. Material properties for test rubber samples.

Density (Kg/m^3)	CTE (1/K)	Thermal Conductivity (W/m K)	Specific Heat (J/Kg K)	Failure Stress (MPa)	Failure Strain (%)
1104.43	4.8E-4	0.145	1500	11.0	500

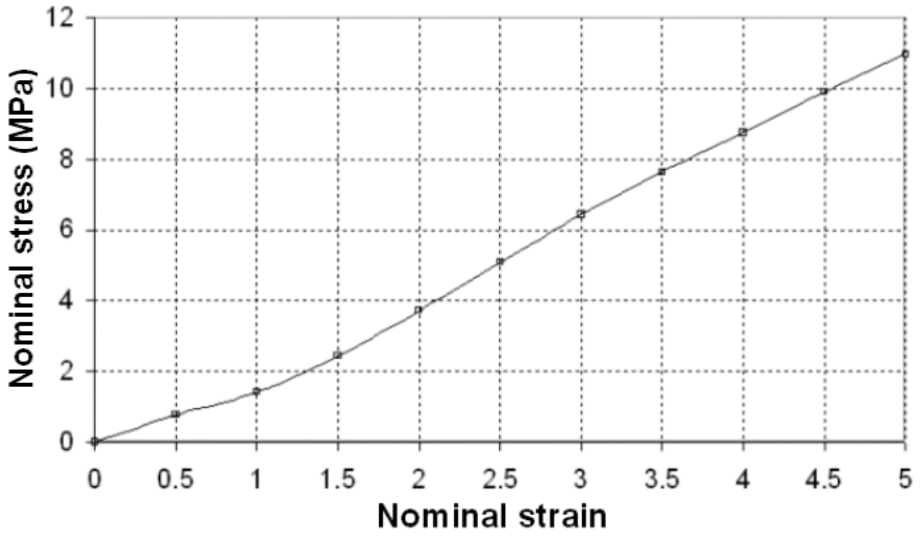

Figure 4.3. Stress strain curve from uniaxial tension tests for the experimental material.

4.5. Finite Element Model of Rubber Cutting

A finite element analysis of orthogonal rubber cutting was conducted using experimentally determined material properties to predict the cutting forces, chip shape and machined surface profile. Cutting parameters are listed in Table 4.2. The 2D plane strain finite element model is shown in Fig. 4.4 with the initial and deformed meshes. Plane strain conditions are satisfied because the width of the cut (11.61 mm) is much greater than the uncut chip thickness (less than or equal to 0.254 mm) and the cutting edge length of the tool (40 mm) is

much larger than the width of the cut. A workpiece length of 6.25 mm was used that is more than 20 times the uncut chip thickness to ensure reaching the steady state solution. The bottom nodes of the workpiece were fixed along the horizontal and vertical directions to satisfy the appropriate displacement boundary condition. The tool was constrained to move along the cutting direction (x-direction) with a constant velocity of 2.4 m/s. A finer mesh was used along the cutting path to ensure achieving more accurate solutions in the high stress and strain gradient zone.

The workpiece was modelled with plane strain four node bilinear elements CPE4R. Reduced integration and hourglass control techniques were used to deal with the large elastic deformation and near incompressibility of the workpiece material. The tool was modelled as a rigid body because of the significantly high modulus of the HSS tool material (~200 Gpa) compared to that of rubber (10^{-1}~10 Mpa). The tool tip radius was measured to be 0.008 mm (See section 3.2.5 for tool tip radius measurement). The rate and temperature-dependent material properties were ignored due to the relatively low cutting speeds.

Table 4.2. Summary of cutting parameters for the simulations.

Rake angle (°)	Clearance angle (°)	Cutting speed (m/s)	Feed rate (mm/rev)	Tool tip radius (mm)
10,30,50,70	5,10,20	2.4	0.064,0.127,0.254	0.008

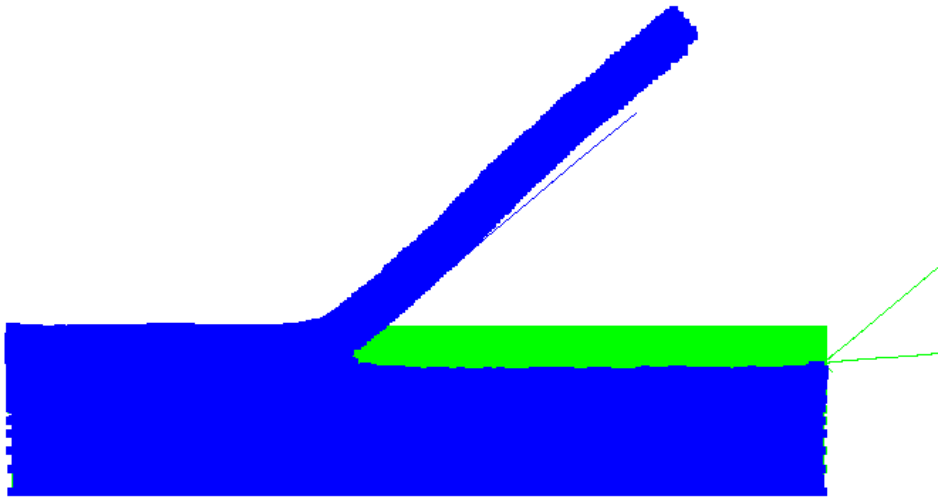

Fig. 4.4. Initial (green) and deformed (blue) meshes for the finite element cutting model.

4.6. Numerical Simulation Results

In metal cutting, there is a distinct shear zone in the primary zone in front of the tool and it is appropriate to use an effective shear strain criterion in FE simulations of metal cutting. Figure 4.5 shows the Tresca stress contours for metal cutting with a 20º rake angle tool. This figure shows that a distinct shear zone is generated during cutting, which extends from the tool tip to the free edge of the workpiece. Note that the Tresca stress is equivalent to twice the max shear stress.

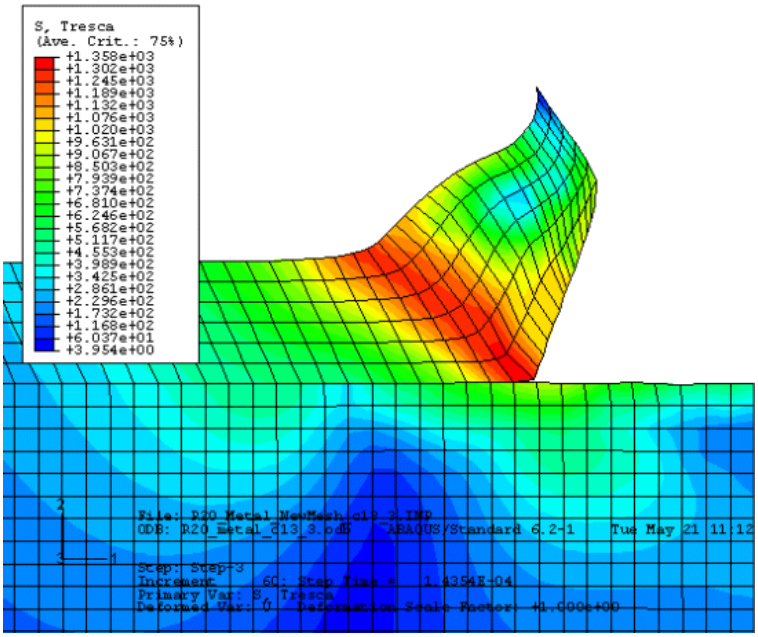

Fig. 4.5. Tresca stress contours for metal cutting with a 20º rake angle tool (Rodkwan, 2002).

Although each molecular sequence of an elastomer is anisotropic, an elastomer consists of millions of such randomly distributed strands that are entangled with each other by crosslinking and therefore it is assumed macroscopically homogeneous and isotropic. Unlike most metallic materials that have a crystal atomic structure and form a slip plane under deformation, elastomers are typically categorized as amorphous polymers having a random-coil molecular arrangement. This unique molecular structure most likely helps to explain why a different failure criterion is needed for simulating the rubber cutting process other than the effective plastic shear strain criterion used in metal cutting simulations.

A series of rubber cutting simulations was conducted to determine the fundamental mechanism of chip formation. Figure 4.6 shows the Tresca stress contour for rubber cutting with a 30º rake angle tool. It can be seen that no distinct shear band exists ahead of the cutting tool for rubber during this simulation. After carefully evaluating the corresponding

machined surfaces and chips, no apparent shearing phenomenon was observed as compared to an equivalent metal cutting process. Therefore, it can be concluded that a different failure criterion other than the effective shear strain is needed for simulating chip formation in rubber cutting. After evaluating several failure criteria in the cutting simulations, the von Mises stress failure criterion was found to be the most suitable choice for rubber cutting simulations with respect to the chip formation process and comparison to the orthogonal cutting experiments. Note that the von Mises stress failure criterion has been derived from a strain energy theory and it is widely used for polymeric materials, such as plastics (Bartenev and Zuyev, 1968), (Gent, 2001). Strain energy and fracture mechanics theory will be used to explain the mechanism to form a smooth surface for rubber cutting in the latter part of this section.

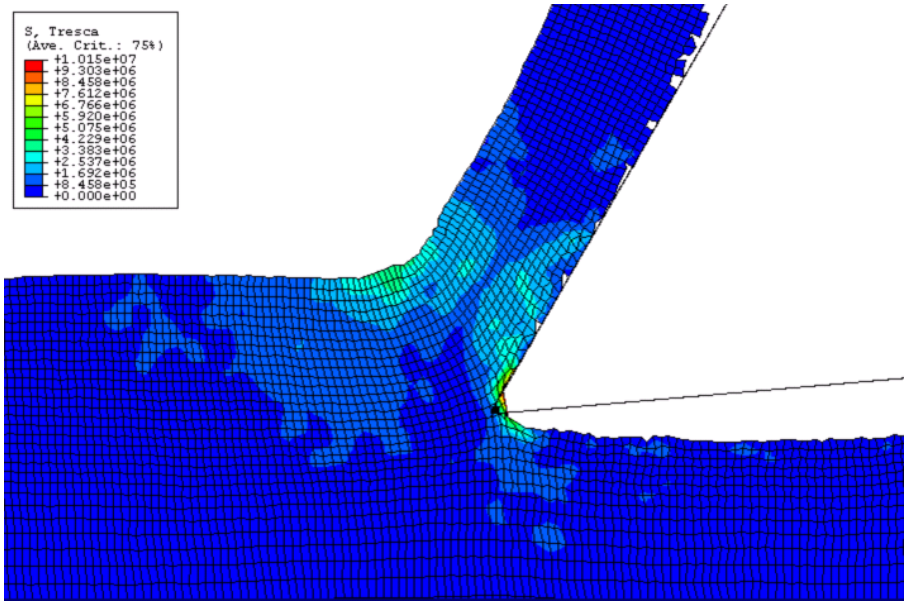

Fig. 4.6. Tresca stress contours for rubber cutting with a 30º rake angle tool.

A complete sequence of a rubber cutting simulation with a tool with a 50° rake angle and 5° clearance angle is illustrated in Fig. 4.7. The entire process includes several stages, such as the initial contact, chip initiation, and steady state cutting, which would occur in an orthogonal rubber cutting process. A rigid tool with a rake angle of 50° is pressed against the vertical surface of a rubber workpiece and incrementally advanced. As the tool moves forward, nodes are separated due to the deletion of "dead" elements from the workpiece mesh which allows the chip to form. This simulation is believed to be the first successful attempt at modeling the continuous transition to steady rubber cutting. It also proves that commercial finite element codes such as ABAQUS/Explicit have the capability to simulate the rubber machining process provided suitable user material subroutines are incorporated into the program and an appropriate failure criterion is defined.

Figure 4.8 shows detailed views of the von Mises and Tresca stress contours near the tool tip for an orthogonal rubber cutting process with a tool with a 50° rake angle and 5° clearance angle. As can be seen, both the high von Mises stress and Tresca stress are concentrated at the tool tip area and there does not exist an apparent shear zone extending from the tool tip to the free edge of the workpiece as found in the metal cutting simulations. As mentioned previously, rubber material models are expressed in terms of the strain energy or distortion energy. The von Mises stress failure criterion was derived by associating the distortion energy in a unit volume with the distortion energy per unit volume in a tensile test specimen at failure (Norton, 1997). Therefore, a von Mises stress failure criterion was appropriate to use in the simulations.

Also note that in comparison to the metal cutting simulation shown in Fig. 4.5, the actual machined surface is much lower than a horizontally projected chip separation line in the rubber cutting simulations. This is due to the extremely low modulus of rubber and the large deformation occurring during the cutting process. This demonstrates that machining rubber to a precise final dimension is a challenge. It is essential that effective means are implemented to improve the rigidity of the workpiece and to use stable fixtures to machine precision components.

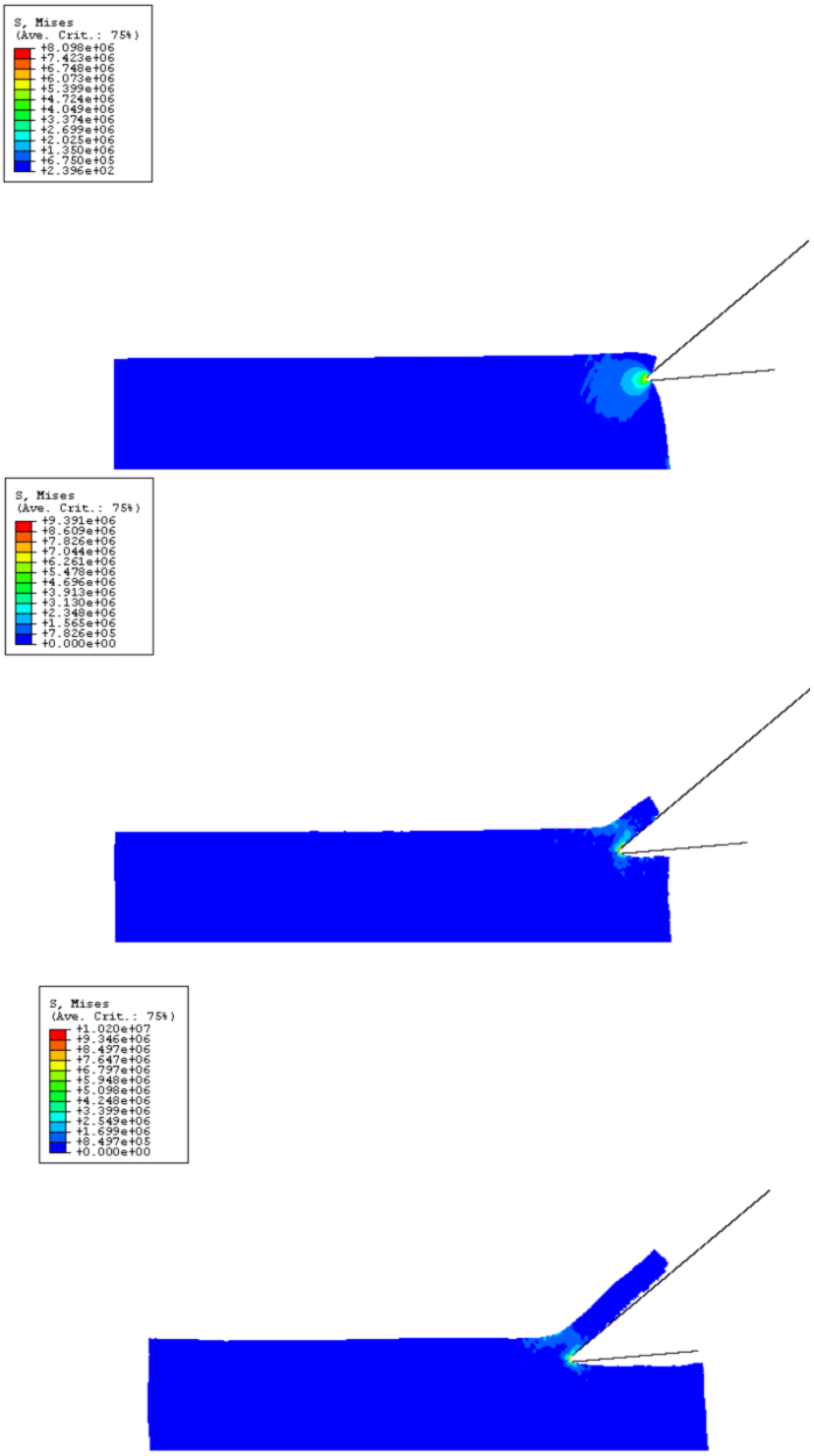

Fig. 4.7. Continuous chip formation process in orthogonal rubber cutting process with a tool of 50° rake angle and 5° clearance angle.

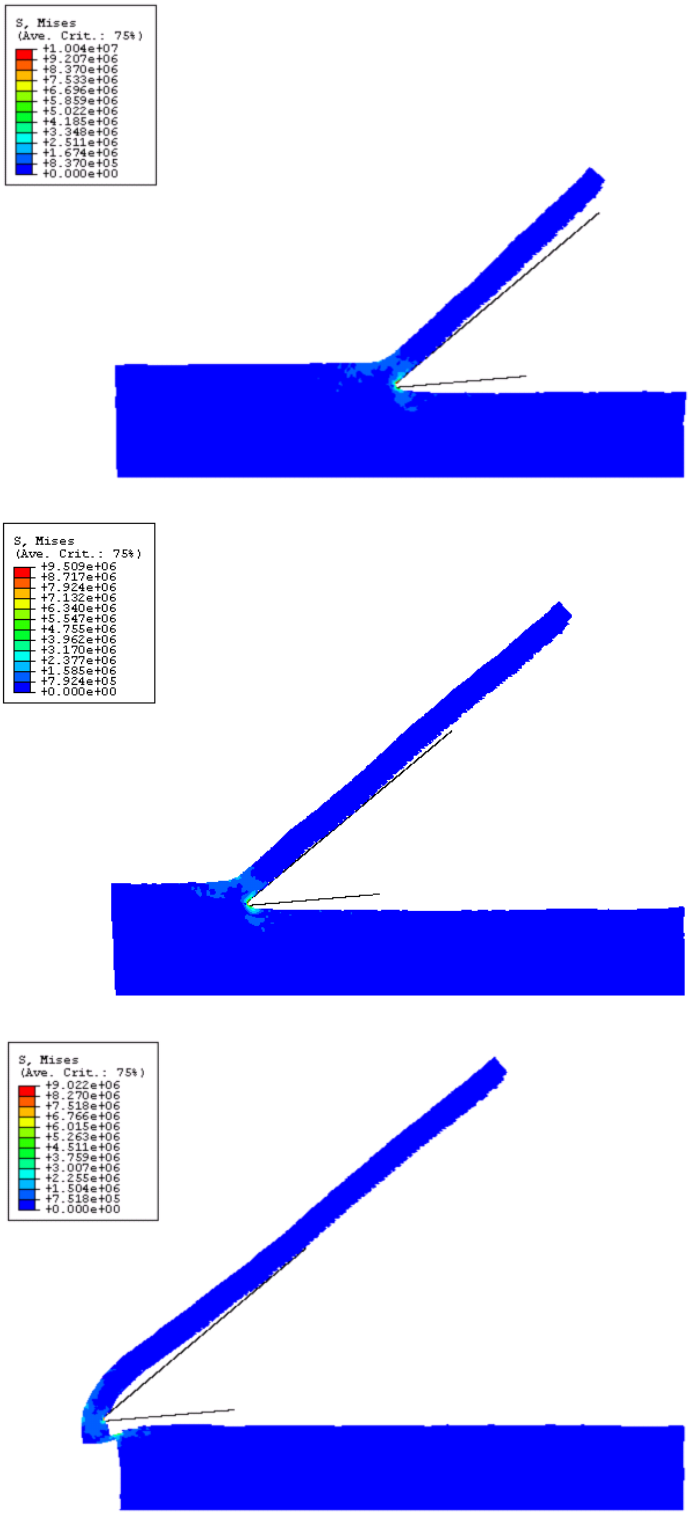

Fig. 4.7. Continuous chip formation process in orthogonal rubber cutting process with a tool of 50° rake angle and 5° clearance angle. (Continued)

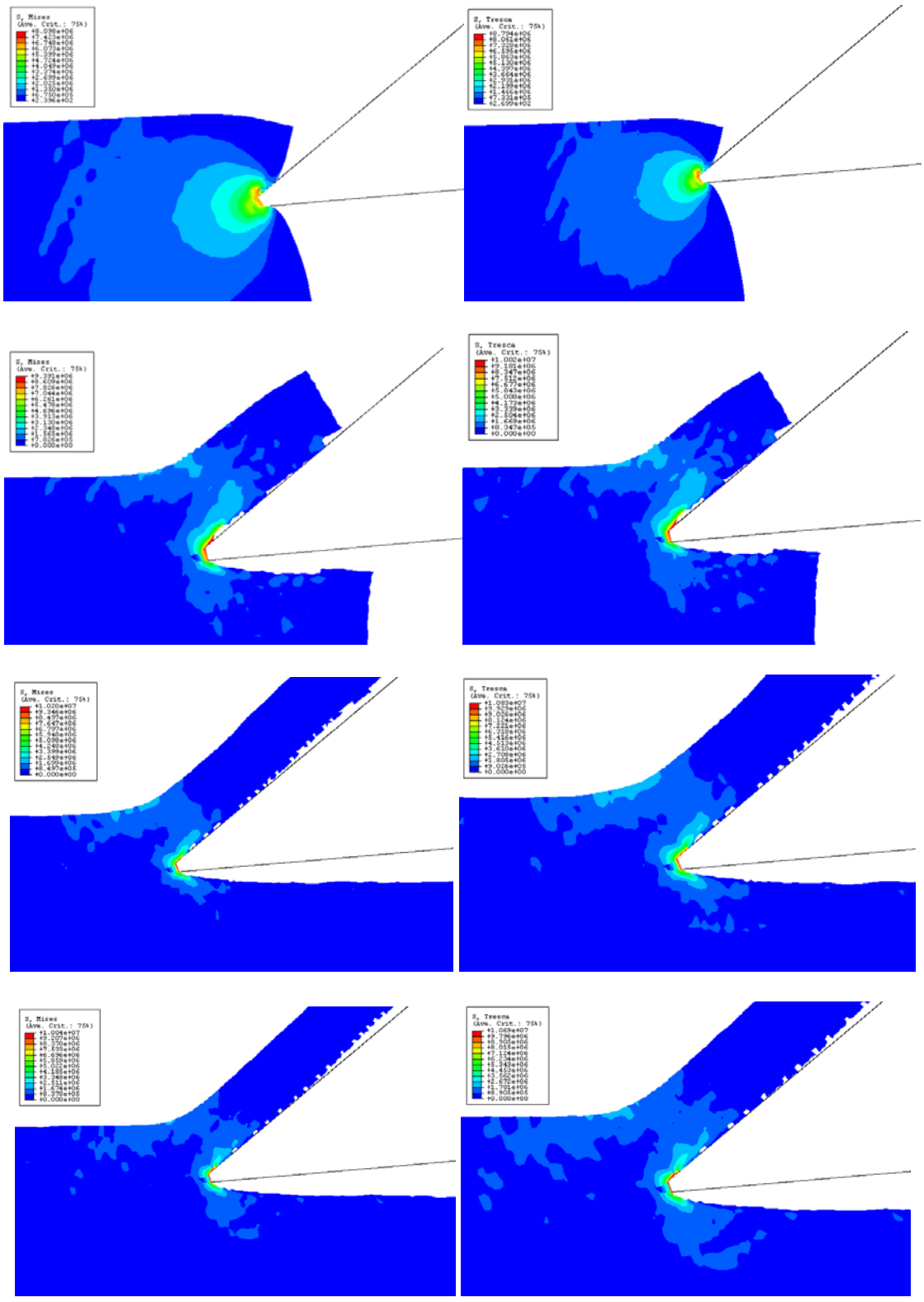

Fig. 4.8. Enlarged views of the von Mises (left) and Tresca (right) stress contours for orthogonal rubber cutting process with a tool of 50° rake angle and 5° clearance angle.

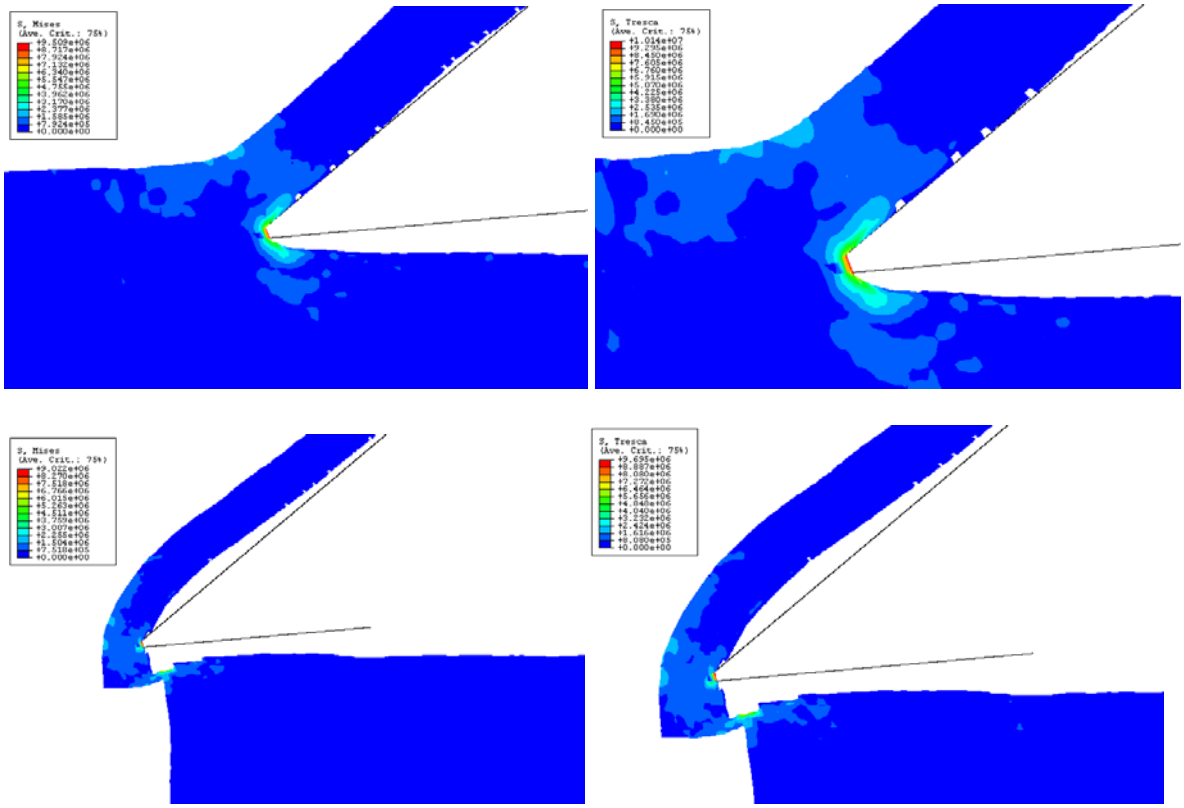

Fig. 4.8. Enlarged views of the von Mises (left) and Tresca (right) stress contours for orthogonal rubber cutting process with a tool of 50° rake angle and 5° clearance angle (Continued).

The predicted von Mises stress contours are shown in Figs. 4.9 ~ 4.11 for tools with rake angles of 10°, 30° and 50°, respectively. These figures also show photographs of the actual chips and machined surfaces that were obtained in the cutting experiments. Note that in Fig. 4.9, the simulation predicted a discontinuous chip and rough machined surface that agrees well with the chips and machined surfaces obtained in the experiments. Similarly, Fig. 4.11 shows that the simulation predicted a continuous chip with small curvature and smooth machined surface that matches the experimental results. From previous work it has been shown that the morphology of rubber chips can be categorized into three basic types: (1)

continuous ribbon-like chips with a smooth machined surface, (2) segmented chips with a rough machined surface, and (3) discontinuous chips with an even worse surface finish, respectively. Continuous ribbon-like chips are associated with a smooth surface finish, which occurs with large rake angle tools. In contrast, large cutting forces and discontinuous chips are associated with a rough machined surface that results from cutting with small rake angle tools. The simulations show good agreement with these experimental results.

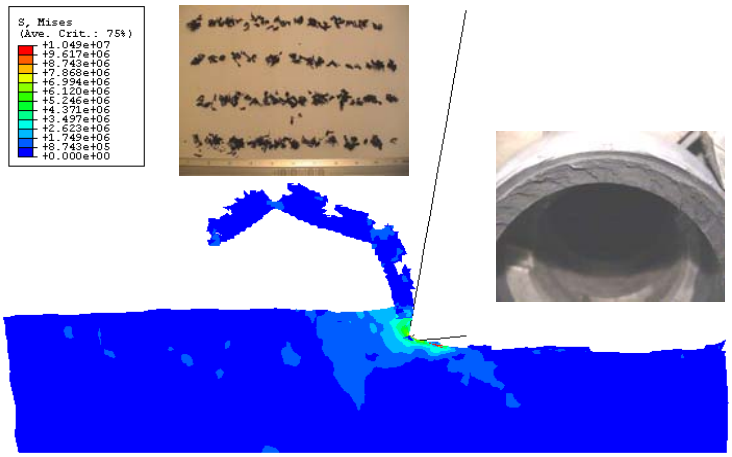

Fig. 4.9. Discontinuous chips and rough machined surface with a tool of 10° rake angle.

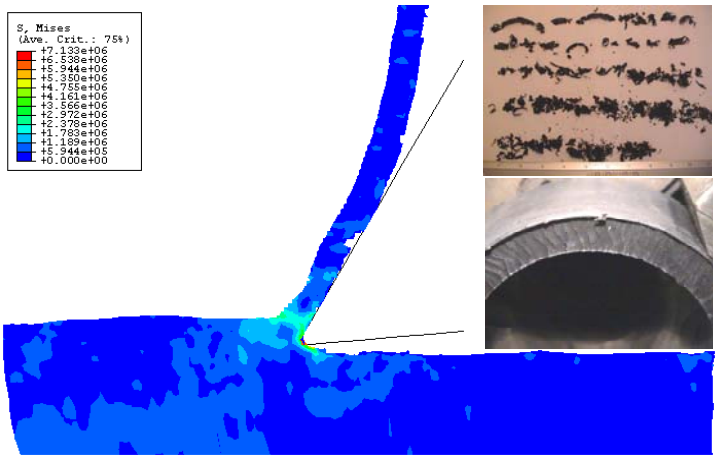

Fig. 4.10. Mixed chip shape and wavy machined surface with a tool of 30° rake angle.

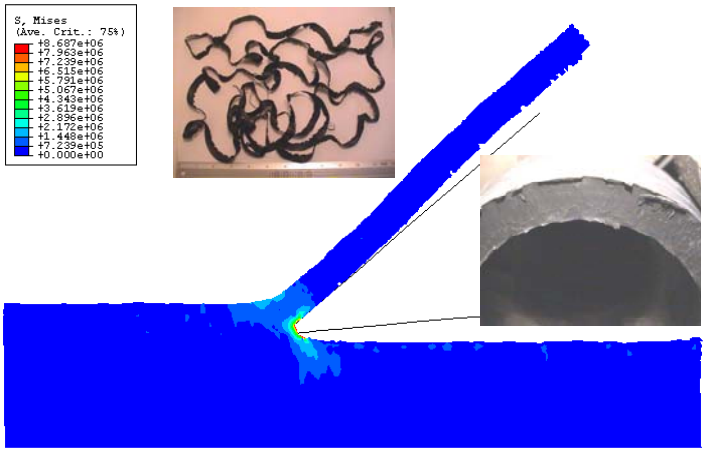

Fig. 4.11. Continuous ribbon-like chips and smooth machined surface with a tool of 50° rake angle.

Figure 4.12 shows the measured and predicted principal and thrust force components as a function of the rake angle for two feeds of 0.127 and 0.254 mm/rev, respectively. It was found that the rake angle was the most important geometric tool parameter and its value dramatically affected cutting performance. For example, the cutting force decreases 55% from about 220 Newton to a low of 100 Newton as the rake angle increases from 10° to 50°. The figure also shows a comparison between the measured forces and those predicted by the model. Good correlation was found for cutting forces over the entire range of rake angles and test feeds. The maximum discrepancy for principal cutting forces is found to be 24% for a tool of 50° rake angle and at 0.127 mm/rev feed rate. A 30° rake angle tool produces a maximum 26% discrepancy between the measured and predicted thrust cutting forces at a feed rate of 0.254 mm/rev.

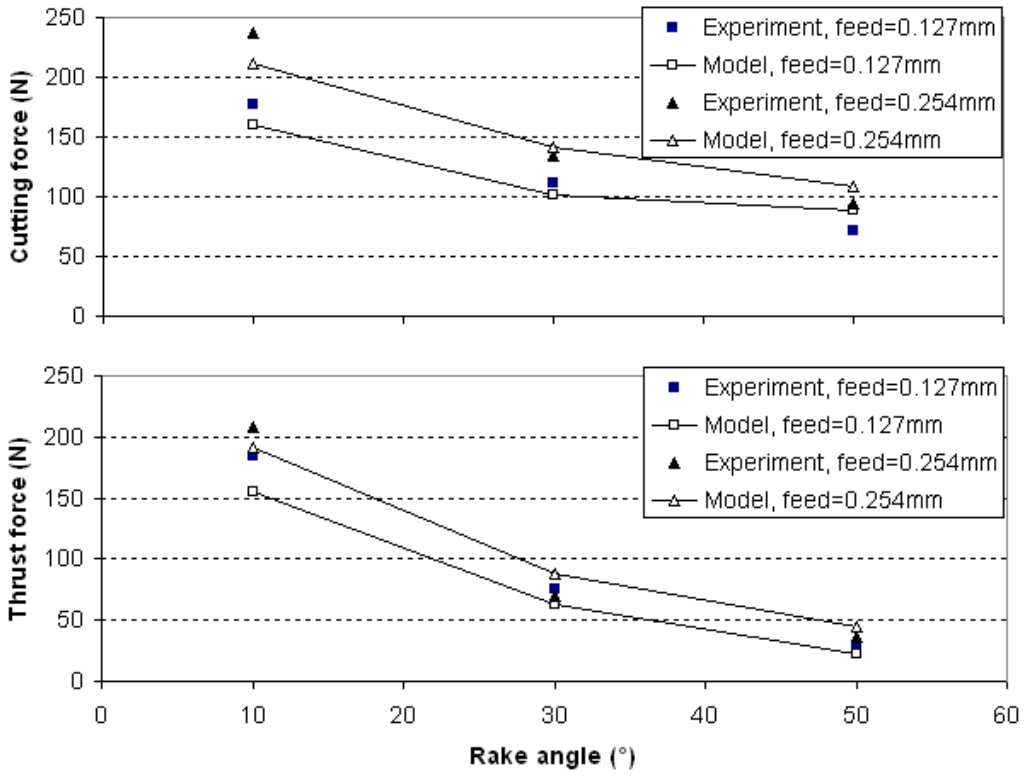

Fig.4.12. Comparison of predicted and measured cutting forces for a cutting speed of 2.4 m/s.

The stress and strain distribution on the workpiece directly under the tool clearance face along the principal direction were studied. Figures 4.13 and 4.14 show the stress and strain contours for cutting with a 70° rake angle tool, respectively. Note that for cutting that produces a smooth machined surface, apparent tensile stress and positive strain in the cutting direction were found on the machined surface near the cutting tool tip.

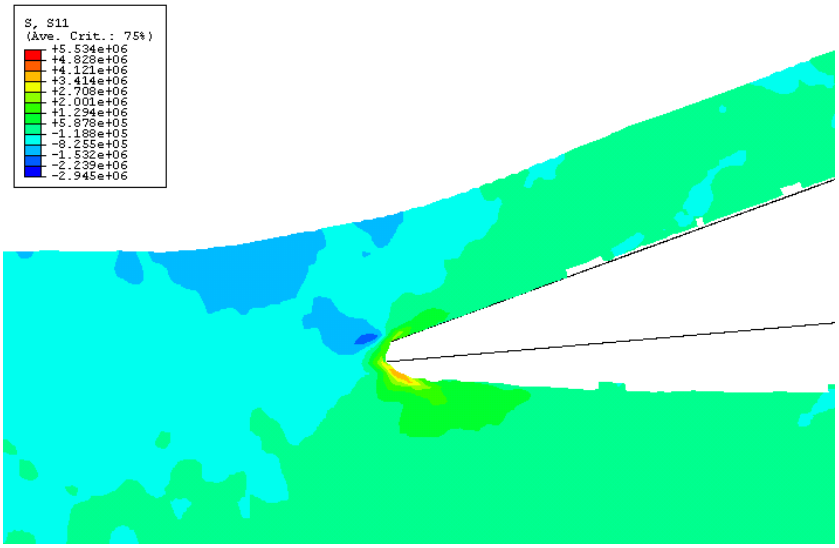

Fig. 4.13. Predicted normal stress contours (MPa) in cutting direction for cutting with a tool of 70° rake angle.

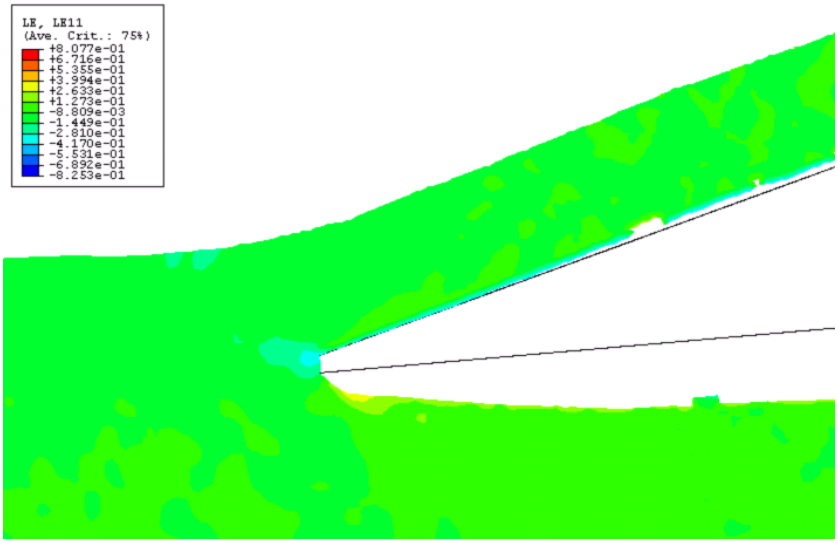

Fig. 4.14. Predicted logarithmic strain contours in cutting direction for cutting with a tool of 70° rake angle.

A primary objective of this research was to determine the conditions for which rubber can be machined with a smooth surface finish. Understanding the chip formation process is critical for establishing optimal cutting conditions to achieve a smooth surface finish. Enlarged views of the strain energy density contours before and after chip separation in the vicinity of the cutting edge are shown in Figs. 4.15 and 4.16 for rake angles of 10° and 50°, respectively. There is a distinct difference in energy distribution in the cutting zones of the workpiece for the small rake angle and large rake angle tools. The strain energy density near the tool edge is not only higher but also extends over a larger region for the 10° rake angle tool as compared to the 50° rake angle tool. For example, the maximum strain energy densities are 3.67 and 4.23 MPa for cutting with a 10° rake angle tool before and after the chip separation, respectively. They are lower (3.2 and 3.79 MPa) for cutting with a 50° rake

angle tool. Also note that for the 10° rake angle tool, the high strain energy density zone extends from the cutting edge to nearly the free surface of the workpiece before chip separation, which would result in discontinuous chip formation and more surface damage.

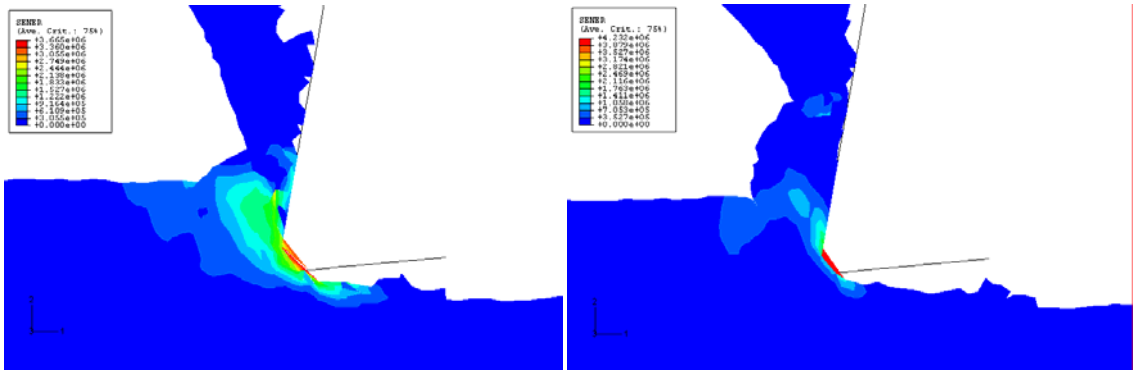

(a) (b)

Fig. 4.15. Strain energy density contour near the tool tip for a 10° rake angle tool (a) before chip separation and (b) after chip separation.

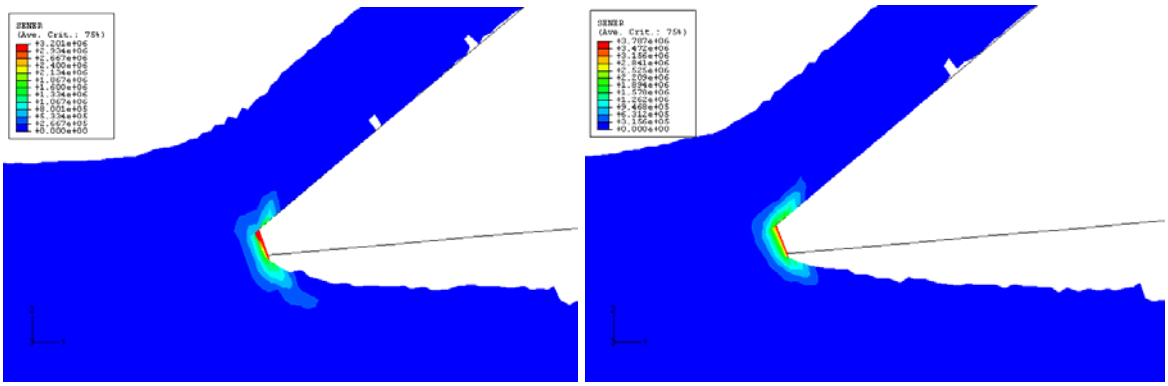

(a) (b)

Fig. 4.16. Strain energy density contour near the tool tip for a 50° rake angle tool (a) before chip separation and (b) after chip separation.

Figure 4.17 shows the history of the strain energy as a function of the cutting time. Again it shows that significantly more strain energy is stored in the workpiece during cutting with the small rake angle tool. In addition, as the tool is advanced into the workpiece, large deformation of the workpiece occurs until the effective stress reaches the strength of the rubber (11 Mpa). When the chip separates from the workpiece, there is a large release of strain energy as the material is unloaded. Note that the strain energy necessary to separate the chip is a characteristic of the rubber itself and independent of the overall shape of the test piece. A similar situation of strain energy release occurs when a crack propagates. The strain energy available to drive a crack is defined as (Gent, 2001), (Boast and Coveney, 1999):

$$-\frac{\partial W}{t\partial a} = G \tag{4.28}$$

where W is the total strain energy in the workpiece, t is the thickness of the workpiece, and a is the crack length. The quantity G is a material constant and termed the "strain energy release rate", "tear energy" or "rupture energy". As shown in Fig. 4.17 (a), because a large amount of strain energy (0.5 ~ 1 MPa) is released, a larger number of chemical bonded crosslinks will be broken and a longer "zigzag" chip separation path is generated that releases a large amount of energy as the tool advances during each step. Therefore, discontinuous chips and a roughened machined surface with more surface crack areas will be generated. In contrast for a 50° rake angle tool, the strain energy release shown in Fig. 4.17 (b) is smoother and significantly reduced (around 0.1 MPa or less) as the tool is advanced the same distance. Because G is a constant, it can be concluded that the chip separation path length must also be smaller for the same tool step. Therefore, continuous chips and a smooth machined surface are more likely to be produced by this type of tool. Recall that small rake angle tools

produced a rough machined surface corresponding to a “zigzag” chip separation path as shown in Figs. 3.15 and 3.16. In contrast, large rake angle tools generated a much smooth surface, which would correspond to a shorter chip separation path.

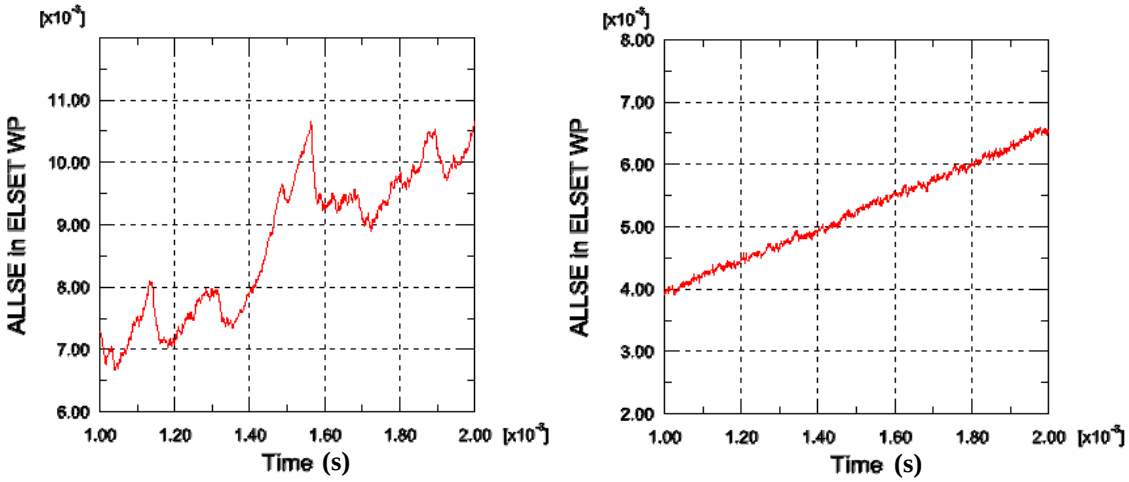

(a) (b)

Fig. 4.17. Strain energy history plots of the workpiece for cutting with (a)10° rake angle tool and (b) 50° rake angle tool.

Recall from the discussion in previous chapters that a well-designed and stable fixture and lower workpiece temperatures are beneficial for generating a smooth machined surface. Note that even with a large strain energy release associated with small rake angle tools, it is still possible to improve the surface quality by increasing the workpiece rigidity.

4.7. Concluding Remarks

A plane strain finite element model was developed using ABAQUS/Explicit for simulating the orthogonal rubber cutting process. A Neo-Hookean hyperelastic material model was implemented with a user material subroutine to simulate the nonlinear mechanical behavior of a rubber-like material. The model was used to predict the cutting forces, chip shape, stress and strain contours, and the strain energy density field in the chip and workpiece. Good agreement was found between the predicted and measured cutting forces. The FE simulation has demonstrated that the model can be used to predict the chip formation of the rubber cutting process. Tensile stress and positive strain in the cutting direction in the workpiece directly underneath the clearance face of the tool tip was observed when a smooth surface was produced. The strain energy density contours near the tool edge were found to be not only higher but they also extended over a larger area when a rough surface was generated. It was also found that the strain energy release rate was closely related to the machined surface quality. A large strain energy release rate corresponds to the formation of a rough surface. In conclusion, the finite element model provides new insight into the chip formation mechanism in rubber cutting by using a strain energy explanation. With this understanding, future guidelines can be developed for operating conditions that result in a smooth machined surface finish for machining of rubber components.

5. CONCLUSIONS AND FUTURE WORK

5.1. Conclusions

In this dissertation, an investigation of the machinability of elastomers was undertaken using orthogonal cutting experiments and finite element simulations of the cutting process. In the orthogonal cutting tests, a wide variety of cutting parameters were examined. Cutting forces, machined surface roughness and temperature were measured to evaluate the effect of various operating parameters. Finite element models using the ABAQUS/Explicit code and user-provided hyperelastic material subroutines were developed to simulate the orthogonal cutting process of elastomers. Strain energy and the strain energy release rate were used to explain the mechanism for producing a smooth machined surface.

The effect of rake angle, clearance angle, feed rate, cutting speed and workpiece temperature was examined in the orthogonal cutting experiments. The rake angle of the tool plays an important role in generating a smooth machined surface. A smooth surface with continuous ribbon-like chips is produced with tools with a large rake angle. In contrast, rough surfaces and discontinuous chips are generated when tools with a small rake are used. The corresponding cutting force components decrease as the rake angle increases. The temperature rise rate for cutting with a large rake angle tool is low compared with that for a small rake angle tool. Low workpiece temperatures help to produce a smooth machined surface due to the increased rigidity of rubber. Cryogenic machining is useful to obtain a smooth machined surface. It also can be used to keep the temperature of the rubber

workpiece from reaching critical values, such as the melting point, due to excessive heat generation during the machining processes. The duration of rubbing before and after the actual cutting action should be shortened to reduce the temperature rise. Large feed rates contribute to both a shorter rubbing duration and a lower machined surface temperature rise rate which leads to a controlled machined surface temperature and a better machined surface quality. Notably, the cutting process itself does not change the machined surface temperature significantly.

A plane strain finite element model was developed using ABAQUS/Explicit for simulating the orthogonal rubber cutting process. A neo-Hookean hyperelastic material constitutive model and a von Mises failure criterion were used to simulate the nonlinear mechanical behavior of elastomers during the cutting process. The model was used to predict the cutting forces, chip shape, stress and strain contours, the strain energy density field, and strain energy history in the chip and workpiece. Good agreement was found between the predicted and measured cutting forces. The FE simulation demonstrated the ability of the model to predict the chip formation characteristics of rubber cutting. Tensile stress and positive strain in the cutting direction in the workpiece machined surface near the tool tip were observed when a smooth surface was produced. The strain energy density contours near the tool edge are not only higher but also extend over a larger area when a rough surface has been generated. It was found that the strain energy release rate is closely related to the machined surface quality. A large strain energy release rate corresponds to the formation of a rough surface. In summary, the FE model provides new insight into the chip formation mechanism for rubber cutting using the strain energy explanations. With this understanding, future

guidelines can be developed for operating conditions that result in a smooth machined surface finish for machining of rubber components.

5.2. Recommendations for Future Work

This research has demonstrated that the finite element model can be used to predict cutting forces, chip shape, stress and strain contours, the strain energy density field, and strain energy history in the chip and workpiece. Several aspects of the model should be addressed in the future to further improve the model. These include:

1. More complete material test data is needed for a wide variety of elastomers, including uniaxial tension, equi-biaxial tension, simple shear, planar shear, simple compression, and bulk compression tests.
2. The accuracy of the hyperelastic material constitutive models can be improved by incorporating temperature and strain rate effects.
3. Improving the finite element models for rubber cutting by including more accurate material constitutive models and more accurate frictional models at the tool-workpiece interface.
4. The study of elastomer machining mechanisms based on energy methods and fracture mechanics, such as strain energy and rupture strength, should be continued.
5. High speed machining studies of elastomers need to be conducted with special customized tools that incorporate large rake angles to better understand the machining behavior under large strain rates.

6. Cryogenic cutting is beneficial for achieving a smooth machined surface. Therefore, further cutting tests with a workpiece that is cooled with liquid nitrogen are suggested.

REFERENCES

ABAQUS Theory Manual, ver. 6.3, (2002). Hibbit, Karlsson, and Sorenson, Inc., Province, RI.

ABAQUS/Explicit User's Manual, ver. 6.3, (2002). Hibbit, Karlsson, and Sorenson, Inc., Province, RI.

Arruda, E.M., and Boyce, M.C. (1993). J. of Mech. Phys. Solids., Vol. 41, pp. 389.

ASTM D1566-00, (2000). Standard Terminology Relating to Rubber, American Society for Testing of Materials.

Athavale, S.M., Strenkowski, J.S. (1997). Material Damagebased Model for Predicting Chip-breakability, J. of Manufacturing Sciences and Engineering, Vol. 119, 4B, pp.675-680.

Bartenev, G. M., and Zuyev, Yu. S. (1968). Strength and Failure of Visco-elastic Materials, Oxford, New York.

Bhowmick, A.K., and Stephens, H.L (2001). Handbook of Elastomers, Marcel Dekker, Inc., New York.

Boast, D., and Coveney, V.A. (1999). Finite Element Analysis of Elastomers, Professional Engineering Pub., London.

Briscoe, B.J., and Sebastian, K.S. (1993). Rubber Chem. Technol.

Calcote, L. R. (1968). Introduction to Continuum Mechanics, Princeton, N.J.

Chandrupatla, T.R., and Belegundu, A.D. (2002). Introduction to Finite Elements in Engineering, Prentice-Hall.

Ciullo, P.A., and Hewitt, N. (1999). The Rubber Formulary, ChemTec Publishing.

Cook, R. D., (1974). Concepts and Applications of Finite Element Analysis; A Treatment of the Finite Element Method as Used for the Analysis of Displacement, Strain, and Stress, New York, Wiley.

Flory, P.J. (1953). Principles of Polymer Chemistry, Cornell University, Ithaca, New York.

Gent, A.N. (2001). Engineering with Rubber – How to Design Rubber Components, Hanser Publishers, Munich.

Guo, Y.B., and Liu, C.R. (1999). Finite Element Analysis of the Effect of Sequential Cuts and Tool-chip Friction on Residual Stresses in A Machines Layer, Int. J. of Mechanical Sciences, Vol. 42, pp.1069-1086.

Guo, Y.B., and Liu, C.R. (2002). 3D FEA Modeling of Hard Turning, ASME J. of Manuf. Sci. and Eng., Vol. 124, 2, pp.189-199.

Guo, Y.B., and Dornfeld, D.A. (2000). Finite Element Modeling of Burr Formation Process in Drilling 304 Stainless Steel, J. of Manufacturing Science and Engineering, Vol. 122, pp. 612-619.

Handheld Infrared Thermocouple Operator's Manual. Omega Engineering, Inc., Stamford, CT.

Harper , C.A. (1996). Handbook of Plastics, Elastomers, and Composites, McGraw-Hill.

Hinton, E. and Owen, D. R. J. (1977). Finite Element Programming, London, New York, Academic Press.

Holzapfel, G.A. (2000). Nonlinear Solid Mechanics, John Wiley & Sons.

Hong, S.Y., and Ding, Y. (2001). Cooling Approaches and Cutting Temperatures in Cryogenic Machining of Ti-6Al-4V, Int. J. of Mach. Tools Manufact., Vol. 41, 10, pp. 1417-1437.

Huang, J.M., and Black, J.T. (1996). An Evaluation of Chip Separation Criteria for the FEM Simulation of Machining, J. of Manuf. Sci. Eng., ASME, Vol. 118, pp.545-554.

Jin, M., and Murakawa, M. (1998). High-Speed Milling of Rubber (1st Report) - Fundamental Experiments and Considerations for Improvement of Work Accuracy, Journal of the Japan Society for Precision Engineering, Vol. 64, 6, pp. 897-901.

Kaliske, M., and Rothert, H. (1997). On the Finite Element Implementation of Rubber-like Materials at Finite Strains, Engineering Computations, Vol. 14, 2, pp. 216-232.

Lamperti, F. A., and Thurston, J. B. (1953). Internal Auditing for Management. Englewood Cliffs, NJ: Prentice-Hall.

Lewis, M.A. (2002). End Milling of Elastomers, NCSU Master Thesis.

Lin, S.Y. (1997). Surface Waviness Removed by Orthogonal Machine Cutting, Theor. Appl. Fract. Mech., Vol. 28, 1, pp. 69-80.

Lin, Z.C., and Lo, S.P. (2001). 2-D Discontinuous Chip Cutting Model by Using Strain Energy Density Theory and Elastic-plastic Finite Element Method, Int. J. Mech. Sci., Vol. 43, 2, pp. 381-398.

Lo, S.P. (2000). An Analysis of Cutting Under Different Rake Angles Using the Finite Element Method, J. of Materials Processing Technology, Vol. 105, pp. 143-151.

Long, H.E. (1985). Basic Compounding and Processing of Rubber, A.C.S. Rubber Division.

Mooney, M. (1940). J. of Applied Physics, Vol. 11, pp.582.

Murayama T. (1978). Dynamic Mechanical Analysis of Polymeric Material, Amsterdam, New York, Elsevier Scientific Pub. Co.

Ng, E.G., and. Aspinwall, D.K. (2002). Modeling of Hard Part Machining, J. of Materials Processing Technology, Vol. 127, pp.222-229.

Norton, R. L. (1997). Machine Design – An Integrated Approach. Prentice Hall.

Ogden, R.W. (1986). Rubber Chem. Technology, Vol. 59, pp.361.

Oxley, P. L. B. (1989). Mechanics of Machining. Ellis Horwood, Ltd., England.

Rodkwan, S. (2002). Numerical and Experimental Investigation of the Machinability of Elastomers, NCSU Ph.D. Dissertation.

Shaw, M. C. (2005). Metal Cutting Principles, New York, Oxford University Press.

Shet, C., and Deng, X. (2000). Finite Element Analysis of the Orthogonal Metal Cutting Process, J. of Materials Processing Technology, Vol. 105, pp. 95-109.

Shih, A.J. (1995). Finite Element Simulation of Orthogonal Metal Cutting, ASME J. Eng. Ind., Vol. 117, pp.84-93.

Shih, A.J. (1996). Finite Element Analysis of the Rake Angle Effects in Orthogonal Metal Cutting, International Journal of Mechanical Science, Vol. 38, pp. 1-17.

Shih, A.J., Lewis, M. A., and Strenkowski, J. S. (2004). End Milling of Elastomers – Fixture Design and Tool Effectiveness for Material Removal, ASME Journal of Manufacturing Science and Engineering, Vol. 126, pp. 115-123.

Shih, A.J., Lewis, M. A., Luo, J., and Strenkowski, J. S. (2004). Chip Morphology and Forces in End Milling of Elastomers, ASME Journal of Manufacturing Science and Engineering, Vol. 126, pp. 124-130.

Sneddon, I. (1975). Applications of Integral Transforms in the Theory of Elasticity, Springer-Verlag, New York.

Strenkowski, J.S., and Carroll, J.T. (1985). A Finite Element Model of Orthogonal Metal Cutting, ASME J. Eng. Ind., Vol. 107, pp.349-354.

Strenkowski, J.S. and Carroll, J. T. (1986). An Orthogonal Metal Cutting Model Based on An Eulerian Finite Element Method, Manufacturing Process Machines and Systems, 13th Conference on Production Research and Technology, U. of Florida, FL.

Strenkowski, J.S., Hseih C. J., and Shih, A.J (2004). An Analytical Finite Element Technique for Predicting Thrust Force and Torque in Drilling, International Journal of Machine Tools and Manufacture, Vol.44, pp.1413-1421.

Strenkowski, J. S. and Mitchum, G. L. (1987). An Improved Finite Element Model of Orthogonal Metal Cutting, Proceedings of North America Manufacturing Research Conference, Bethlehem, PA.

Strenkowski, J. S. and Moon, K. J. (1990). Finite Element Prediction of Chip Geometry and Tool/workpiece Temperature Distributions in Orthogonal Metal Cutting, Journal of Engineering for Industry, Vol. 112, 11, pp. 313-318.

Strenkowski, J.S., Shih, A.J, and Lin, J.C. (2002). An Analytical Finite Element Model for Predicting Three-dimensional Tool Forces and Chip Flow, International Journal of Machine Tools and Manufacture, Vol. 42, pp. 723-731.

Strenkowski, J.S., Shih, A.J., Luo, J., and Yan, J. (2004). The Use of Induction Heated Tools and Effective Fixture Design for Improving the Machinability of Elastomers, 2004 NSF Design, Service and Manufacturing Grantees and Research Conference Proceedings, Dallas, TX.

Strenkowski, J.S., Shih, A.J., Rodkwan, S., and Lewis, M.A. (2003). Machining of Elastomers – Experimental and Numerical Investigation, 2003 NSF Design, Service and Manufacturing Grantees and Research Conference, Birmingham, Alabama.

Strenkowski J.S., Yan J., Shih A.J., and Luo J. (2005). Improving the Machinability of Elastomers with Induction Heated Tools and Finite Element Cutting Models. 2005 NSF Design, Service and Manufacturing Grantees and Research Conference Proceedings, Scottsdale, AZ.

Timbrell, C., Wiehahn, M., Cook, G, and Muhr, A.H. (2003). Simulation of Crack Propagation in Rubber, Third European Conference On Constitutive Models For Rubber, London, UK.

Timoshenko, S.P., and Goodier, J.N. (1970). Mathematical Theory of Elasticity, 3rd Edition, McGraw-Hill, New York.

Treloar, L.R. (1975). The Physics of Rubber Elasticity, 3rd Edition, Charendon Press, Oxford.

Usui, E., Hirota, A., and Masuko, M. (1978). Analytical Prediction of Three Dimensional Cutting Process: Part 1 Basic Cutting Model and Energy Approach, ASME Journal of Engineering for Industry, Vol. 100, pp. 222-228.

Usui, E., Hirota, A., and Masuko, M. (1978). Analytical Prediction of Three Dimensional Cutting Process: Part 2, Chip Formation and Cutting Force with Conventional Single-point Tool, ASME Journal of Engineering for Industry, Vol. 100, pp. 229-235.

Walker B. M. (1979). Handbook of Thermoplastic Elastomers, New York.

Wang, B.P., Sadat, A.B., and Twu, M.J. (1988). Finite Element Simulation of Orthogonal Cutting – A Survey, Materials in manufacturing processes, MD, ASME WAM, Chicago, IL, Vol. 8, pp. 87-91.

Ward, I. M. (1983). Mechanical Properties of Solid Polymers, New York.

Williams, J.G., and Pavan, A. (2000). Fracture of Polymers, Composites, and Adhesives, Amsterdam, New York.

Yang, X.P., and Liu, C.R. (2002). A New Stress-based Model of Friction Behavior in Machining and its Significant Impact on Residual Stresses Computed by Finite Element Method, Int. J. of Mechanical Sciences, Vol. 44, pp. 703-723.

Yan J., and Strenkowski J.S. (2005). A Finite Element Analysis of Orthogonal Rubber Cutting, In Press, J. of Materials Processing Technology.

Yan J., and Strenkowski J.S. (2005). Finite Element Modelling of Rubber Cutting, In Press, Fourth European Conference on Constitutive Modelling of Rubber, Stockholm, Sweden.

Yan J., and Strenkowski J.S. (2005). An Experimental Study of Rubber Cutting Process, In Press, Fourth European Conference on Constitutive Modelling of Rubber, Stockholm, Sweden.

Yeoh, O.H. (1993). Rubber Chemistry Technology. Vol. 66, pp.754.

Zhang, L. (1999). On the Separation Criteria in the Simulation of Orthogonal Metal Cutting Using the Finite Element Method, J. of Materials Processing Technology, Vol. 89, pp. 273-278.

APPENDIX

Neo-Hookean Hyperelatic Material User Subroutine

This program is based on the derivation of hyperelastic material constitutive model in Section 4.4. A stress and strain relationship was derived from the neo-Hookean hyperelastic material constitutive model that is normally represented as the strain energy with strain invariants.

```
      subroutine vumat(
C Read only (unmodifiable)variables -
     1  nblock, ndir, nshr, nstatev, nfieldv, nprops, lanneal,
     2  stepTime, totalTime, dt, cmname, coordMp, charLength,
     3  props, density, strainInc, relSpinInc,
     4  tempOld, stretchOld, defgradOld, fieldOld,
     5  stressOld, stateOld, enerInternOld, enerInelasOld,
     6  tempNew, stretchNew, defgradNew, fieldNew,
C Write only (modifiable) variables -
     7  stressNew, stateNew, enerInternNew, enerInelasNew )
C
      include 'vaba_param.inc'
C
      dimension props(nprops), density(nblock), coordMp(nblock,*),
     1  charLength(nblock), strainInc(nblock,ndir+nshr),
     2  relSpinInc(nblock,nshr), tempOld(nblock),
     3  stretchOld(nblock,ndir+nshr),
     4  defgradOld(nblock,ndir+nshr+nshr),
     5  fieldOld(nblock,nfieldv), stressOld(nblock,ndir+nshr),
     6  stateOld(nblock,nstatev), enerInternOld(nblock),
     7  enerInelasOld(nblock), tempNew(nblock),
     8  stretchNew(nblock,ndir+nshr),
     8  defgradNew(nblock,ndir+nshr+nshr),
     9  fieldNew(nblock,nfieldv),
     1  stressNew(nblock,ndir+nshr), stateNew(nblock,nstatev),
     2  enerInternNew(nblock), enerInelasNew(nblock)
C
      character*80 cmname
C
      if (cmname(1:6) .eq. 'VUMAT0') then
          call VUMAT0(nblock, ndir, nshr, nstatev, nfieldv, nprops, lanneal,
     2  stepTime, totalTime, dt, cmname, coordMp, charLength,
     3  props, density, strainInc, relSpinInc,
     4  tempOld, stretchOld, defgradOld, fieldOld,
     5  stressOld, stateOld, enerInternOld, enerInelasOld,
     6  tempNew, stretchNew, defgradNew, fieldNew,
     7  stressNew, stateNew, enerInternNew, enerInelasNew)
```

```
      else if (cmname(1:6) .eq. 'VUMAT1') then
      call VUMAT1(nblock, ndir, nshr, nstatev, nfieldv, nprops, lanneal,
     2  stepTime, totalTime, dt, cmname, coordMp, charLength,
     3  props, density, strainInc, relSpinInc,
     4  tempOld, stretchOld, defgradOld, fieldOld,
     5  stressOld, stateOld, enerInternOld, enerInelasOld,
     6  tempNew, stretchNew, defgradNew, fieldNew,
     7  stressNew, stateNew, enerInternNew, enerInelasNew)
      end if
      end
C
      subroutine vumat0 (
C Read only -
     *     nblock, ndir, nshr, nstatev, nfieldv, nprops, lanneal,
     *     stepTime, totalTime, dt, cmname, coordMp, charLength,
     *     props, density, strainInc, relSpinInc,
     *     tempOld, stretchOld, defgradOld, fieldOld,
     *     stressOld, stateOld, enerInternOld, enerInelasOld,
     *     tempNew, stretchNew, defgradNew, fieldNew,
C Write only -
     *     stressNew, stateNew, enerInternNew, enerInelasNew )
C
      include 'vaba_param.inc'
C
      dimension coordMp(nblock,*), charLength(nblock), props(nprops),
     1     density(nblock), strainInc(nblock,ndir+nshr),
     2     relSpinInc(nblock,nshr), tempOld(nblock),
     3     stretchOld(nblock,ndir+nshr),
     4     defgradOld(nblock,ndir+nshr+nshr),
     5     fieldOld(nblock,nfieldv), stressOld(nblock,ndir+nshr),
     6     stateOld(nblock,nstatev), enerInternOld(nblock),
     7     enerInelasOld(nblock), tempNew(nblock),
     8     stretchNew(nblock,ndir+nshr),
     9     defgradNew(nblock,ndir+nshr+nshr),
     1     fieldNew(nblock,nfieldv),
     2     stressNew(nblock,ndir+nshr), stateNew(nblock,nstatev),
     3     enerInternNew(nblock), enerInelasNew(nblock)
C
      dimension devia(nblock,ndir+nshr),
     1      BBar(nblock,4), stretchNewBar(nblock,4), intv(2)
C
      character*80 cmname
      parameter (zero = 0.D00, one = 1.D00, two = 2.D00, three = 3.D00,
     *                 four = 4.D00, half = 0.5D0)
      real C10,D1,ak,twomu,amu,alamda,hydro,vonMises, maxShear,
     1     midStrain, maxPrincipalStrain
```

```
C
      intv(1) = ndir
     intv(2) = nshr
C
     if (ndir .ne. 3 .or. nshr .ne. 1) then
       call xplb_abqerr(1,'Subroutine VUMAT is implemented '//
     *      'only for plane strain and axisymmetric cases '//
     *      '(ndir=3 and nshr=1)',0,zero,' ')
       call xplb_abqerr(-2,'Subroutine VUMAT has been called '//
     *      'with ndir=%I and nshr=%I',intv,zero,' ')
       call xplb_exit
     end if
C
     C10   = props(1)
     D1    = props(2)
C       C10=1.11619E6  D1=4.48E-8
C
      ak=two/D1
     amu=two*C10
      twomu=four*C10
      alamda=(three*ak-twomu)/three
C
C     if stepTime equals zero, assume pure elastic material and use initial elastic
modulus
C
      if(stepTime .EQ. zero) then
            do k=1,nblock
                  trace1 = strainInc(k,1) + strainInc(k,2) + strainInc(k,3)
                  stressNew(k,1) = stressOld(k,1)
     *                  + twomu * strainInc(k,1) + alamda * trace1
                  stressNew(k,2) = stressOld(k,2)
     *                  + twomu * strainInc(k,2) + alamda * trace1
                  stressNew(k,3) = stressOld(k,3)
     *                  + twomu * strainInc(k,3) + alamda * trace1
                  stressNew(k,4) = stressOld(k,4)
     *                  + twomu * strainInc(k,4)
C           write(6,*) totalTime,k,defgradNew(k, 1),stretchNew(k,1),
C     1                  stressNew(k,2),stressNew(k,3),stressNew(k,4)
            end do
      else
            do k=1,nblock
C
C                  JACOBIAN OF STRETCH TENSOR (U is symmetric and in local
axis)
C
                  det=stretchNew(k, 3)*
```

```
     1          (stretchNew(k, 1)*stretchNew(k, 2)-stretchNew(k, 4)**two)
                scale=det**(-ONE/THREE)
                stretchNewBar(k, 1)=stretchNew(k, 1)*scale
                stretchNewBar(k, 2)=stretchNew(k, 2)*scale
                stretchNewBar(k, 3)=stretchNew(k, 3)*scale
                stretchNewBar(k, 4)=stretchNew(k, 4)*scale
C
C               CALCULATE LEFT CAUCHY-GREEN TENSOR (B is
symmetric)
C
                BBar(k,1)=stretchNewBar(k, 1)**two+stretchNewBar(k, 4)**two
                BBar(k,2)=stretchNewBar(k, 2)**two+stretchNewBar(k, 4)**two
                BBar(k,3)=stretchNewBar(k, 3)**two
                BBar(k,4)=stretchNewBar(k, 1)*stretchNewBar(k, 4) +
     1                stretchNewBar(k, 2)*stretchNewBar(k, 4)
C
C               CALCULATE STRESS tensor
C
                TRBBar=BBar(k,1)+BBar(k,2)+BBar(k,3)
                EG=two*C10/det
                PR=two/D1*(det-one)
                stressNew(k,1)=EG*(BBar(k,1)-TRBBar/Three) + PR
                stressNew(k,2)=EG*(BBar(k,2)-TRBBar/Three) + PR
                stressNew(k,3)=EG*(BBar(k,3)-TRBBar/Three) + PR
                stressNew(k,4)=EG* BBar(k,4)
C
C          Update the specific internal energy
C
          stressPower = half * (
     1      ( stressOld(k,1)+stressNew(k,1) ) * strainInc(k,1) +
     2      ( stressOld(k,2)+stressNew(k,2) ) * strainInc(k,2) +
     3      ( stressOld(k,3)+stressNew(k,3) ) * strainInc(k,3) ) +
     4      ( stressOld(k,4)+stressNew(k,4) ) * strainInc(k,4)
          enerInternNew(k) = enerInternOld(k)
     1       + stressPower / density(k)
C
C               Strains under corotational coordinates
C
                stateNew(k,1) = stateOld(k,1) + strainInc(k,1)
                stateNew(k,2) = stateOld(k,2) + strainInc(k,2)
                stateNew(k,3) = stateOld(k,3) + strainInc(k,3)
                stateNew(k,4) = stateOld(k,4) + strainInc(k,4)
C
C          Calculate vonMises
C
                hydro = (stressNew(k,1)+stressNew(k,2)+
```

```
     1                                    stressNew(k,3))/3.
                        do k1=1,ndir
                        devia(k,k1) = stressNew(k,k1) - hydro
                        end do
                        do k1=ndir+1,ndir+nshr
                        devia(k,k1) = stressNew(k,k1)
                        end do
                        vonMises = 0.
                        do k1=1,ndir
                        vonMises = vonMises + devia(k,k1)**2
                        end do
                        do k1=ndir+1,ndir+nshr
                        vonMises = vonMises + 2*devia(k,k1)**2
                        end do
                        vonMises = sqrt(3./2*vonMises)
C               use 3/2 will get 2 (int) !
C
C                       write(6,*) totalTime,defgradNew(k, 4),stretchNew(k,4)
C     1                 ,defgradNew(k,3),defgradNew(k,4),defgradNew(k,5)
C                       ,det,TRBBar
C     1           ,stressNew(k,1),stressNew(k,2),stressNew(k,3),stressNew(k,4)
C
C                       Failure Criteria
C
                        midStrain = stateNew(k,1) + stateNew(k,2)
                        maxShear = sqrt((stateNew(k,1) - midStrain)**2. +
     1                  stateNew(k,4)**2.)
                        if (midStrain .GE. 0.) then
                                maxPrincipalStrain = midStrain + maxShear
                        else
                                maxPrincipalStrain = maxShear - midStrain
                        end if
                        if (vonMises .GE. 10.8565e6) then
                                stateNew(k,5) = 0
                        end if
                end do
        end if
      return
      end
C
      subroutine vumat1 (
C Read only -
     *     nblock, ndir, nshr, nstatev, nfieldv, nprops, lanneal,
     *     stepTime, totalTime, dt, cmname, coordMp, charLength,
     *     props, density, strainInc, relSpinInc,
     *     tempOld, stretchOld, defgradOld, fieldOld,
```

```
     *     stressOld, stateOld, enerInternOld, enerInelasOld,
     *     tempNew, stretchNew, defgradNew, fieldNew,
C Write only -
     *     stressNew, stateNew, enerInternNew, enerInelasNew )
C
      include 'vaba_param.inc'
     dimension coordMp(nblock,*), charLength(nblock), props(nprops),
     1     density(nblock), strainInc(nblock,ndir+nshr),
     2     relSpinInc(nblock,nshr), tempOld(nblock),
     3     stretchOld(nblock,ndir+nshr),
     4     defgradOld(nblock,ndir+nshr+nshr),
     5     fieldOld(nblock,nfieldv), stressOld(nblock,ndir+nshr),
     6     stateOld(nblock,nstatev), enerInternOld(nblock),
     7     enerInelasOld(nblock), tempNew(nblock),
     8     stretchNew(nblock,ndir+nshr),
     9     defgradNew(nblock,ndir+nshr+nshr),
     1     fieldNew(nblock,nfieldv),
     2     stressNew(nblock,ndir+nshr), stateNew(nblock,nstatev),
     3     enerInternNew(nblock), enerInelasNew(nblock)
C
      dimension devia(nblock,ndir+nshr),
     1      BBar(nblock,4), stretchNewBar(nblock,4), intv(2)
C
           character*80 cmname
      parameter (zero = 0.D00, one = 1.D00, two = 2.D00, three = 3.D00,
     *                 four = 4.D00, half = 0.5D0)
           real C10,D1,ak,twomu,amu,alamda,hydro,vonMises
C
           intv(1) = ndir
      intv(2) = nshr
C
      if (ndir .ne. 3 .or. nshr .ne. 1) then
        call xplb_abqerr(1,'Subroutine VUMAT is implemented '//
     *       'only for plane strain and axisymmetric cases '//
     *       '(ndir=3 and nshr=1)',0,zero,' ')
        call xplb_abqerr(-2,'Subroutine VUMAT has been called '//
     *       'with ndir=%I and nshr=%I',intv,zero,' ')
        call xplb_exit
      end if
C
      C10   = props(1)
      D1    = props(2)
C        C10=1.11619E6  D1=4.48E-8
C
           ak=two/D1
      amu=two*C10
```

```
      twomu=four*C10
      alamda=(three*ak-twomu)/three
C
C     if stepTime equals zero, assume pure elastic material and use initial elastic
modulus
C
      if(stepTime .EQ. zero) then
            do k=1,nblock
                  trace1 = strainInc(k,1) + strainInc(k,2) + strainInc(k,3)
                  stressNew(k,1) = stressOld(k,1)
     *                  + twomu * strainInc(k,1) + alamda * trace1
                  stressNew(k,2) = stressOld(k,2)
     *                  + twomu * strainInc(k,2) + alamda * trace1
                  stressNew(k,3) = stressOld(k,3)
     *                  + twomu * strainInc(k,3) + alamda * trace1
                  stressNew(k,4) = stressOld(k,4)
     *                  + twomu * strainInc(k,4)
C           write(6,*) totalTime,k,defgradNew(k, 1),stretchNew(k,1),
C     1                  stressNew(k,2),stressNew(k,3),stressNew(k,4)
            end do
      else
            do k=1,nblock
C
C                  JACOBIAN OF STRETCH TENSOR (U is symmetric and in local
axis)
C
                  det=stretchNew(k, 3)*
     1           (stretchNew(k, 1)*stretchNew(k, 2)-stretchNew(k, 4)**two)
                  scale=det**(-ONE/THREE)
                  stretchNewBar(k, 1)=stretchNew(k, 1)*scale
                  stretchNewBar(k, 2)=stretchNew(k, 2)*scale
                  stretchNewBar(k, 3)=stretchNew(k, 3)*scale
                  stretchNewBar(k, 4)=stretchNew(k, 4)*scale
C
C                  CALCULATE LEFT CAUCHY-GREEN TENSOR (B is
symmetric)
C
                  BBar(k,1)=stretchNewBar(k, 1)**two+stretchNewBar(k, 4)**two
                  BBar(k,2)=stretchNewBar(k, 2)**two+stretchNewBar(k, 4)**two
                  BBar(k,3)=stretchNewBar(k, 3)**two
                  BBar(k,4)=stretchNewBar(k, 1)*stretchNewBar(k, 4) +
     1                  stretchNewBar(k, 2)*stretchNewBar(k, 4)
C
C                  CALCULATE STRESS tensor
C
                  TRBBar=BBar(k,1)+BBar(k,2)+BBar(k,3)
```

```
                    EG=two*C10/det
                    PR=two/D1*(det-one)
                    stressNew(k,1)=EG*(BBar(k,1)-TRBBar/Three) + PR
                    stressNew(k,2)=EG*(BBar(k,2)-TRBBar/Three) + PR
                    stressNew(k,3)=EG*(BBar(k,3)-TRBBar/Three) + PR
                    stressNew(k,4)=EG* BBar(k,4)
C
C       Update the specific internal energy
C
      stressPower = half * (
     1   ( stressOld(k,1)+stressNew(k,1) ) * strainInc(k,1) +
     2   ( stressOld(k,2)+stressNew(k,2) ) * strainInc(k,2) +
     3   ( stressOld(k,3)+stressNew(k,3) ) * strainInc(k,3) ) +
     4   ( stressOld(k,4)+stressNew(k,4) ) * strainInc(k,4)
      enerInternNew(k) = enerInternOld(k)
     1    + stressPower / density(k)
C
C                   Strains under corotational coordinates
C
                    stateNew(k,1) = stateOld(k,1) + strainInc(k,1)
                    stateNew(k,2) = stateOld(k,2) + strainInc(k,2)
                    stateNew(k,3) = stateOld(k,3) + strainInc(k,3)
                    stateNew(k,4) = stateOld(k,4) + strainInc(k,4)
C
C       Calculate vonMises
C
                    hydro = (stressNew(k,1)+stressNew(k,2)+
     1                          stressNew(k,3))/3.
                    do k1=1,ndir
                    devia(k,k1) = stressNew(k,k1) - hydro
                    end do
                    do k1=ndir+1,ndir+nshr
                    devia(k,k1) = stressNew(k,k1)
                    end do
                    vonMises = 0.
                    do k1=1,ndir
                    vonMises = vonMises + devia(k,k1)**2
                    end do
                    do k1=ndir+1,ndir+nshr
                    vonMises = vonMises + 2*devia(k,k1)**2
                    end do
                    vonMises = sqrt(3./2*vonMises)
C                   write(6,*) totalTime,defgradNew(k, 4),stretchNew(k,4)
C    1              ,defgradNew(k,3),defgradNew(k,4),defgradNew(k,5)
C                   ,det,TRBBar
C    1          ,stressNew(k,1),stressNew(k,2),stressNew(k,3),stressNew(k,4)
```

```
            end do
        end if
    return
    end
```